Effect of non-equilibrium fluctuations in transport and escape problems

By

Vishwajeet Kumar

Enrolment No. : PHYS10202104005

The Institute of Mathematical Sciences, Chennai

Supervisor: Dr. Arnab Pal

The Institute of Mathematical Sciences, Chennai

A thesis submitted to the

Board of Studies in Physical Sciences

In partial fulfillment of requirements

for the Degree of

DOCTOR OF PHILOSOPHY

of

HOMI BHABHA NATIONAL INSTITUTE

Homi Bhabha National Institute

Recommendations of the Viva Voce Committee

As members of the Viva Voce Committee, we certify that we have read the dissertation prepared by Vishwajeet Kumar entitled "Effect of non-equilibrium fluctuations in transport and escape problems" and recommend that it may be accepted as fulfilling the thesis requirement for the award of Degree of Doctor of Philosophy.

Sibasish Ghosh

Date: 27 July, 2026

Chairman - Prof. Sibasish Ghosh

Arnab Pal

Date: 27 July, 2026

Guide/Convenor - Dr. Arnab Pal

Date: 27 July, 2026

Examiner - Prof. Rajarshi Chakrabarti

Date: 27 July, 2026

Member 1 - Prof. Satyavani Vemparala

Date: 27 July, 2026

Member 2 - Prof. Pinaki Chaudhuri

Date: 27 July, 2026

Member 3 - Prof. Bijay Kumar Agarwalla

Final approval and acceptance of this thesis is contingent upon the candidate's submission of the final copies of the thesis to HBNI.

I hereby certify that I have read this thesis prepared under my direction and recommend that it may be accepted as fulfilling the thesis requirement.

Date: 27/07/2026

Arnab Pal

Place: Chennai

Guide

STATEMENT BY AUTHOR

This dissertation has been submitted in partial fulfillment of requirements for an advanced degree at Homi Bhabha National Institute (HBNI) and is deposited in the Library to be made available to borrowers under rules of the HBNI.

Brief quotations from this dissertation are allowable without special permission, provided that accurate acknowledgement of source is made. Requests for permission for extended quotation from or reproduction of this manuscript in whole or in part may be granted by the Competent Authority of HBNI when in his or her judgement the proposed use of the material is in the interests of scholarship. In all other instances, however, permission must be obtained from the author.

Vishwajeet Kumar

DECLARATION

I hereby declare that the investigation presented in the thesis has been carried out by me. The work is original and has not been submitted earlier as a whole or in part for a degree / diploma at this or any other Institution / University.

Vishwajeet Kumar

LIST OF PUBLICATIONS ARISING FROM THE THESIS

Publications:

- **Published**

1. **Inferring intermediate states by leveraging the many-body Arrhenius law**

   — V. Kumar, A. Pal, O. Shpielberg; The Journal of Chemical Physics 163 (22) (2025)

2. **Speeding up Brownian escape via intermediate finite potential barriers**

   — V. Kumar, O. Shpielberg, A. Pal; Chaos: An Interdisciplinary Journal of Nonlinear Science 35 (11) (2025)

3. **Emerging universality classes in thermally assisted activation of interacting diffusive systems: A perturbative hydrodynamic approach**

   —V. Kumar, A. Pal, O. Shpielberg; The Journal of Chemical Physics 160 (13) (2024)

4. **Arrhenius law for interacting diffusive systems**

   —V. Kumar, A. Pal, O. Shpielberg; Physical Review E 109 (3), L032101(2024)

Vishwajeet Kumar

Vishwajeet Kumar

List of presentations and participation at conferences

Talks:

1. At the S. N. Bose National Centre for Basic Sciences, Kolkata on May 5, 2025.
   Title : Exploring Metastabilities : Decoding unknown energy landscapes by leveraging Generalized Arrhenius Law.

2. At the Workshop on Stochastic Thermodynamics (WOST) V on 15th May, 2024. Title : Arrhenius law for Interacting Diffusive Systems.

Posters

1. At the 10th Indian Statistical Physics Community Meeting at ICTS, Bangalore : April 23 - April 25, 2025.
   Topic : Exploring Metastability: Decoding an unknown energy landscape by leveraging Arrhenius Law for interacting diffusive systems.

2. At the Frontiers in Non-equilibrium Physics (FNEP), The Institute of Mathematical Sciences, Chennai from Jan 7-10, 2025.
   Topic : Exploring Metastability: Decoding an unknown energy landscape.

3. At the Summer school in Les Houches on Large deviations and applications, France from 1-26 July, 2024.
   Topic: Arrhenius law for interacting diffusive systems and Emerging Universality.

4. At the Frontiers in Statistical Physics, Raman Research Institute, Bangalore from 04-08 December 2023.

Topic: Arrhenius law for interacting diffusive systems and Emerging Universality.

5. At the Frontiers in Non-equilibrium Physics (FNEP), The Institute of Mathematical Sciences, Chennai from 17-20 January, 2023.
   Topic : Arrhenius law for interacting diffusive systems.

6. At the event IMSc 60, Institute of Mathematical Sciences, Chennai, from 02-05 January, 2023.
   Topic : Arrhenius law for interacting diffusive systems.

7. Meeting On Statistical Physics and Complex Systems, IIT Kharagpur, 2023.
   Topic : Arrhenius law for interacting diffusive systems.

Dedicated to my Mom, Dad, Brother and Sister

ACKNOWLEDGEMENTS

The completion of this thesis would not have been possible without the support, guidance, and encouragement of many individuals and institutions. I would like to take this opportunity to express my sincere gratitude to all those who have assisted me throughout this journey.

First and foremost, I express my deepest gratitude to my mother; words are simply not enough to convey the extent of her unwavering support, sacrifices, and boundless love that have shaped every step of my life. I am deeply grateful to my brother, whose constant support, understanding, and companionship have always been a source of strength, and to my sister for her support and care. Words are insufficient to express the depth of their love and the significance they hold in my life, which has sustained me through every challenge along this journey. The moments I have spent with them are truly the most beautiful and meaningful parts of my life, and I cherish them more than anything.

I am deeply grateful to my supervisor, Dr. Arnab Pal, for his constant guidance, invaluable insights, and unwavering support throughout the course of my doctoral studies. He has always been available to guide and support his students. I have greatly benefited from the countless in-depth scientific discussions with him, which have significantly shaped my understanding and approach to research. His encouragement to think beyond conventional boundaries and his openness to new ideas have been particularly inspiring. His clarity of thoughts and deep understanding of the subjects have been a constant source of inspiration for me.

I am also very grateful to my collaborator, Dr. Ohad Shpielberg, with whom I had the privilege of working. I have always admired his exceptional mathematical

insights and profound critical thinking. I am sincerely thankful to him for helping me navigate and understand several technical aspects of this work. I greatly valued our discussions, which have significantly deepened my understanding of macroscopic fluctuation theory and related topics.

I am also grateful to my doctoral committee members: Prof. Sibasish Ghosh, Prof. Satyavani Vemparala, Prof. Pinaki Chaudhuri and Prof. Bijay Kumar Agarwalla for their time in reviewing my works, motivating me and providing critical constructive suggestions. I am also very thankful to Dr. Sayantan Sharma for his help and support.

I would like to express my sincere gratitude to Ghulam Sarwar Sir, who has been a constant source of support and encouragement. I am also thankful to Ghorai Sir for his timely help on several occasions and for his continued encouragement. I am very grateful to Prof. M. M. R. Akhtar, who taught me Physics during my higher secondary education; his exceptional teaching ability and clarity of explanation have left a lasting impression on me.

I am deeply grateful to my friends Abul, Vishal, Panchanan, and Krishanu for their support and time. I also owe a special thanks to my batchmates and first friends at IMSc—Arup, Harshit, Sashikanta, and Saurav—for making my start here so memorable. My thanks go to Arup and Ashutosh for the several discussions and the fun we shared along the way. I would also like to thank Amit and Dhananjay for their kind companionship, whether over a meal or a quick visit to the juice shop. To my group members—Ashutosh, Reshmi, Arup, Rahul, and Jitin—thank you for the scientific debates and the equally important non-scientific ones. Thank you for all the funs we had. I am also grateful to Sushant, Rohit, Suraj, Sarbartha, Pritesh, Prem, Ravi and Goutham for their friendship, as well as my seniors Apurba, Manav, Bishwajit, Arghya, Sitendar, Sahil, Tanmoy, Arabinda, and Shivesh for their support and guidance. To anyone I may have missed, please accept my apologies; I am truly

grateful to all of you for being part of this journey. You people have made this journey interesting and enjoying.

I am also thankful to my friends and seniors on the Cricket Ground: Rakesh, Pritesh, Umang, Hitesh, Sathish, Manikandan, Arun, Anuj, Partha, Ratan, Purushottam, Faizan, Rahul, Gopal, Vijay, Vasan, Moovendan, Nikhil and many more. Cricket as a sport has been there with me since childhood and I enjoyed a lot playing with you people.

I would like to express my sincere gratitude to the Director of IMSc for their continued support during my tenure. I am also thankful to the institute for providing the excellent facilities that made this work possible.

My thanks go to the entire administrative team, the Registrar, Indra, Sadhana, and everyone for their coordination. I am also thankful to the people at the Library and the Computer Facilities team—particularly Vasan and colleagues—for their technical assistance throughout my tenure.

Needless to say, this list is far from complete. It is often said that every person who crosses our path teaches us something valuable. I am deeply thankful to everyone who has touched my life during this journey.

Contents

List of Figures

Chapter 1

Introduction

Many physical phenomena become significant when systems are considered at microscopic scales, where fluctuations play an important role in determining their properties. At macroscopic scales, fluctuations are typically negligible because they are strongly suppressed by the presence of an enormous number of constituent particles, leading to well-defined average behavior. In contrast, at microscopic scales the fluctuations in quantities such as energy, particle number, or position can become comparable to their mean values. A classical example is Brownian motion, where a suspended particle undergoes irregular motion as a result of continuous thermal collisions with surrounding fluid molecules [2]. Consequently, a deterministic description is often insufficient at this scale, and a proper theoretical framework requires probabilistic approaches, which allow one to quantify the statistics of fluctuations and understand their impact on macroscopic observables.

One of the earlier microscopic description of such non-deterministic motion was proposed by Paul Langevin in year 1908, which is now known as the Langevin equation. Langevin postulated that the dynamics of a Brownian particle are governed by Newton's equation of motion, supplemented by two additional forces arising from its interaction with the surrounding fluid [3]. The first is a viscous drag force, which accounts for the friction experienced by the particle as it moves through the fluid. The

second is a random fluctuating force that rapidly varies in time and represents the effect of collisions with the surrounding fluid molecules. Together, these two forces capture the stochastic influence of the environment on the motion of the Brownian particle. The resulting Langevin equation is given by [3, 4]

$$m\ddot{x} = -\mu\dot{x} + \sqrt{2D}\,\xi(t) \tag{1.1}$$

where m denotes the mass of the particle, μ is the friction coefficient associated with viscous drag, and $\xi(t)$ is a stochastic force/noise with zero mean, $\langle \xi(t) \rangle = 0$, and delta correlation, $\langle \xi(t)\xi(t') \rangle = \delta(t - t')$. The parameter D represents the strength of the noise.

A fundamental requirement is that, at long times, the particle must relax to thermal equilibrium with the surrounding medium. This requirement imposes a constraint on the relative strengths of dissipation and fluctuations. In particular, the dissipative drag term $-\mu\dot{x}$ continuously removes energy from the system, while the noise injects energy through random kicks. Thermal equilibrium is achieved only when these two effects balance in a precise manner, leading to a relation between the noise strength D and the friction coefficient μ. This relation, known as Einstein's relation or the fluctuation–dissipation theorem, is given by $D = \mu k_B T$, where k_B is the Boltzmann constant and T denotes the temperature of the surrounding medium [4].

Since the microscopic dynamics are governed by stochastic equations [Eq. (1.1)], the observables associated with such dynamics are themselves stochastic, and exhibit statistical variation around their mean values. As a result, observables of interest must be characterized through their statistical properties, such as probability distributions, mean values, and higher moments.

Although fluctuations are especially pronounced at microscopic scales, they are not entirely absent at macroscopic scales. Macroscopic fluctuations arise as a direct

consequence of the stochastic nature of the microscopic degrees of freedom that collectively determine the behavior of physical macroscopic systems. Even though macroscopic observables typically attain the corresponding average values, small deviations from these typical values inevitably occur due to the underlying microscopic randomness. In thermodynamic equilibrium, the probability of such fluctuations from mean can be determined in a systematic manner, and equilibrium statistical mechanics provides an explicit relation between fluctuation probabilities and thermodynamic variables describing the system. Consequently, equilibrium fluctuations are quantitatively governed by variations of these macroscopic state functions. As an illustrative example, let us consider an equilibrium system in the canonical ensemble. According to statistical mechanics, the probability of the system having an energy E is given by

$$P(E) = \frac{1}{Z} f(E) e^{-E/k_B T} \tag{1.2}$$

where, Z denotes the canonical partition function, $f(E)$ represents the density of states of the system at energy E and T is the temperature of the heat bath. This expression determines the equilibrium energy distribution and encapsulates complete information about the statistics of energy fluctuations around the mean value $\langle E \rangle$. In particular, the energy fluctuations σ_E^2 about the mean $\langle E \rangle$ is given by [5]

$$\sigma_E^2 = \langle E^2 \rangle - \langle E \rangle^2 = k_B T^2 C_v, \tag{1.3}$$

where C_v denotes the heat capacity of the system at constant volume.

Although a well established theoretical framework exists for characterizing fluctuations in systems at thermodynamic equilibrium, as discussed above, the situation is considerably more challenging for systems out of equilibrium. In contrast to the equilibrium case, there is no general and universal theory that fully characterizes

the statistics of fluctuations in systems driven out of equilibrium. Nevertheless, significant progress has been made toward understanding fluctuations in such systems. One of the notable developments at the microscopic level is the framework of *Stochastic Thermodynamics*, which provides a systematic approach to describe non-equilibrium processes by extending classical thermodynamic quantities, such as work, heat, and entropy, to individual stochastic trajectories [6, 7]. This formulation enables a detailed characterization of fluctuations at the microscopic scale. Another significant achievement, at the coarse grained level, is the development of the *Macroscopic Fluctuation Theory* (MFT) which provides a systematic framework to describe fluctuations in a broad class of non-equilibrium systems, namely the driven diffusive systems. Within this framework, the system is described in terms of particle density and current fields, which together determine the probability of a trajectory followed by the system. This formulation enables the computation of various observables of interest in non-equilibrium settings [8–11]. An overview of MFT is presented in Appendix A.

A particularly important consequence of such fluctuations in non-equilibrium systems is the emergence of rare events, which can drive the system far from its typical behavior and induce transitions between distinct configurations or phases. These transitions are particularly significant when the system is confined to a metastable state, where it can remain trapped for long durations until a rare fluctuation induces a transition to another state [12]. Such escape constitutes a fundamental class of fluctuation-induced phenomena and arises in a wide range of physical, chemical, and biological systems. For example, in chemical reactions, reactant molecules must overcome an activation barrier to break existing bonds and form new ones, thereby enabling the transformation of reactants into more stable products. In another instance, during protein folding, a polypeptide chain can undergo a series of conformational transitions across multiple intermediate states by overcoming energy barriers before ultimately attaining its native, stable structure.

A quantitative understanding of such transitions or escape processes is credited to Van't Hoff and Arrhenius, who empirically established the dependence of chemical reaction rates on activation barriers and temperature, a relation now known as the Arrhenius law. In particular, they demonstrated that reaction rates exhibit an exponential dependence on the activation barrier and the inverse temperature. Many years later of this formulation, Kramers gave diffusion model of chemical reactions and he showed that the rate of escape of a Brownian particle from a potential barrier exhibits the same exponential dependence on the height of the barrier and inverse temperature; see Eq. (1.5) and Fig. 1.1(a).

The universality of the escape rate, namely its exponential dependence solely on the barrier height rather than on the detailed structure of the underlying potential landscape, has motivated extensive investigations of the validity of Arrhenius law across a broad class of systems. While the Arrhenius form remains valid in many cases, notable deviations have been reported in certain cases, such as an active particle system [13]. This naturally leads to the question of whether such universality persists in interacting systems, which forms the basis of the first part of this thesis. In this context, we analyze the escape rate for interacting diffusive systems by employing the MFT and demonstrate that this universality can break down in the presence of interactions, leading to a generalized formulation that we refer to as the generalized Arrhenius law. See Fig. 1.1(b). Furthermore, we show that this framework can be systematically exploited to infer the number of metastable states in an unknown energy landscape; see Sections 1.1, 1.2, and 1.3.

In the last part of the thesis, we employ the first-passage formalism to investigate a strategy for accelerating the escape of a single Brownian particle over a potential barrier. This study is motivated by the observation that, while the exponential factor in the Arrhenius law exhibits universality, the pre-exponential factor depends sensitively on the form of the potential landscape. Consequently, by appropriately

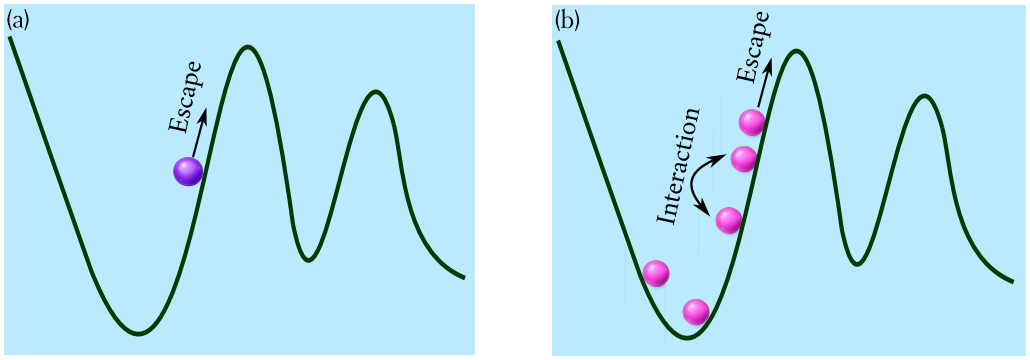

Figure 1.1: Panel (a): Escape of a single particle from a potential trap. In this case, the escape rate is governed by the conventional Arrhenius law, as given in Eq. (1.5). Panel (b): Escape of a particle in an interacting diffusive system from a potential trap. In this case, the escape rate deviates from the conventional Arrhenius form and is instead described by the generalized Arrhenius law, as given in Eq. (1.6).

reshaping the potential landscape while keeping the overall barrier height fixed, one can significantly reduce the mean barrier-crossing time; see Sec. 1.4.

1.1 The conventional Arrhenius law

The Arrhenius law (AL), which provides one of the earliest quantitative descriptions of escape and activation processes, states that the escape rate r of a chemical reaction is given by

$$r = \alpha e^{-E_A/k_B T}, \tag{1.4}$$

where, α is a pre-factor and E_A denotes the activation energy required to initiate the reaction.

Subsequent developments in the understanding of escape processes clarified that such activation events are rare and arise from stochastic fluctuations. In 1935, Eyring [14] and Evans and Polanyi [15] gave the theory to describe rates of reactions, what later became known as conventional Transition State Theory (CTST). To briefly explain the idea of CTST, consider a reaction between two atoms P and Q eventually forming a product R, $P + Q \rightleftharpoons R$. For such a system, the potential energy surface

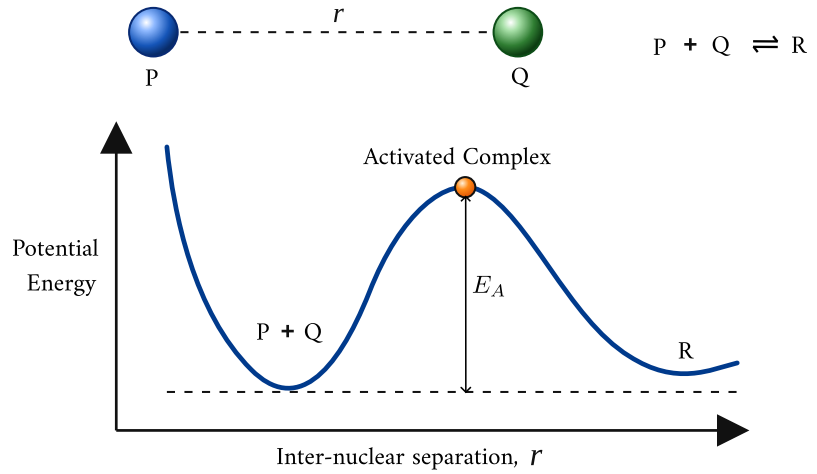

Figure 1.2: Schematic illustration of a reaction between two atoms P and Q forming a product R. To form the product, the reactants must overcome the potential energy barrier E_A. The top of this barrier corresponds to the activated complex. The reaction rate is given by Eq. (1.4).

reduces to a one-dimensional curve describing the potential energy as a function of the inter-nuclear separation between P and Q. See Fig. 1.2. In reactions involving more than two atoms, the potential energy surface becomes multidimensional [16]. A reaction may then be visualized as the motion of the system on this potential energy surface from the reactant configuration to the product configuration. The reactant and product states correspond to valleys on the surface. These valleys meet at a stationary point known as a col or saddle point, which corresponds to an activated complex. Within this framework, CTST assumes quasi-equilibrium between reactants and the activated complex, allowing its concentration to be determined using equilibrium statistical mechanics, and further assumes that trajectories crossing the saddle in the forward direction proceed to products without recrossing. Under these assumptions, the CTST derives an explicit expression for the reaction rate, thereby yielding a microscopic statistical derivation of the Arrhenius form [14–16].

In 1940, Kramers presented his seminal work [17], in which he established his diffusion model of chemical reaction. In contrast to the CTST picture, the reacting system is coupled to a thermal medium maintained at some fixed temperature T and characterized by a viscosity or friction coefficient, so that the motion is influenced

both by systematic damping and by random thermal noise. The activation process is modeled as the motion of a one-dimensional Brownian particle in a potential well $U(x)$, coupled to a heat bath at temperature T, with its dynamics described by the Langevin equation with an external force term, $m\ddot{x} = -U'(x) - \mu\dot{x} + \sqrt{2D}\,\xi(t)$. Escape from the metastable well requires surmounting a barrier of height ΔU. Within this framework, Kramers computed the escape rate in distinct damping regimes by analyzing the corresponding Fokker–Planck equation. In the high-barrier limit, $\Delta U \gg k_B T$, he demonstrated that the escape rate is exponentially suppressed and given by the Boltzmann factor $\exp(-\Delta U/k_B T)$, reflecting the rarity of escape. Additionally, through a careful evaluation of the probability flux across the barrier, he obtained the viscosity-dependent pre-exponential factor in the intermediate to strong damping regimes.

In the high damping regime, where the friction is sufficiently large such that the inertial term in the Langevin equation can be neglected, the escape rate is given by [17–20]

$$\Phi_{\rm SP} = \mathcal{T}_0^{-1} \exp\left(-\frac{\Delta U}{k_B T}\right). \tag{1.5}$$

Here, without loss of generality, we set the friction coefficient to unity. Eq. (1.5) applies when the barrier height is much greater than the average thermal energy of the particle, i.e., $\Delta U \gg k_B T$, where ΔU is the height of the potential barrier and T is the temperature of the surrounding environment. The subscript SP denotes that the system is of single Brownian particle. $\mathcal{T}_0$ is microscopic non-universal time scale of the system that depends on specific form of the potential trap $U(x)$. By contrast, the exponential factor exhibits a universal character: it depends solely on the barrier height ΔU and on the temperature T, and is independent of any other details of trap. See Fig. 1.3.

To understand Eq. (1.5) better, imagine a diffusive process on a multidimensional, rugged energy landscape. Presence of a variety of local minima surrounded by energy

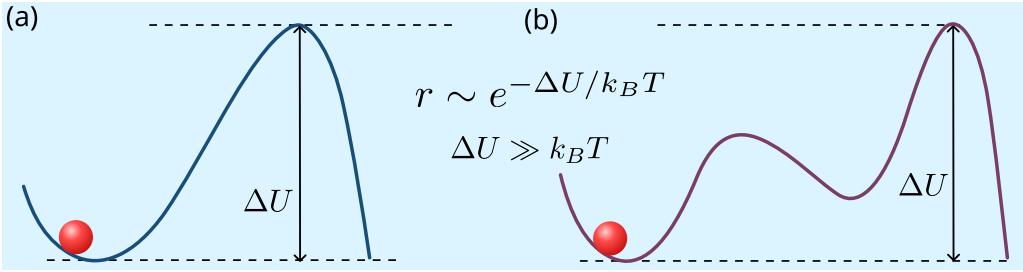

Figure 1.3: Panels (a) and (b) schematically show two different potential landscapes. In both cases, however, the particle must overcome the same barrier height ΔU. When $\Delta U \gg k_B T$, the exponential factor in the escape rate is therefore the same for the two potentials, reflecting the universality of the Kramers escape-rate formula given in Eq. (1.5).

barriers $\Delta U \gg k_B T$ renders a natural separation of timescales in these systems—fast fluctuations in the well followed by slow and rare fluctuations between the wells. In other words, the particle fluctuates many times within a well (typical trajectories) before leaving it (rare trajectories). This is a key assumption behind Eq. (1.5) in generic activation processes [21–24].

The universal exponential dependence $\exp(-\Delta U/k_B T)$ in Eq. (1.5) implies that the activation barrier ΔU can be inferred directly from escape rate data. In particular, taking the logarithm of the escape rate renders it linear in the inverse temperature $\beta = 1/(k_B T)$. Consequently, a plot of $-\log \Phi_{\mathrm{SP}}$ as a function of β yields a straight line, the slope of which is given by ΔU.

It is precisely this universal structure of the Arrhenius law that underlies its broad applicability across a wide range of physical systems and has sustained extensive theoretical and experimental interest over several decades; comprehensive reviews may be found in Refs. [18, 19]. Despite many years of study, discoveries are still being made around the AL and exciting applications continue to be found such as activation in the presence of viscoelastic medium [25, 26], escape dynamics of active particles [13, 27–30], temperature dependent activation energies [31, 32], multiple metastable states [27], experiments with colloids [33, 34], semiclassical transition rate theory [35], and inference methods from barrier crossings [36, 37]. Further

notable studies that have provided deeper insight into activation dynamics include elucidating the influence of long-range temporal correlations or memory effects on the escape time statistics [38, 39], as well as the escape dynamics of composite systems such as dimers [40–42], thereby underscoring the continuing relevance and richness of the Arrhenius paradigm across diverse physical settings.

Despite numerous studies, the validity of the AL remains less explored in interacting systems. The presence of interactions raises fundamental questions regarding the validity and universality of the AL. In addition to the existing slow and fast timescales, the "nature" of interaction also sets another timescale in the problem. Consequently, the universal exponential decay in AL may no longer hold true due to the complex interplay of different agents and their interactions [43–46]. Indeed, explicit breakdowns of Arrhenius behavior have been demonstrated in several contexts. For instance, the rate of escape of an active particle from a potential trap acquires an exponential contribution that depends explicitly on its self-propulsion speed, thereby deviating from the classical Arrhenius form. As shown in Ref. [13], this modification in the exponential term can give rise to the counterintuitive scenario in which, for certain ranges of propulsion speed, a particle may surmount a higher potential barrier more readily than a lower one, reflecting a qualitative departure from the standard activation picture, Eq. (1.5). Similar deviations arise in glassy systems. In particular, for most glass-forming liquids, the viscosity does not exhibit a simple Arrhenius temperature dependence as the system is cooled towards the glass transition [32]. Therefore, it is not a priori clear whether the exponential Arrhenius form remains universal in interacting systems, or whether interactions qualitatively modify the dependence of escape rates on thermal noise. This naturally leads to the question of whether a generalized Arrhenius law can be formulated for interacting systems, and, if so, how the effective activation barrier are shaped by interparticle interactions. The first part of this thesis is devoted to addressing these issues to determine the AL in the context of interacting diffusive systems, as

discussed in the subsequent sections.

1.2 The generalized Arrhenius law for interacting diffusive systems

Building on the framework of Macroscopic Fluctuation Theory (MFT), we derive a generalized Arrhenius law (AL) for interacting diffusive systems and show that it assumes the following simplified form

$$\Phi_{\mathrm{MP}} \asymp e^{-\beta \Delta U g(\overline{\rho}_0)} \tag{1.6}$$

where the subscript MP stands for interacting diffusive many-particles system, $\overline{\rho}_0$ is the average particle density of the system and the function $g(\overline{\rho}_0)$ quantifies the modification induced by interactions in the escape rate relative to the single-particle result given in Eq. (1.5).

To understand Eq. (1.6) better, let us consider two paradigmatic examples of interacting-difusive systems, namely the symmetric simple exclusion process(SSEP) [47] and the zero range process(ZRP) [48]. In SSEP, each lattice site can be occupied by at most one particle, and a particle can hop to a nearest-neighbour site only if the target site is vacant. This constraint gives rise to an excluded-volume interaction, which refers to the geometric restriction that particles cannot occupy the same spatial region simultaneously, so that each particle effectively excludes a finite volume from being accessed by others. As a consequence, the system exhibits an effective repulsive interaction. For such a system having excluded-volume interactions, the function $g(\overline{\rho}_0)$ depends on the average particle density as well as the form of the potential trap $U(x)$. Consequently, the exponential factor in Eq. (1.6) acquires an explicit dependence on the potential landscape, in contrast to the con-

ventional Arrhenius law in Eq. (1.5), which depends solely on the barrier height. This establishes that excluded-volume interactions break the universality of the conventional Arrhenius form. Remarkably, however, all systems characterized by excluded-volume interactions exhibit the same functional form of $g(\overline{\rho}_0)$, irrespective of the details of the underlying microscopic dynamics. We refer to this class of systems as the excluded-volume universality class.

In contrast to the SSEP, the ZRP does not involve excluded-volume constraints, as the occupation number at each lattice site is unbounded. The hopping rate to a neighbouring site depends on the number of particles at the departure site, which may give rise to either effective attractive or repulsive interactions depending on its functional form. For such systems without excluded-volume interactions, the function satisfies $g(\overline{\rho}_0) = 1$, implying that the exponential factor in Eq. (1.6) reduces to that of the conventional Arrhenius form. Consequently, the universality in Eq. (1.5) is preserved, and such systems are therefore classified as belonging to the Arrhenius universality class.

The details and analysis are provided in Chapter 2. Further, in Chapter 3 we present another method called perturbative hydrodynamic approach to analytically validate the existence and range of validity for these two universality classes.

1.3 Inferring the number of metastable states of an unknown landscape using the generalized Arrhenius law.

Going forward, in Chapter 4 we demonstrate that the generalized Arrhenius law for interacting diffusive systems with excluded volume interactions can be systematically exploited to infer the number of metastable states in an unknown potential

landscape, an inference that is not possible within the framework of the traditional Arrhenius law, Eq. (1.5). In particular, for systems with excluded-volume interactions, the function $g(\overline{\rho}_0)$, appearing in the exponential term of the escape rate, develops non analytic points (kinks), the number of which coincides with the number of extremal points in the underlying landscape. Consequently, determining the number of metastable states reduces to identifying the number of kinks in $g(\overline{\rho}_0)$. A practical challenge, however, arises because these non analytic features become apparent only in the asymptotic limit $\beta\Delta U \to \infty$, a regime that is not experimentally accessible. To overcome this limitation, we establish a correspondence between the escape problem under consideration and equilibrium thermodynamic phase transitions, which enables the introduction of an effective free energy and associated response functions. We show that these response functions exhibit pronounced peaks at finite values of $\beta\Delta U$, and that the number of such peaks is in one to one correspondence with the number of kinks in $g(\overline{\rho}_0)$. Thus, although the extrema of the landscape are formally encoded in the asymptotic non analytic structure of $g(\overline{\rho}_0)$, their signatures persist at experimentally relevant barrier heights in the form of pronounced peaks in response functions. This establishes a robust and experimentally accessible protocol for identifying the number of extrema in an unknown energy landscape.

1.4 Speeding-up of the Brownian escape

A prominent theme in recent developments in the understanding of escape dynamics is the search for mechanisms or controls that can *accelerate* the escape process—critical in applications ranging from chemical kinetics to molecular machines. Several innovative strategies have emerged to reduce the mean barrier crossing time. These include: noise engineering – modulating the memory time of colored noise has been shown to significantly influence the crossing dynamics [49]; stochastic resetting – introducing resetting protocols [50–58]—where particles are intermittently

returned to a specific location—can lead to an optimal escape rate under certain conditions [59–64]; time-dependent driving: applying weak, time-periodic forces to the system can enhance the likelihood of barrier crossing via stochastic resonance mechanisms [65]; removal of single maximum trapping time along the path of a tracer in disordered systems [66]. Such mechanisms are of considerable interest both from a fundamental perspective and in applications where rapid barrier crossing is desirable. The last part of the thesis is devoted to investigating one such mechanism, with the aim of identifying conditions under which barrier-crossing events can be systematically accelerated.

Among these approaches, manipulating the underlying potential landscape constitutes one natural way to control barrier-crossing times [34, 67, 68]. Understanding how controlled modifications of the potential profile influence escape dynamics remains an active area of research. This is also important since diffusion of particles, ions, molecules, or even living microorganisms in confined geometries such as tubes and channels plays a key role across various scales in natural and technological processes [69–71]. One promising direction in this context involves reshaping the potential profile, a mechanism that will be explored in Chapter 5 with the aim of facilitating faster escape.

To explore the effect of reshaping the potential profiles on barrier-crossing times, we employ the first-passage formalism, in which barrier-crossing time is the mean first-passage time (MFPT), with the absorbing boundary placed at the top of the potential barrier. Within this framework, we demonstrate that a suitable modification of the potential landscape, while preserving the overall barrier height, can lead to a substantial reduction in the MFPT relative to that of the original unmodified potential. The modification is done via the introduction of finite intermediate barriers. Furthermore, we show that increasing the number of such intermediate barriers yields additional reduction in the MFPT. This effect is not limited to simple linear

potentials; analogous improvements can also be achieved in non-linear landscapes by replacing smooth potentials with suitably constructed piecewise profiles. Detailed results and analysis are presented in Chapter 5.

1.5 Structure of the thesis

For brevity, we now provide an outline of the thesis. In Chapter 2, we derive the generalized AL and establish the emergence of the universality classes. Additional technical details related to this chapter are presented in Appendix C. In Chapter 3, we introduce an alternative derivation based on a perturbative hydrodynamic approach, which further confirms the existence of the universality classes and identifies their range of validity. In Chapter 4, we investigate the inference properties of the generalized AL for interacting diffusive systems with excluded-volume interactions; supplementary material for this chapter is provided in Appendix D. In Chapter 5, we examine a mechanism based on controlled manipulation of the potential landscape to achieve a reduction in barrier-crossing times of a single Brownian particle, with additional details included in Appendix E. In Chapter 6, we conclude with a summary of the main results and a discussion of possible future directions. Appendix A presents an overview of macroscopic fluctuation theory, followed by a discussion of the additivity principle (which is employed in Chapter 2) in Appendix B. Finally, Appendix F contains the derivation of diffusivity and mobility for a few representative models of interacting diffusive systems.

Chapter 2

Arrhenius law for interacting diffusive systems

The content of this chapter has been published in [72]

2.1 Introduction

As discussed in Chapter 1, the conventional Arrhenius law (AL) [Eq. (1.5)] exhibits universality in its exponential term, in the sense that this term depends only on the barrier height and is otherwise independent of the detailed structure of the potential landscape. Surprisingly, this universality has not been systematically examined in the context of interacting systems. The presence of interactions introduces additional correlations and collective effects, thereby rendering the dynamics considerably more complex. Consequently, it is not a priori clear whether the universality exhibited by the conventional Arrhenius law continues to hold in interacting systems.

In what follows, we postulate a setup, where (1.5) cannot hold. Consider a system of finite size colloids, restricted to move in a $1D$ tube, and trapped by an external potential. If the density of colloids in the trap is finite, they cannot all occupy the bottom of the potential as some of the colloids are pushed away from the bottom. Hence, an effective activation energy, smaller than ΔU, may be considered. Naively,

this effective activation energy can depend on the inter-colloid interaction and the interaction of the colloid with the medium. Clearly, it also depends on the density of colloids in the trap, ultimately suggesting a violation of the AL (1.5). This simple setup rightly shows the key role of interactions in the escape problem of AL and why a new formulation is very much needed to generalize the AL for interacting systems.

Our aim in this chapter is therefore to delve deeper into the AL for interacting diffusive systems. However, before doing that, it is insightful to derive the AL for M non-interacting particles. Notably, the AL can be computed from the large time survival probability which can be derived by mapping the problem to an effective Schrödinger equation with absorbing boundaries – see the textbook [20] for this standard procedure. Technically, the survival probability $\mathcal{S}(t) \asymp \exp\left[-t\,\Phi_{\rm NI}\right]$ [1], where the escape rate $\Phi_{\rm NI} = ME_0$ and E_0 is the ground state energy of the Fokker-Planck Hamiltonian $\hat{H}_{FP} = -D_0\partial_{xx} + \frac{D_0}{4}(\partial_x U/D_0)^2 - \frac{1}{2}\partial_{xx}U$, where $D_0 = k_BT$. See Appendix C.1 for details (also see [20, 74–76]). Here we stress that the escape rate is the inverse of the mean activation of a single particle [2]. Evidently, the AL universality still prevails for non-interacting particles. What happens to this universality when we incorporate many-body interactions? Here, we try to address this important question in different systems as discussed below.

Systems with excluded volume interactions

The symmetric simple exclusion process(SSEP): The SSEP is a lattice gas model, where each site is either occupied or not (see Fig. 2.1(a)). A particle at site i, jumps to the neighboring site j with rate $\eta_i(1-\eta_j)$ where η_i denotes the onsite occupancies. Despite its simplicity, the SSEP has been widely studied in the context of nonequilibrium statistical mechanics and has been used as a paradigmatic model for understanding the behavior of interacting particle systems in many phys-

[1] Assuming $t \gg L^2/D_0$ the diffusion time. For the short time limit, see [73].

[2] While our main goal is to asses the mean activation time of a single particle, in principle one can generalize our results to the case of the escape of all M particles from the trap.

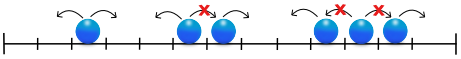

(a) The SSEP dynamics where each site can be occupied only by one particle.

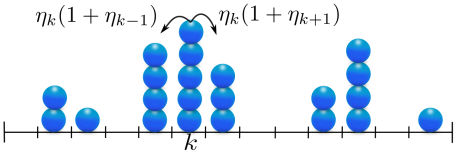

(b) The SIP dynamics where each site can have unbounded number of particles.

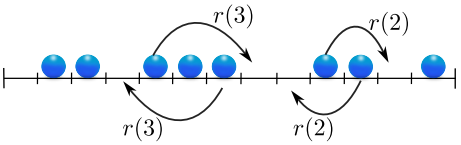

(c) The strong particles model where a quantum of k-particles can either move to the left or right available sites with a rate $r(k)$.

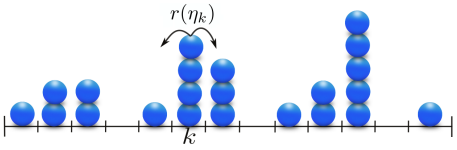

(d) The ZRP dynamics where many particles can occupy each lattice site. They can hop together from a site (k) with a rate $r(\eta_k)$ where η_k is the number of particles at the k-th site.

Figure 2.1: Schematic of the paradigmatic lattice gas models analyzed in this work: (a) the SSEP, (b) the SIP, (c) the strong particles model and (d) the ZRP.

ical and biological systems, e.g. traffic flow, tracer dynamics, protein synthesis, and gene regulation [77, 78]. The SSEP typically demonstrates genuine nonequilibrium behavior, e.g. a non-product steady state measure and long range nonequilibrium correlations [8, 11]. Furthermore, the SSEP is susceptible to exact solutions; microscopically via the Bethe ansatz and macroscopically through the MFT [47, 79–82].

The strong particles model(SPM): The strong particles model [83–85] is a lattice gas model, where each lattice site is either occupied or not. Blocks of k occupied sites can move in their entirety with rate $r(k)$ one step to the right or left (see Fig. 2.1(c)). This dynamics depicts that a particle is strong enough to push a whole line of particles – hence the name.

Systems without excluded volume interactions

The simple exclusion process(SIP): The SIP is a lattice gas model, where the particle occupancy at each site is unbounded. A particle at site i jumps to a nearest neigh-

boring site j with rate $\eta_i(1+\eta_j)$ where $\eta_{i,j}$ are the particle occupancies [79, 86–88] (see Fig. 2.1(b)). Namely, where the SSEP is the classical analog of Fermions, the SIP is the classical analog of Bosons. It is often the case where if the SSEP dynamics can be solved analytically, so can the corresponding SIP dynamics [79].

The zero range process(ZRP): The ZRP is a lattice gas model, where a particle at site i jumps to a neighboring site j with rate $r(\eta_i)$ where η_i is the occupancy at site i [48] (see Fig. 2.1(d)). That is, only onsite interactions are important. We have $r(0) = 0$ for the process to be well defined. Notice that the jump rates are robust enough to allow a mixture of attractive and repulsive interactions. The relation between $D(\rho)$ and $\chi(\rho)$ is given by $D(\rho) = \frac{d}{d\rho}\chi(\rho)$ (see Appendix F.3).

These are the systems that we study in this chapter. To understand the result consider an extended 1D system of interacting diffusing particles in a monotonically increasing potential $U(x)$ with initial mean density $\overline{\rho}_0 = M/L$, where M is the number of particles and L is the domain size. We show in this chapter that the mean time it takes for a particle to escape from the potential is given by the following generalized AL

$$\Phi_{\mathrm{MP}} \asymp \mathrm{e}^{-\Delta \mathrm{Ug}(\overline{\rho}_0)/\mathrm{D}_0}, \tag{2.1}$$

where g depends both on the density $\overline{\rho}_0$ and on the inter-particle interactions. Once again, we stress that Φ_{MP} is the particle escape rate, its inverse indicates the mean escape time of a single particle. By minimizing the particle configuration energy, one can show $g = 1 - U_{top}/\Delta U$ where U_{top} is the highest energy a particle can attain in the minimum energy configuration. The exponential form of the AL is still preserved. However, the salient point is the emergence of two universality classes. Whenever $\Delta U/D_0$ is large, and no excluded volume interactions take place, the minimum energy configuration compresses all the particles at the origin, keeping the AL universality intact with $g = 1$. However, excluded volume effects change the minimum energy configuration and thus g strongly depends on the particle density.

This implies on one hand the breakdown of the AL universality as g depends on the shape of the potential. On the other hand, notice that g is independent of the dynamics at play. That is, we have identified a *new universality class* – the excluded volume universality.

To illustrate the generalized AL, consider the paradigm of the symmetric simple exclusion process (SSEP) where the inter-particle interaction is hard-core exclusion [77]. Minimizing the particle configuration energy implies that they are tightly packed around the potential minimum, resulting in $g < 1$ [see Fig. 2.2(a), details later]. Therefore, the excluded volume imposes a shorter mean escape time. Eq. (2.1) is the central result of this chapter and we will demonstrate it for a class of diffusive interacting systems, within the framework of the macroscopic fluctuation theory (MFT) [8] (also see Appendix A).

To illustrate the generalized AL, consider the paradigm of the SSEP, or the SPM, which exhibit excluded volume interactions. Minimizing the particle configuration energy implies that they are tightly packed around the potential minimum [see Fig. 2.2(a)]. In this minimum energy configuration, the topmost particle is at the potential level denoted by $U_{\rm top}$ in Fig. 2.2(a). Therefore, this particle does not have to overcome the full barrier ΔU. Instead, it effectively experiences a reduced barrier $\Delta U - U_{\rm top}$. Therefore, the excluded volume imposes a shorter mean escape time. On the other hand, for systems with no excluded volume interactions, like the SIP and the ZRP, $U_{\rm top} = 0$ (see Fig. 2.2(b)). Therefore, in order to cross the barrier, a particle has to overcome the full barrier ΔU. Eq. (2.1) is the central result of this chapter and we will demonstrate it for a class of diffusive interacting systems discussed above, within the framework of the macroscopic fluctuation theory (MFT) [8] (also see Appendix A).

We confine an interacting-diffusive gas consisting of M particles in a trap of size L. After doing the diffusive rescaling (see Appendix A), we denote the rescaled

trapping potential by $U(x)$. At coarse grained level, in the large L limit, the system is described by the following fluctuating hydrodynamics equation:

$$\partial_s \rho = -\partial_x j \tag{2.2a}$$

$$j = J(\rho) + \sqrt{2D_0\chi/L}\,\xi(x,s), \tag{2.2b}$$

$$J(\rho) = -D(\rho)\partial_x\rho - \chi(\rho)\beta\partial_x U. \tag{2.2c}$$

where, $D_0 = 1/\beta = k_B T$. $\rho(x,s), j(x,s)$ are the density and current density respectively. Here $x \in [0,1]$ and $s \in [0,t]$ are diffusively rescaled. The functions $D(\rho)$ and $\chi(\rho)$ represent, respectively, the diffusivity and mobility associated with the underlying microscopic dynamics. The stochastic term $\xi(x,s)$ is a Gaussian white noise with zero mean and delta correlations in both space and time, satisfying $\langle \xi(x,s)\xi(x',s')\rangle = \delta(x-x'), \delta(s-s')$ – also see Appendix A.

Building on the fluctuating hydrodynamics equation, the fundamental formula of MFT asserts that the path probability is given by

$$\text{Prob}\left[\{\rho, j\}\right] \asymp \exp\Big[-\frac{L}{D_0}\int_0^t ds \int_0^1 dx\, \frac{\left(j - J(\rho)\right)^2}{4\chi}\Big]\delta(\partial_s\rho + \partial_x j) \tag{2.3}$$

where $\asymp$ indicates possible possible logarithmic corrections. The delta functional enforces the continuity constraint, $\partial_s\rho + \partial_x j = 0$, ensuring that only those trajectories $\{\rho, j\}$ which satisfy this constraint contribute to the path probability.

Further, we assume that the particles are constrained between one reflecting and one absorbing wall at $x = 0$ and $x = 1$ respectively. Thus, $\mathcal{S}(t)$, the survival probability of the particles to stay inside the region upto time t can be written as a conditional sum over all the paths Prob$[\{\rho, j\}]$ (see Eq. (2.3)) that satisfy the following boundary conditions

$$J(\rho)|_{x=0} = \rho|_{x=1} = 0, \tag{2.4}$$

and the mass conservation in the system

$$L \int dx\, \rho(x,t) = M. \tag{2.5}$$

The constraint in Eq. (2.5) enforces conservation of the total number of particles in the system, which is essential since our objective is to compute the survival probability of the entire system, i.e., all M particles, up to time t. This survival probability, in turn, determines the escape rate associated with the first particle exiting the system, which is the central quantity of interest.

Within the MFT, one expects $\mathcal{S}(t) \asymp \mathrm{e}^{-t\,\Phi}$, where computation of Φ ($\Phi_{\rm NI}$ or $\Phi_{\rm MP}$) reduces to a minimization problem of finding an optimal fluctuation $\{\rho, j\}$ that satisfy the above mentioned constraints. Note that the optimal fluctuation governs Φ due to the large L saddle dominated probability in Eq. (2.3). However, the minimization problem still remains hard. To address that, we use the additivity principle, that was introduced in [89] and proved as a useful tool in evaluating large deviations [8] (also see [79, 80, 84, 90, 91]). The additivity principle posits that the optimal fluctuation density is time-independent, reducing the complexity of finding the optimal fluctuations.

For a $1D$ system, the additivity principle assumption $\rho(x,t) = \rho(x)$ implies $j(x,t) =$ const due to the continuity equation. However, const $= 0$ since the current vanishes at the boundaries. Finding Φ then reduces to the following minimization problem

$$\Phi = \frac{D_0 L}{4} \min_{\rho(x)} \int dx\, \mathcal{L}(\rho, \partial_x \rho), \;\; \mathcal{L} = \frac{J(\rho)^2}{\chi} - 4\Lambda(\rho - \overline{\rho}_0), \tag{2.6}$$

where $\rho(x)$ is subjected to Eq. (2.4) and Λ is a Lagrange multiplier ensuring mass conservation $\overline{\rho}_0 = M/L = \int dx\, \rho(x)$. It is important to emphasize that the additivity principle has converted a hard dynamical optimization problem (see Eq. (2.3)) into a simpler static optimization problem over the time-independent density profile $\rho(x)$.

The minimization problem in Eq. (2.6) then boils down to solving an Euler-Lagrange (EL) equation with the Lagrangian $\mathcal{L}$. Using the transformation [73, 92] (we will henceforth refer to this as F-transformation)

$$F(\rho) = \int_0^\rho dz \frac{D(z)}{2\sqrt{\chi(z)}}, \tag{2.7}$$

the resulting EL reads

$$-\partial_{xx}F + \frac{1}{8}(\partial_x \tilde{U})^2 \chi' - \frac{1}{2}\sqrt{\chi}\partial_{xx}\tilde{U} = \Lambda \frac{\sqrt{\chi}}{D}, \tag{2.8}$$

where $\chi = \chi(\rho[F])$ and $\chi' = \delta\chi/\delta F$ and $\tilde{U} = U/D_0$ (recall that $D_0 = 1/\beta = k_B T$). The resulting boundary conditions inherited from (2.4) are

$$J_F|_{x=0} = \rho[F]|_{x=1} = 0 \tag{2.9}$$

with a rescaled current

$$J_F = \partial_x F + \frac{1}{2}\chi^{1/2}\partial_x \tilde{U}. \tag{2.10}$$

Thus, the survival probability can be estimated via (2.6) as

$$\Phi = D_0 L \int dx\, J_F^2, \tag{2.11}$$

where F is the solution of (2.8).

Before discussing the interactions, it is instructive to re-derive the results for non-interacting particles. Indeed, here $D = 1, \chi = \rho$ so that $\rho = F^2$ and (2.8) recovers $\hat{H}_{FP}F = D_0 \Lambda F$, which is the eigen-value problem for the non-interacting system. Skipping details, one can show that $\Phi_{\rm NI} = D_0 L \bar{\rho}_0 \Lambda$ which implies that $D_0\Lambda$ is the ground state energy of $\hat{H}_{FP}$ (see Appendix C.4).

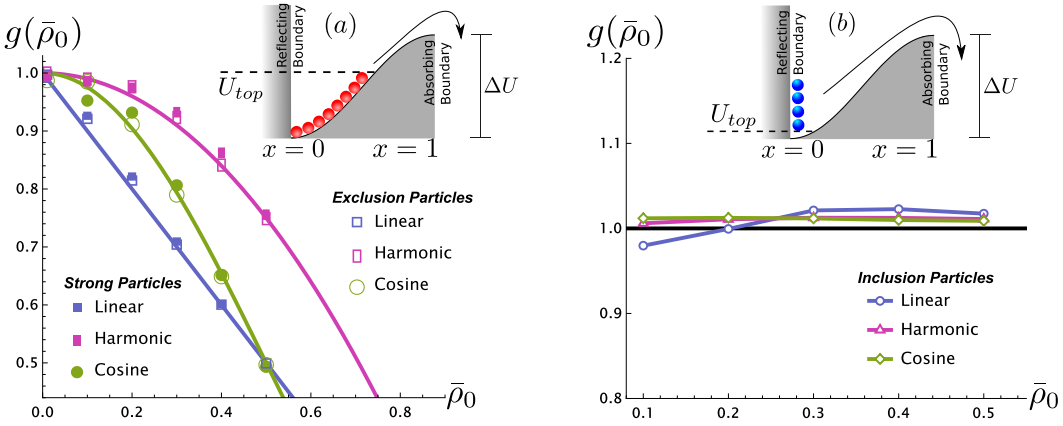

Figure 2.2: **The generalized AL for interacting diffusive systems.** The minimal energy configuration for the SSEP, strong particles model, and SIP is sketched in the sub-figures of (a) and (b) correspondingly. For the excluded volume models, the particles pack tightly, leading to $U_{top} = U(\overline{\rho}_0)$. For the SIP, all the particle can accumulate on the potential minimum at $x = 0$, leading to $U_{top} = 0$. The g function is tested numerically, as a function of $\overline{\rho}_0$, with three potentials $U(x)$: linear $\Delta U x$, harmonic $\Delta U x^2$ and cosine $\frac{1}{2}\Delta U(1-\cos(\pi x))$. We confirm numerically, for the SSEP and the strong particles model $g = 1 - U(\overline{\rho}_0)/\Delta U$ (left panel) and for the SIP $g = 1$ (right panel), as predicted by Eq. (2.1). Both predictions are well fitted up to the expected numerical errors. We refer to Appendix C for more details.

For short range interactions, and in the limit of a dilute system, i.e. $\overline{\rho}_0 \to 0$, suggests interactions become negligible. Indeed in this limit, $F \to 0$. Thus, Eq. (2.8) can be linearized in F, leading to the non-interacting case. Thus for dilute systems, the AL is recovered. In what follows, in order to justify the generalized AL in Eq. (2.1), we turn to study several interacting systems.

Notation: Before proceeding to the subsequent sections and chapters, we clarify the notation used throughout the thesis. The symbol Φ_{MP} denotes the escape rate for interacting diffusive systems. More specifically, Φ_{SSEP}, Φ_{SIP}, Φ_{SPM} and Φ_{ZRP} represent the escape rates for the SSEP, the SIP, the strong particles model and the ZRP respectively. The notation Φ_{NI} is used for the escape rate of non-interacting particles. When no subscript is specified, Φ is used in a generic sense to denote the escape rate, with its precise meaning inferred from the context.

2.2 Excluded volume universality

The objective of this section is to demonstrate the emergence of a universality class associated with diffusive systems exhibiting excluded-volume interactions. We refer to this as the excluded-volume universality class. In what follows, we establish this universality within two representative models with excluded-volume effects, namely the symmetric simple exclusion process and the strong particles model.

2.2.1 The symmetric simple exclusion process (SSEP)

For the SSEP, $D = 1, \chi = \rho(1-\rho)$ [11] (also see Appendix F.1). The transformation to F leads to $\rho = \sin^2 F$. We restrict F to the range $[0, \pi/2]$ to ensure a positive $\chi^{1/2} = \frac{1}{2}\sin 2F$. While χ, χ' in (2.8) becomes explicit, a solution for arbitrary potential is challenging. Fortunately, an analytical solution can be obtained for the linear potential $\tilde{U}(x) = \Delta\tilde{U}x$ ($\tilde{U} = U/D_0$). In that case (2.8) is simply an autonomous equation. With the transformation $y = \cos 2F$, and by assuming that the density as well as y are monotonous functions, (2.8) can be reduced to a first order differential equation (see Appendix C.2)

$$\begin{aligned} \frac{dy}{dx} &= \frac{1}{2}\Delta\tilde{U}\sqrt{1-y^2}\sqrt{1-y^2+8\lambda(y-y_0)}, \\ & y_0 = y|_{x=0}, \quad y_1 = y|_{x=1} = 1, \end{aligned} \tag{2.12}$$

where $\lambda = \Lambda/\Delta\tilde{U}^2$. Note that $-1 \leq y_0 \leq 1$. Here $y_0 \to 1(-1)$ implies that the density at the reflecting boundary is approaching zero (unity).

Eqs. (2.11) and (2.12) constitute an implicit solution of the survival probability, denoted by Φ_{SSEP}, for the SSEP. However, it is worth stressing that one need not explicitly solve y (and thus F) in order to obtain Φ_{SSEP}. Skipping details from

Appendix C, we obtain

$$\frac{\Phi_{\rm SSEP}}{D_0 L} = \frac{C_0}{2}\left(y_0 - 1 + C_0 - C_2 + 4\lambda(C_1 - y_0 C_0)\right),$$
$$\text{where} \quad C_k = \int_{y_0}^{1} dy \frac{y^k}{\sqrt{1-y^2}\sqrt{1-y^2+8\lambda(y-y_0)}}, \tag{2.13}$$

for $k = 0, 1, 2$. Fortunately, the C_k integrals are analytical and involve elliptic functions. Furthermore, $\Phi_{\rm SSEP}$ is given in terms of (λ, y_0) which are implicit functions of $\Delta\tilde{U}$ and $\overline{\rho}_0$.

To make the relations explicit, we notice that direct integration of (2.12) leads to $C_0 = \Delta\tilde{U}/2$. Also, recalling that $\overline{\rho}_0 = \int dx \sin^2 F$ implies that $2\overline{\rho}_0 = 1 - C_1/C_0$. The regime of large $\Delta\tilde{U}$ is supported by $0 < 1 + y_0 \ll \lambda \ll 1$. In these limits and to leading order $\lambda = 2\mathrm{e}^{-\Delta\tilde{U}(1-\overline{\rho}_0)}$ and $(1+y_0) = \mathrm{e}^{-\Delta\tilde{U}\overline{\rho}_0}$. Finally, we have

$$\Phi_{\rm SSEP} = D_0 L A \mathrm{e}^{-\Delta\tilde{U}(1-\overline{\rho}_0)}, \tag{2.14}$$

where A is a polynomial function of $\overline{\rho}_0$ and $\Delta\tilde{U}$ (see Appendix C.2).

At this point, we connect the above with our announced result (2.1). Eq. (2.14) implies $g = 1 - \overline{\rho}_0$ for the linear potential. In the exclusion process, the system's energy is minimized if the particles are ordered as close to the potential minimum as possible. Consequently, the minimum energy occurs when the system is fully occupied between $x = 0$ and $x = \overline{\rho}_0$, and therefore $U_{top} = U(x = \overline{\rho}_0)$ (see Fig. 2.2(a)).

Although solving Eq. (2.8) is hard for generic monotonous potentials, the same physical arguments can be given to infer the generalized AL. Indeed, the minimum energy attained by tight packing the exclusion particles in monotonous potentials, lead to $U_{top} = U(x = \overline{\rho}_0)$. To demonstrate this behavior, we employ a standard shooting method algorithm to solve the eigen-problem (2.8) for various potentials (see Appendix C.5 for more details). The numerical results shown in Fig. 2.2 pro-

vide an excellent agreement with Eq. (2.1) thus validating the generalized AL for arbitrary monotonous potentials with excluded volume effects. In the absence of excluded volume effect, Eq. (2.1) implies $g = 1$. This is indeed the case for the reflected Brownian motion, where particles cannot overtake one another, following from Jepsen line arguments [93–95]. The reflected Brownian motion is precisely the limit of the SSEP at vanishing $\overline{\rho}_0$, in agreement with $g = 1$.

2.2.2 The strong particles model (SPM)

The strong particles model is a gradient type model. This implies an analytic calculation of the diffusivity [83, 85] (see also Appendix F.4). In our case,

$$D = \sum_{k=1}^{\infty} k^2 r(k) \rho^{k-1}. \tag{2.15}$$

As long as the rates allow all possible configurations, we have the free energy density $f(\rho) = \rho \log \rho + (1-\rho)\log(1-\rho)$. This implies that the mobility is given by (see also Appendix F.4)

$$\chi = \rho(1-\rho)D. \tag{2.16}$$

Clearly, for $r(k=1) = 1$ and $r(k>1) = 0$ we reduce to the SSEP. Here, we choose $r_k = 1/k^2$ to simplify the F transformation. This gives $\chi = \rho, D = 1/(1-\rho)$. We find that $\rho = \chi = \tanh^2 F$ with $D = \cosh^2 F$. Indeed, Fig. 2.2 confirms that g is identical for the SSEP and the strong particles model, revealing they both belong to the excluded volume universality.

2.3 Arrhenius universality.

In this section, we demonstrate that diffusive systems without excluded-volume interactions belong to the Arrhenius universality class. In such systems, the exponential contribution to the escape rate depends solely on the barrier height and the temperature. We establish this universality by analyzing two representative models, namely the simple inclusion process and the zero-range process.

2.3.1 The simple inclusion process (SIP)

In the literature, one can find numerous studies on the SIP as a model that facilitates condensation [96, 97]. In this thesis, we focus on diffusive transport, and thus avoid the condensation region. Hence, the SIP densities are assumed low enough to avoid any condensation transition. For $\overline{\rho}_0 < 0.6$, the absence of condensation is numerically verified.

The interaction among the particles is attractive. Therefore, naively, one might guess that attractive interactions decrease the escape rate and therefore ultimately result in $g > 1$. In contrast, we demonstrate here that $g = 1$. Namely, the SIP, lacking excluded volume effects belongs to the Arrhenius universality class and satisfies Eq. (1.5).

For the SIP, one finds $D = 1, \chi = \rho(1+\rho)$ (see Appendix F.2). The F-transformation implies $\rho = \sinh^2 F$. Notice that unlike the SSEP, F is unbounded for the SIP. Similarly to the SSEP analysis, one can explicitly write the Euler-Lagrange equation (2.8), but an explicit solution is again challenging for an arbitrary potential. However, some analytical progress can be made for the linear potential. Skipping details,

we find (see Appendix C.3)

$$\Phi_{\mathrm{SIP}} = D_0 L A \mathrm{e}^{-\Delta\tilde{U}}, \tag{2.17}$$

where A once again is a polynomial function of $\overline{\rho}_0, \Delta\tilde{U}$ (see Appendix C.3).

Eq. (2.17) remarkably coincides with the single particle AL noting that there is no slowdown in the escape. This indeed stems from the underlying physics of the SIP, where the attractive interactions imply that the minimum energy configuration is attained when all the particles bunch at the potential minimum. Comparing Φ_{SIP} with Eq. (2.1) results in $g = 1$. In fact, this holds for any monotonous potential. To demonstrate this fact, we employ our shooting algorithm to solve (2.8) for different potentials. The numerical results are illustrated in Fig. 2.2 validating the AL for SIP regardless of the particle density $\overline{\rho}_0$. We should stress that the simplicity of Eq. (2.17) can be deceptive since there is no *simple* or *trivial* way to derive it.

2.3.2 The zero-range process (ZRP)

Assuming χ to be polynomial in ρ, the ZRP indeed conforms to (2.1) with $g = 1$. Fig. 2.3 plots numerical $g(\overline{\rho}_0)$ for a linear potential $U(x) = \Delta U x$ a harmonic potential $U(x) = \Delta U x^2$, and a cosine potential $U(x) = \Delta U[1 - \cos(\pi x)]/2$. We consider the ZRP characterized within the MFT by $\chi = \rho(1 + \rho)$. For all three potentials, the numerical results are in agreement with the theoretical prediction, yielding values of g that remain equal to unity within numerical accuracy.

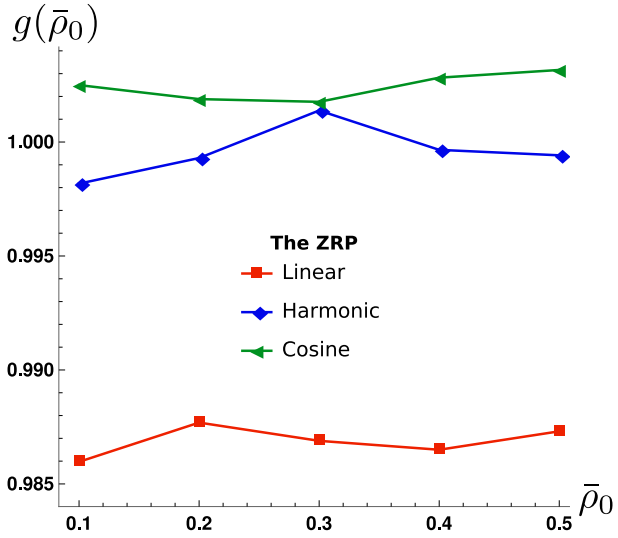

Figure 2.3: The plot extracts g as a function of the mean density $\bar{\rho}_0$ for ZRP defined by $\chi = \rho(1+\rho)$. These particles experience a linear $U/\Delta U = x$, harmonic $U/\Delta U = x^2$ or a cosine potential $U/\Delta U = (1-\cos \pi x)/2$. Clearly, $g = 1$ up to numerical errors as expected.

2.4 Discussion.

Understanding escape times in a thermal activation process while accounting for many-body interactions is at the heart of this chapter. To this end, we have studied the survival probability of interacting particles with diffusive dynamics in a potential trap. In the limit of weak thermal fluctuations $\Delta U \gg D_0$, we show, using the seminal macroscopic fluctuation theory, that the Arrhenius law can be generalized (Eq. (2.1)) with $\Delta U g$ an effective activation energy. Importantly, we reveal that the escape problem in lattice gas models branches into two universality classes. We demonstrate our result in five distinct paradigmatic models. Particle models with excluded volume exhibit a decrease in g leading to a facilitated escape from the potential. Importantly g is independent of the interaction. On the other hand, whenever excluded volume effects are not present, we reach quite surprisingly and non-trivially to an effective single particle problem. Thus, the canonical AL applies for processes without excluded volume effects. It should be stressed that albeit its technical simplicity and intuitively appealing physical interpretations, any attempts

to generalize the insight gained from single particle AL to many particles with arbitrary interactions remains exorbitantly challenging. Furthermore, the generalized AL holds in store quite a few surprises.

Naively, one expects that the generalized AL would be more restrictive from an experimental stand point. However, Eq. (2.1) suggests the opposite with two immediate interesting directions within the excluded volume universality class. Consider a narrow tube serving as a $1D$ transport channel for colloids, where both the trap and the interactions can be manipulated externally. Here, the new universality class suggests that such changes would not affect escape rates from the potential trap. However, changes in the colloids density, or varying the shape of the potential (modulated by, e.g. optical tweezers), while keeping ΔU fixed, will result in different escape rates. Therefore, measurement of escape rates allows to infer the particle density in the trap as we change the potential, or vice versa. See [98–101] and especially [33] for similar inference problems.

Beyond these applications, this work opens new avenues of research. First, it will be important to extend Eq. (2.1) to include arbitrary potential landscape, possibly also to higher dimensions [102, 103].

A yet unexplored path is to consider the AL for multi-species particles, where D, χ become matrices [104]. It will be worth investigating whether such inter-species interactions can speed up the escape rate of a complex activation process.

Chapter 3

Emerging universality classes in thermally assisted activation of interacting diffusive systems: A perturbative hydrodynamic approach

The contents of this chapter has been published in [105].

In Chapter 2, we derived Arrhenius law for interacting diffusive systems using the framework of the macroscopic fluctuation theory (MFT). Our analysis revealed the existence of two distinct universality classes: systems without excluded-volume interactions fall within the Arrhenius universality class, whereas systems with excluded-volume interactions belong to the excluded-volume universality class. The results were demonstrated with the aid of numerical analysis. In this chapter, we present a perturbative hydrodynamic approach to analytically validate the existence and range of validity for the two universality classes.

More specifically, in Chapter 2, the Euler–Lagrange equation [Eq. (2.8)], arising from the underlying variational minimization problem, could not be solved analytically for arbitrary potential landscapes. In what follows, we address this limitation by adopting an alternative analytical strategy. The idea is to bypass the need for an

exact solution of the Euler–Lagrange equation by employing a perturbative approach constructed around the thermal equilibrium. This enables a systematic analytical treatment of the minimization problem.

3.1 A perturbation theory close to equilibrium

We are now in a position to address the main claim of this work; diffusive particle systems, within the framework of the MFT belong either the Arrhenius universality class, or the excluded volume universality class. In this section, we present the proof.

Importantly, the proof provided here has to be carried out independently for each dynamics D, χ. Therefore, we start by stating the essence of the proof, and only then continue to demonstrate it for: non-interacting particles, the symmetric simple exclusion process (SSEP), the strong particles model, the simple inclusion process (SIP) and finally the family of zero-range processes (ZRPs).

The premise of our method is to notice that at the $\Delta U \gg D_0$ limit, the escape rate $\Phi \ll 1$. Namely, the escape rate of particles from a deep trap is small. Considering an equilibrium density profile $\rho_{\rm eq}$ (correspondingly $F_{\rm eq}$), where $J(\rho_{\rm eq}) = 0$ (correspondingly $J_{F_{\rm eq}} = 0$) implies $\Phi = 0$ directly from Eqs. (2.10) and (2.11). The equilibrium density profile is small but non vanishing at the absorbing boundary, in contradiction with the boundary conditions (2.9). Therefore, it seems plausible that the optimal fluctuation can be written as a perturbative expansion around the equilibrium fluctuation. Let us construct this perturbation theory.

3.1.1 The essence of the proof

In order to estimate the escape rate Φ, we need to solve the Euler-Lagrange equation (2.8) subjected to the boundary conditions (2.9). The premise of the method is

that the optimal profile F can be approximated by invoking a perturbative analysis around the equilibrium setup

$$F = F_{\text{eq}} + \omega \delta F + O(\omega^2), \tag{3.1}$$

where ω is a small parameter, yet to be determined, and δF is an order 1 perturbation. It is important to state from the get-go that it is hard to carry out the perturbation theory to the next order. Nevertheless, it will prove useful for the task at hand, as $\Phi \asymp \omega^2$ to leading order.

First, we explicitly find F_{eq} as the solution of $J_{F_{\text{eq}}} = 0$. The equilibrium solution F_{eq} naturally depends on the particle mass in the system $M = L\overline{\rho}_0$. Therefore F_{eq} is determined from $J_{F_{\text{eq}}} = 0$ up to a constant we denote by A. Then, it is important to find $A = A(\frac{\Delta U}{D_0}, \overline{\rho}_0)$, where $D_0 = k_B T$. We expect this is typically possible analytically at the limit of large $\Delta U / D_0$.

F_{eq}, the equilibrium component, satisfies the reflecting boundary condition, but it does not account for the absorbing boundary condition. We posit that the correction term $\omega \delta F$ is responsible to mend the absorbing boundary condition. Namely, $F_{\text{eq}} + \omega \delta F|_{x=1} = 0$. More precisely, we fix $\delta F|_{x=1} = -1$ so that

$$\omega = F_{\text{eq}}|_{x=1}. \tag{3.2}$$

This implies that to leading order in ω

$$\Phi = L D_0 \omega^2 \min_{\delta F} \int dx \, (\partial_x \delta F + \frac{\chi'}{4 D_0 \chi^{1/2}} \partial_x U \delta F)^2, \tag{3.3}$$

where $\chi = \chi(F_{\text{eq}})$. The new minimization problem of δF is in no way simpler than the original problem and we make no attempt to solve it. Instead, we notice δF is of order 1 and therefore the integral in (3.3) is typically non-vanishing and leads to

a polynomial function of $\Delta U/D_0$. Therefore, it is ω that determines the exponential decay of Φ.

In simple words, using this perturbative approach, we have thus reduced the problem from solving a hard minimization problem on F, to finding the proper scaling ω. Finally, after determining ω, we recover $\Phi \asymp \omega^2$ to recover the generalized AL at the limit where $\Delta U/D_0 \gg 1$.

In what follows, we implement this methodology for a set of paradigmatic lattice gas models.

3.1.2 Non-interacting particles

Within the MFT formalism, $D = 1$, and $\chi = \rho$ for non-interacting diffusive particles. In this case, the F transformation (2.7) implies $\rho = F^2$. With the above in mind, we write the escape rate for non-interacting particles $\Phi_{\rm NI}$, the resulting Euler-Lagrange equation, and the boundary conditions

$$\begin{aligned} \Phi_{\rm NI} &= D_0 L \int dx (\partial_x F + \frac{1}{2D_0} F \partial_x U)^2 + \Lambda(F^2 - \overline{\rho}_0), \\ & \partial_x F + \frac{1}{2D_0} F \partial_x U|_{x=0} = F|_{x=1} = 0. \end{aligned} \tag{3.4}$$

According to the recipe of Sec. 3.1.1, we posit (3.1), and for a vanishing $J_{F_{\rm eq}}$, we find

$$\begin{aligned} F_{\rm eq} &= A\, {\rm e}^{-\frac{\rm U(x)}{\rm 2D_0}}, \quad \text{and} \\ A^2 &= \frac{\overline{\rho}_0}{\int dx\, {\rm e}^{-\rm U(x)/D_0}}, \end{aligned} \tag{3.5}$$

where A is obtained from the mass conservation at the leading order. At the large $\Delta U/D_0$ limit, we can explicitly evaluate $A^2 = \overline{\rho}_0 \frac{\partial_x U(x=0)}{D_0} + O(1)$, provided the first derivative around $x = 0$ is non-vanishing. More generally, when $\partial_x^k U(x = 0) = 0$ for

$k < n$, one finds $A^2 \propto \overline{\rho}_0(\Delta U/D_0)^{1/n}$ up to subleading contributions in $\Delta U/D_0$.

From (3.2), satisfying the absorbing boundary condition, we find

$$\omega = A\,\mathrm{e}^{-\frac{\Delta \mathrm{U}}{2\mathrm{D}_0}}. \tag{3.6}$$

This choice is justified if ω is indeed small. Since A is polynomial in $\Delta U/D_0$, and $\overline{\rho}_0$ is finite, we confirm $\omega \ll 1$ at large $\Delta U/D_0$ and the perturbation theory is justified. Moreover, we verify that

$$\begin{aligned} \Phi_{\mathrm{NI}} &= D_0 L \omega^2 \mathrm{Poly}(\Delta \mathrm{U}/\mathrm{D}_0) \\ &= D_0 M \mathrm{Poly}(\frac{\Delta \mathrm{U}}{\mathrm{D}_0})\mathrm{e}^{-\frac{\Delta \mathrm{U}}{\mathrm{D}_0}}, \end{aligned} \tag{3.7}$$

where the polynomial contribution comes from both the ω^2 term and from the integral in (3.3). Therefore, we have reconstructed the famous AL for non-interacting particles. In what follows, we show that the same methodology, with a tad more technicality, re-affirms the classification to two AL universality classes; differentiating between processes with and without excluded volume.

3.1.3 The symmetric simple exclusion process (SSEP)

In this subsection, we focus on inferring g of (2.1) for the SSEP. (For microscopic details of SSEP, see Appendix F.1.) It will demonstrate that the SSEP belongs to the excluded volume universality class, as predicted by (2.1).

We recall that within the MFT formalism, the SSEP is defined by $D = 1$, and , $\chi = \rho(1-\rho)$. The F transformation (2.7) implies $\rho = \sin^2 F$ for the SSEP. Let us, once again, collect the escape rate Φ_{SSEP} and the boundary conditions for the SSEP

[1]

$$\begin{aligned}
\frac{\Phi_{\rm SSEP}}{D_0 L} &= \min_F \int dx\, J_F^2 + \Lambda(\sin^2 F - \overline{\rho}_0), \\
F|_{x=1} &= \partial_x F + \frac{1}{4D_0} \sin 2F \partial_x U|_{x=0} = 0, \\
J_F &= \partial_x F + \frac{1}{4D_0} \sin 2F \partial_x U.
\end{aligned} \tag{3.8}$$

Our methodology states that we need to find $F_{\rm eq}$ explicitly. Imposing $J_{F_{\rm eq}} = 0\ \forall x$ implies

$$F_{\rm eq} = \arctan(A\, {\rm e}^{-{\rm U}/2{\rm D}_0}). \tag{3.9}$$

A is inferred from the mass conservation $\overline{\rho}_0 = \int dx\, \sin^2 F_{\rm eq}$, i.e.

$$1 - \overline{\rho}_0 = \int dx\, \frac{1}{1 + A^2 {\rm e}^{-{\rm U(x)}/{\rm D}_0}}. \tag{3.10}$$

At large $\Delta U/D_0$ values, and assuming monotonous potentials, it is possible to evaluate $A^2 = {\rm e}^{{\rm U}(\overline{\rho}_0)/{\rm D}_0}$, up to subleading corrections. Indeed, we notice that [2]:

$$\begin{aligned}
\int \frac{dx}{1 + A^2 {\rm e}^{-{\rm U(x)}/{\rm D}_0}} &= \left(\int_0^{\overline{\rho}_0} + \int_{\overline{\rho}_0}^1 \right) \frac{dx}{1 + {\rm e}^{\frac{{\rm U}(\overline{\rho}_0) - {\rm U(x)}}{{\rm D}_0}}} \\
&\approx O(\frac{D_0}{\Delta U}) + 1 - \overline{\rho}_0.
\end{aligned} \tag{3.11}$$

Now that we have evaluated A, we recall that (3.2) implies

$$\begin{aligned}
\omega &= F_{\rm eq}|_{x=1} = \arctan A {\rm e}^{-\Delta {\rm U}/2{\rm D}_0}, \\
\Phi_{\rm SSEP} &= D_0 L {\rm Poly}(\Delta {\rm U}/{\rm D}_0) \omega^2 \\
&= D_0 L {\rm Poly}(\Delta {\rm U}/{\rm D}_0) {\rm e}^{-\Delta {\rm Ug}/{\rm D}_0},
\end{aligned} \tag{3.12}$$

for deep potentials, and with $g = 1 - U(\overline{\rho}_0)/\Delta U$ for monotonous U as suggested

[1] Here we refrain from writing the Euler-Lagrange equation as the scaling of ω stems from the absorbing boundary condition.

[2] The subleading term $D_0/\Delta U$ can change to a different power law if $\partial_x U|_{x=0}$ vanishes.

in [72]. Note that δF is of order 1 and thus the polynomial contributions arise from the integral. Moreover, for a finite density $\omega^2 = \arctan \mathrm{e}^{-\Delta \mathrm{Ug}/\mathrm{D}_0} \ll 1$, thus justifying the perturbative approach.

We have shown that this perturbative scheme is sufficient to capture the generalized Arrhenius law in monotonous potentials. The extension to non-monotonous potentials can be pursued by the perturbative scheme and amounts to re-evaluating the integral (3.11). While non-monotonous potentials lead to interesting results on their own right, a focused study will be presented in Chapter 4.

We have verified for the SSEP the main claim of (2.1). The excluded volume results in $g < 1$. In what follows, we show that even in the case of a more complex dynamics than the SSEP, involving excluded volume effects, we still recover the same g given by (2.1). Namely, processes in the excluded volume universality class lead to the same g, independent of the dynamics.

3.1.4 The strong particles model (SPM)

We recall from Chapter 2 that for strong particles, the rate $r(k) = 1/k^2$ leads to $D = 1/(1-\rho)$ with $\chi = \rho$. Furthermore, the F transformation (2.7) leads to $\rho = \chi = \tanh^2 F$ with $D = \cosh^2 F$.

Collecting the setup for the strong particles model, we have

$$\begin{aligned} \frac{\Phi_{\mathrm{SPM}}}{D_0 L} &= \min_F \int dx\, J_F^2 + \Lambda(\tanh^2 F - \overline{\rho}_0), \\ F|_{x=1} &= \partial_x F + \frac{1}{2D_0} \tanh F \partial_x U|_{x=0} = 0, \\ J_F &= \partial_x F + \frac{1}{2D_0} \tanh F \partial_x U. \end{aligned} \tag{3.13}$$

Setting $J_{F_{eq}} = 0$, we find $F_{eq} = \operatorname{arcsinh} A \mathrm{e}^{-\mathrm{U}/2\mathrm{D}_0}$, where A is determined by mass

conservation

$$\overline{\rho}_0 = \int dx \tanh^2 F_{eq} = \int dx \frac{1}{1 + A^{-2} \mathrm{e}^{\mathrm{U(x)/D_0}}}. \tag{3.14}$$

For large $\Delta U/D_0$, and for monotonous potentials, we can evaluate $A^2 = \mathrm{e}^{\mathrm{U}(\overline{\rho}_0)/\mathrm{D_0}}$.

Now, we have from (3.2) that $\omega = \operatorname{arcsinh} A\mathrm{e}^{-\Delta \mathrm{U}/2\mathrm{D_0}}$, leading to the escape rate for deep potentials

$$\Phi_{\mathrm{SPM}} = D_0 L \mathrm{Poly}(\Delta \mathrm{U}/\mathrm{D_0}) \mathrm{e}^{-\Delta \mathrm{Ug}/\mathrm{D_0}}, \tag{3.15}$$

where $g = 1 - U(\overline{\rho}_0)/\Delta U$ as expected. To conclude, g is identical for the SSEP and the strong particles model. They both belong to the excluded volume universality class.

We verify numerically that the SSEP and strong particles model both belong to the excluded volume universality class. See Fig. 3.1.

We have established the excluded volume universality class, where g is independent of the type of interactions. We move onwards to analyze the simple inclusion process (SIP), which involves attractive interactions, but no excluded volume effects. This, in order to argue that even with interactions, but no excluded volume effects, the process lies within the Arrhenius universality.

3.1.5 The simple inclusion process (SIP)

Within the MFT framework, the SIP is captured by $D = 1$, and $\chi = \rho(1 + \rho)$. The F transformation (2.7) reads $\rho = \sinh^2 F$. We therefore recover

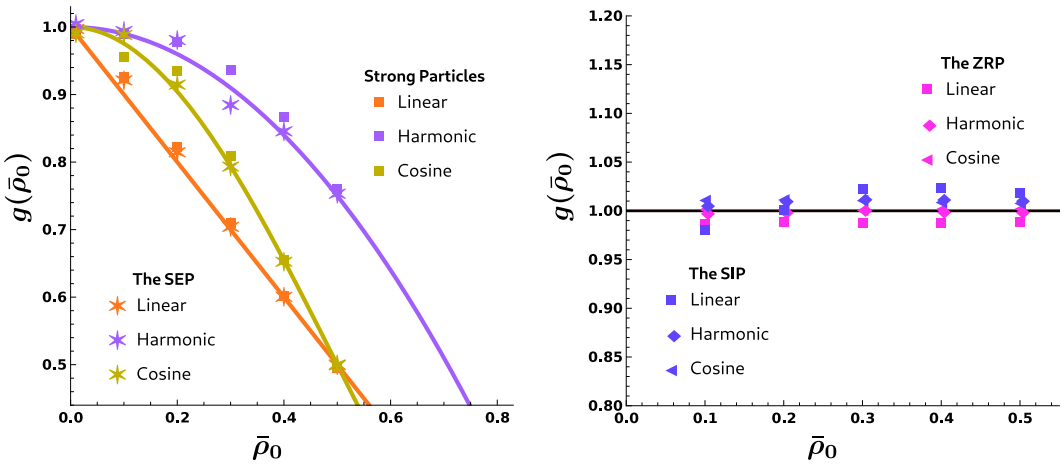

Figure 3.1: Numerically determining Φ [Eq. (2.11)] subjected to the boundary condition in Eq. (2.9). The two panels present g as a function of the particle density in the trap for three potentials: the linear potential $U/\Delta U = x$, the Harmonic potential $U/\Delta U = x^2$ and the Cosine potential $U/\Delta U = \frac{1}{2}(1 - \cos \pi x)$. The left plot presents g for the SSEP and the strong particles model, both falling within the excluded volume universality class. For the monotonous potentials under study, $g = 1 - U(\bar{\rho}_0)/\Delta U$ as obtained from the minimum energy configuration. In the right plot, g is presented for the inclusion process and for a ZRP with $\chi = \rho(1+\rho)$. It is confirmed that both processes belong to the Arrhenius universality class, with $g = 1$. For both plots, the numerical values show good agreement with the theoretical prediction and are within the expected errors of the numerical method. We stress that the numerical code, like the analytical treatment, relies on the validity of the MFT and of the additivity principle assumption.

$$\begin{aligned} \frac{\Phi_{\rm SIP}}{D_0 L} &= \min_F \int dx\, J_F^2 + \Lambda(\sinh^2 F - \overline{\rho}_0), \\ F|_{x=1} &= \partial_x F + \frac{1}{4D_0} \sinh 2F \partial_x U|_{x=0} = 0, \\ J_F &= \partial_x F + \frac{1}{4D_0} \sinh 2F \partial_x U. \end{aligned} \tag{3.16}$$

Setting $J_{F_{\rm eq}} = 0$, we find $F_{\rm eq} = \mathrm{arctanh} A \mathrm{e}^{-\mathrm{U}/2\mathrm{D}_0}$. This implies, together with (3.2) that

$$\begin{aligned} \omega &= \mathrm{arctanh}\, A \mathrm{e}^{-\Delta \mathrm{U}/2\mathrm{D}_0}, \\ 1 + \overline{\rho}_0 &= \int dx \frac{1}{1 - A^2 \mathrm{e}^{-\mathrm{U(x)}/\mathrm{D}_0}}, \end{aligned} \tag{3.17}$$

where we have recovered A from the mass conservation. Eq. (3.17) suggests that for any finite density $\overline{\rho}_0$, one should have $0 < A^2 < 1$ whenever $\Delta U/D_0 \gg 1$. Evaluating the latter integral can be done exactly only for a set of potentials. Nevertheless, for $\overline{\rho}_0 \to 0$ we have $A^2 \to 0$ and similarly as $\overline{\rho}_0 \to \infty$ we have $A^2 \to 1^-$. Moreover, A^2 is an increasing (and bounded) function of $\overline{\rho}_0$. Therefore, we find $\omega^2 = \mathrm{arctanh}^2(A \mathrm{e}^{-\Delta \mathrm{U}/2\mathrm{D}_0}) \approx \mathrm{A}^2 \mathrm{e}^{-\Delta \mathrm{U}/\mathrm{D}_0}$. This implies

$$\Phi_{\rm SIP} = D_0 L \mathrm{Poly}(\Delta \mathrm{U}/\mathrm{D}_0) \mathrm{e}^{-\Delta \mathrm{U}/\mathrm{D}_0}, \tag{3.18}$$

following (2.1), and as proposed in [72]. The SIP, lacking excluded volume effects, is indeed within the Arrhenius universality class.

Let us conclude the analysis with the zero-range processes, allowing to account for non-trivial interactions, repulsive and attractive, but with no excluded volume effects.

3.1.6 The zero-range process (ZRP)

In this subsection, we turn to study the set of zero-range processes (ZRP). Unlike the previous models, where the interaction was restricted to either repulsive or attractive, the set of ZRP allows to have repulsive, attractive or a mixture of repulsive and attractive interactions. Like the SIP, the site occupation is unbounded. Therefore, there are no excluded volume effects, and (2.1) implies $g = 1$. Here, we show this is indeed the case, showing that the type of interaction plays no role in the determination of g, where no excluded volume effects are present in lattice gas models.

Within the MFT, the ZRP is captured by $D = \partial_\rho \chi$. Generally for the ZRP, the F transformation implies $\chi = F^2$. Hence, we have

$$\begin{aligned} \frac{\Phi_{\mathrm{ZRP}}}{D_0 L} &= \min_F \int dx\, J_F^2 + \Lambda(\mathrm{inv}[\chi] - \overline{\rho}_0), \\ F|_{x=1} &= \partial_x F + \frac{1}{2D_0}\chi^{1/2}\partial_x U|_{x=0} = 0, \\ J_F &= \partial_x F + \frac{1}{2D_0}\chi^{1/2}\partial_x U. \end{aligned} \tag{3.19}$$

Here we have denoted $\mathrm{inv}[\chi]$ as the inverse function to χ. Requiring $J_{F_{\mathrm{eq}}} = 0$ implies $F_{eq} = A\mathrm{e}^{-\mathrm{U}/2\mathrm{D}_0}$, where the constant A is found from the mass conservation

$$\overline{\rho}_0 = \int dx\, \mathrm{inv}[\chi](\mathrm{F}_{\mathrm{eq}}^2). \tag{3.20}$$

From (3.2), we find $\omega = A\mathrm{e}^{-\Delta\mathrm{U}/\mathrm{D}_0}$. We stress that the perturbative approach works as long as $\omega \ll 1$. Hence, we will need to infer the value of A, which of course depends on the mobility χ.

Since χ is a monotonous increasing function of ρ, $\mathrm{inv}[\chi]$ is also a monotonous increasing function of F. Hence, together with $\mathrm{inv}[\chi](0) = 0$, we can use the mass

conservation equation to express A

$$\overline{\rho}_0 = \int dx \, \mathrm{inv}[\chi](\mathrm{A}^2 \mathrm{e}^{-\mathrm{U}/\mathrm{D}_0}) \approx \mathrm{c}\frac{\mathrm{D}_0}{\Delta \mathrm{U}} \mathrm{inv}\left[\chi\right]\left(\mathrm{A}^2\right), \tag{3.21}$$

where $c > 0$ is a constant depending on the exact shape of χ. Taking this into account we demand

$$\omega^2 = \chi\left(\frac{1}{cD_0}\Delta U \overline{\rho}_0\right) \mathrm{e}^{-\Delta \mathrm{U}/\mathrm{D}_0} \ll 1, \tag{3.22}$$

for the validity of the perturbation approach. Eq. (3.22) is satisfied for a polynomial χ and we find as expected

$$\Phi_{\mathrm{ZRP}} \asymp \mathrm{e}^{-\Delta \mathrm{U}/\mathrm{D}_0}. \tag{3.23}$$

In the rather extreme case, where χ is an exponentially increasing function, there exists some density where ω is not longer small. In this case, the perturbative approach breaks down. Physically, an exponentially increasing mobility and diffusivity imply that particles do not tend to bunch up, and that the particle jump rate is increasing with the local occupancy. In this case, particles leave the trap fast. It is beyond the scope of the present work to asses what is the escape rate in such a scenario. Nevertheless, notice that this is the exact opposite case to one leading to a condensation transition [106], where the particle rates become slow when the onsite density is large.

3.2 Discussion

In this work, we have delved deeper into the Arrhenius Law for interacting particle systems. To this end, we have computed the survival probability of interacting diffusive particles in a deep potential trap. Typically, the survival time is significantly longer than the diffusive time L^2/D_0 when the trap is deep, i.e. $\Delta U/D_0 \gg 1$. In

this case, the survival probability takes the large deviation form $\mathcal{S}(t) \asymp \mathrm{e}^{-\mathrm{t}\Phi}$, where Φ is the large deviation function. To asses Φ – the escape rate from the trap – we have employed the MFT, a nonequilibrium hydrodynamic theory for diffusive systems. Analytically, we have established, for a list of paradigmatic processes, that the escape rate falls into one of the two universality classes. If particle occupancy is unbounded, the process belongs to the Arrhenius universality class, where $\Phi \asymp \mathrm{e}^{-\Delta \mathrm{U}/\mathrm{D}_0}$. This is demonstrated for the non-interacting case, the SIP and a large class of zero-range processes. If particle occupancy is bounded, i.e. particles generate excluded volume, the process belongs to the excluded volume universality and $\Phi \asymp \mathrm{e}^{-\Delta \mathrm{Ug}/\mathrm{D}_0}$, where $g = 1 - U(\overline{\rho}_0)/\Delta U$ for monotonous potentials. Importantly, g is independent of the dynamics of process. This was demonstrated for the SSEP and the strong particles model which share the same g despite having completely different dynamics, see Fig. 3.1. We refer to Table 3.1 for a concise summary of the generalized AL.

An intuitive way to interpret g in the escape rate is through the minimum energy configuration [72]. At low temperatures, i.e. $D_0 \ll \Delta U$, an equilibrium system is dominated by its minimum energy configuration. Hence, the activation energy $\Delta U g$ is the necessary energy to activate a single particle. For deep potentials, the minimum energy configuration packs the particles as tightly as possible around the global minimum. Particles that can be packed into a single point at finite energy will be found in the Arrhenius law. Particles with exclusion dynamics change their minimum energy configuration as a function of their density in the trap. For a monotonous trap, we expect to find the highest energy particle at $x = \overline{\rho}_0$. Hence, the activation energy is $\Delta U g = \Delta U - U(\overline{\rho}_0)$. Indeed this intuitive argument, suggested in [107] for systems with linear dynamics, allows to infer the rigorous results obtained in this work.

The approach developed here significantly reduces the complexity of calculating the

escape rate Φ. Previously in [72], Φ was obtained by direct solution of the non-linear Euler-Lagrange equation (2.8). Analytically, solving (2.8) is feasible for a limited set of potentials. Numerically, solving (2.8) via a shooting method is restricted to $\Delta U/D_0$ no larger than ~ 40. Using the perturbative approach developed here, we notice that at the expanse of ignoring the sub-exponential terms of the escape rate, the perturbative approach allows to gain analytical insight for any potential. Numerically, one can employ the perturbative approach which basically boils down to extracting A from the mass term, see e.g. (3.10). For the SSEP, one can easily go to $\Delta U/D_0 \sim 100$ by numerical integration of (3.10). The numerical advantage of the perturbative approach will be crucial when studying non-monotonous potentials (see Chapter 4).

One can try to interpret our results within the experimental context in the following way. We consider once more the colloidal particles, restricted to travel through a tube or a channel. Moreover, they are subjected to a trap potential, which can be facilitated by optical tweezers, fixed in time. Assume the density of the colloids in the trap to be finite. In the case of a narrow tube, where the radius of the tube is comparable to that of the colloids, the escape rate is determined by the excluded volume. Naturally, such scenarios belong to the excluded volume universality class. Importantly, the interactions between the colloids hardly effect the escape rate. Conversely to the Arrhenius universality, the shape of the potential and the colloid density in the trap play a key role in determining g.

The perturbative method is able to corroborate for a number of important models the existence of the two universality classes; the Arrhenius universality class for lattice gas models with unbounded particle occupancy, and the excluded volume universality class for lattice gas models with bounded particle occupancy. One case where the perturbative approach is inconclusive, is for a ZRP where χ is exponentially increasing for large densities. This process, microscopically, corresponds to a

Table 3.1: Summary of the Generalized AL

Models	$\boldsymbol{D}\&\boldsymbol{\chi}$	$\boldsymbol{F_{eq}}$	$\boldsymbol{\omega}$	**AL,** $\boldsymbol{\Phi \asymp e^{-\frac{\Delta U}{D_0} g(\bar{\rho}_0)}}$	
Non-interacting particles	$D=1$ $\chi=\rho$	$Ae^{-\frac{U(x)}{2D_0}}$ (3.5)	$Ae^{-\frac{\Delta U}{2D_0}}$ (3.6)	$g=1$	**Arrhenius universality**
SIP	$D=1$ $\chi=\rho(1+\rho)$	$\operatorname{arctanh}(Ae^{-\frac{U(x)}{2D_0}})$	$\operatorname{arctanh}(Ae^{-\frac{\Delta U}{2D_0}})$ (3.17)	$g=1$	
ZRP	$D=\partial_\rho \chi$	$Ae^{-\frac{U(x)}{2D_0}}$	$Ae^{-\frac{\Delta U}{2D_0}}$	$g=1$	
SSEP	$D=1$ $\chi=\rho(1-\rho)$	$\arctan(Ae^{-\frac{U(x)}{2D_0}})$ (3.9)	$\arctan(Ae^{-\frac{\Delta U}{2D_0}})$ (3.12)	$g=1-\frac{U(\bar{\rho}_0)}{\Delta U}$	**Excluded volume universality**
Strong particles model	$D=\frac{1}{1-\rho}$ $\chi=\rho$	$\operatorname{arcsinh}(Ae^{-\frac{U(x)}{2D_0}})$	$\operatorname{arcsinh}(Ae^{-\frac{\Delta U}{2D_0}})$	$g=1-\frac{U(\bar{\rho}_0)}{\Delta U}$	

model where particle bunching leads to strong repulsion. While the perturbative approach fails to capture the escape rate Φ, it should still be possible to employ the shooting-method algorithm in [72] to understand whether the universality is maintained. Moreover, it could also be possible to invoke microscopic techniques in order to capture the escape rate Φ [48].

Another point worth discussing is the importance of the F transformation in the analytical analysis. First, there exist non-particle transport models, like the Kipnis-Marchioro-Presutti (KMP) model [108], where a continuous quantity like energy is being transported. For the KMP model, with $D=1, \chi=\rho^2$, the F transformation diverges. Simply put, this implies, that the large deviation form of the survival probability can no longer be assumed. We do not expect such escape problem could be successfully analyzed using the MFT. Second, the macroscopic presentation using D, χ of many particle models is either unknown, or given by convoluted expressions

[109]. This implies that only numerical approximations to the F transformation are possible. It would be useful to develop such a protocol to advance the perturbative approach analysis to deal with arbitrary diffusive dynamics.

To conclude, the successful identification of the two universality classes motivates further studies, beyond the diffusive regime. Can a similar classification in active systems, multi-particle species, particles with inertia be observed? Is it possible to identify other universality classes when we leave the realm of lattice gas models, e.g. in soft particles? These questions show that indeed the study of the escape problem from a deep trap is far from resolved.

Chapter 4

Inferring intermediate states by leveraging the many-body Arrhenius law

The content of this chapter has been published in [110]

In Chapters 2 and 3, we developed a generalized Arrhenius law for interacting diffusive systems with and without excluded volume interactions. In particular, for systems with excluded volume interactions, we demonstrated that the function $g(\overline{\rho}_0)$, which appears in the escape rate $\Phi_{\mathrm{MP}} \asymp e^{-\beta \Delta U g(\overline{\rho}_0)}$, depends explicitly on the form of the confining potential $U(x)$. In the present chapter, we show that this dependence can be systematically exploited to infer the number of metastable states in an unknown energy landscape.

4.1 Introduction

Determining the escape-time statistics of a system evolving in a potential landscape is of fundamental importance. Of particular interest is the associated inverse problem, namely the inference of properties of the underlying energy landscape from observed escape-time statistics. One aspect of the inverse problem, prevalent in the theory of chemical dynamics, is predicting the value of the energy barrier ΔU by interpreting experimental data. Such an activation process may extend beyond the

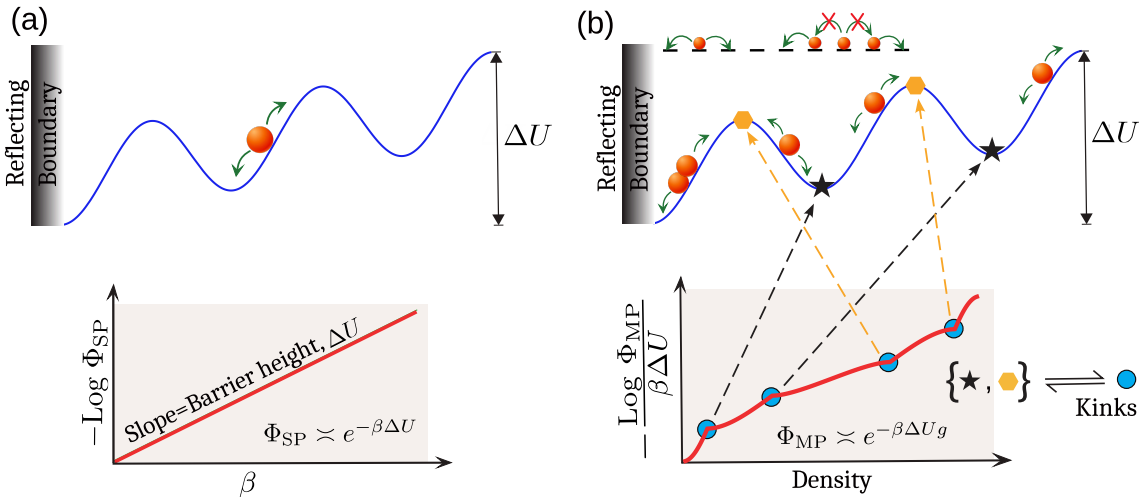

Figure 4.1: (a) The escape problem of a single particle. The bottom figure shows the traditional inference of the activation barrier height from Arrhenius law Eq. (1.5) (b) Inference of the potential minima and maxima by employing the many-body Arrhenius law Eq. (1.6). The number of kinks in the bottom figure corresponds to local maxima and minima of the potential $U(x)$ in the top figure. Thus, the many-body escape dynamics (for instance, activated dynamics of a stochastic lattice gas model with volume exclusion as shown in the top) allow to infer the metastabilities of the single particle escape problem.

standard Kramers setup, and involve a conformational or configurational transition as motion along the reaction coordinate in a rugged energy landscape [23]. A second aspect of the inverse problem is inferring the coordinates and number of local minima in the energy landscape. The local minima can be identified as long-lived states, or metastabilities, where the system spends significant time. Identifying these metastabilities enables the reduction of the system's state space by filtering out fast degrees of freedom, a crucial technique for simplifying complex dynamics in chemical physics. While the AL Eq. (1.5) is equipped to address finding ΔU as the slope of the semilog plot of Φ_{SP} (see Fig. 4.1(a)), building on the subexponential dependence on τ_0, it is ill equipped to infer the number and positions of the metastabilities.

The problem of quantifying the state space of long-lived states was addressed in the literature, especially by employing statistical tools to assess the state space number, i.e. the number of local minima of the trapping potential or metastabilities. For instance, one key result in chemical kinetics is that the randomness parameter or the

coefficient of variation measured from the turnover time of an enzymatic reaction, can place a strict lower limit on the topology i.e., the number of metastable kinetic states in any viable model for the mechanism of a given enzyme [22]. Another method based on escape time was proposed by Li and Kolomeisky [111] to determine the mechanism and topology of complex chemical and biological networks. There, the authors hypothesized that the dwell-time distributions of events between two states can encode information on number of intermediate states, pathways, and transitions that lie between initial and final states. Recently, this theoretical work was tested in a high precision experiment [33] for an overarching set of complex molecular or nanoscale systems to unravel the quantitative features of the underlying energy landscape. In another work, the structure of the protein folding energy landscape involving multiple kinetic traps was predicted via the multiple relaxation time scales emanating from the first passage time distribution between reactants and products of these biomolecules [112]. In a similar vein, here we show that the generalized Arhhenius law, Eq. (1.6), enables the inference of the number of metastabilities in a potential landscape— thereby establishing a powerful and robust theoretical method irrespective of the complex underlying mechanisms, and which could not be achieved within the traditional Arrhenius law, Eq. (1.5).

We recall that the diffusive particles with excluded volume interactions, positioned in a deep trap, acquire the escape rate given by the many-body Arrhenius law in Eq. (1.6) [72,105](see chapters 1, 2 and 3). $\Delta U g(\overline{\rho}_0)$ in Eq. (1.6) is termed as the effective activation energy. The function $g(\overline{\rho}_0)$ represents the many-body correction to the conventional Arrhenius law. Notably, while $g(\overline{\rho}_0)$ depends on the particle density $\overline{\rho}_0$ and on the specific form of the trapping potential, it remains independent of the microscopic details of the particle interactions. The only requirement is that the interactions include, but are not restricted to hardcore repulsion – there exist an excluded volume (see Chapter 3 for specific examples). Moreover, the function $g(\overline{\rho}_0)$ is computable for an arbitrary trapping potential, using a geometric argument. In

this work, we show that for a given potential, varying $\overline{\rho}_0$ – the particle density in the trap may lead to kinks in $g(\overline{\rho}_0)$. These kinks are associated with the local minima and maxima of the trap potential (see FIG. 4.1). We reveal a surprising equivalence between $\Phi_{\rm MP}$ and a thermodynamic partition function. Drawing on the theory of critical phenomena, we construct analogous thermodynamic response functions as quantitative tools to detect metastabilities, treating them as the counterparts of thermodynamic phase transitions.

4.2 Setup

We recall that in the limit of deep traps, i.e., $\beta\Delta U \gg 1$ and large M, L, with a fixed particle density in the trap $\overline{\rho}_0 = M/L$, the escape rate for interacting diffusive systems is given by Eq. (1.6) (See Chapters 2 and 3 for details). For diffusive systems with excluded volume interactions, the function g in Eq. (1.6) is explicitly given by $g(\overline{\rho}_0) = 1 - U_{\rm top}(\overline{\rho}_0)/\Delta U$, with $U_{\rm top}$ defining the maximum potential value occupied by particles when they are arranged in the minimum energy configuration (MEC) (see FIG. 4.2). This implies

$$\overline{\rho}_0 = \int dx\, \Theta(\beta U_{\rm top} - \beta U(x)), \tag{4.1}$$

where Θ is the Heaviside function.

Eq. (1.6) is non-trivial to derive in the many-body case, yet, it can be understood by an intuitive argument. In the limit $\beta\Delta U \to \infty$, the particles organize into the MEC, which is primarily determined by the structure of the potential (see FIG. 4.2). The escaping particle is the one with the highest potential energy, $U_{\rm top}$ in the MEC (also see Langer et al. [107]). This intuition essentially leads to Eq. (1.6), recalling that $g(\overline{\rho}_0) = 1 - U_{\rm top}(\overline{\rho}_0)/\Delta U$. Note that activating a single particle from the MEC leads to an energy dominated free energy change in the macroscopic system. The latter

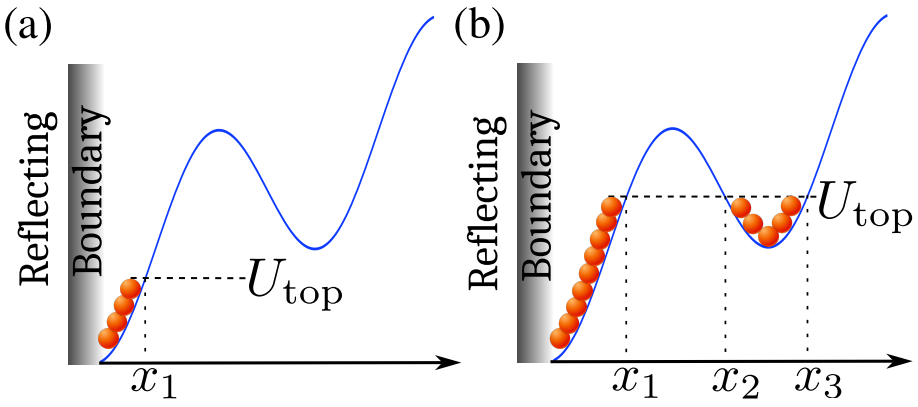

Figure 4.2: A visualization of the MEC for particles with excluded volume on an arbitrary non-monotonic potential. Particles occupy the potential for $U(x) < U_{\rm top}$. (a) Here $U_{\rm top}$ is smaller then the lowest value of the potential extrema. Thus, $U_{\rm top}$ has a single intersection with $U(x)$, at position x_1, and we find $\overline{\rho}_0(U_{\rm top} = U(x_1))$, leading to $U_{\rm top}(\overline{\rho}_0) = U(x = \overline{\rho}_0)$ as in the monotonous potential. (b) Here $U_{\rm top}$ is in the range where there are three intersection points with $U(x)$, denoted by $x_{1,2,3}$. In this case $\overline{\rho}_0(U_{\rm top}) = x_1 + x_3 - x_2$. Notice that in this case $U_{\rm top}(\overline{\rho}_0) \neq U(x = \overline{\rho}_0)$.

assertion may differ for particles with long-range interactions like polymers [113], which we do not consider within our formalism.

For the sake of concreteness, we stress that our analysis relies on two assumptions. First, that the typical time scale for activation is much larger than the diffusive time scales. Second, that the activation time from the initial condition is much longer than the relaxation time to the MEC. Physically, this means that there is no set of particles that start too close to the absorbing boundary, or a macroscopic set of particles that starts in a local potential minimum, away from the origin, and detached from the main bulk of particles.

Within our trap setup, and for monotonous potentials, the MEC predicts via Eq. (4.1) that $U_{\rm top} = U(x = \overline{\rho}_0)$, leading to

$$g_{\rm monotone}(\overline{\rho}_0) = 1 - U(x = \overline{\rho}_0)/\Delta U. \tag{4.2}$$

See also FIG. 4.2. Intuitively, the escape rate should increase as we fill the trap with excluded volume particles, since adding particles pushes the highest energy particle

in the trap closer to the activation energy. Hence, $g(\overline{\rho}_0)$ has to be a monotonous decreasing function of $\overline{\rho}_0$. From this reasoning alone, it is clear that $g(\overline{\rho}_0)$ cannot follow Eq. (4.2) for non-monotonous potentials. The presence of non-monotonic potentials is quite ubiquitous in the context of particle, ion or metabolite transport through confined geometries containing narrow openings, corners, bottlenecks or channels. Despite their pervasiveness, the inverse problem of inferring the structure of the channel, the nature of the potential from the escape time statistics remains a challenge [112]. In what follows we analyze the structure of $g(\overline{\rho}_0)$ for an arbitrary non-monotonic potential, and show the relevance to the inference problem.

4.3 Emergence of the kinks

In non-monotonic potentials, the escape rate, and in particular $g(\overline{\rho}_0)$ varies dramatically from the monotonic case captured in Eq. (4.2). Indeed, one still infers $g(\overline{\rho}_0)$ from the MEC. Before providing $g(\overline{\rho}_0)$ for an arbitrary trapping potential, it is instructive to first consider a minimal model for a non-monotonic potential – the piecewise linear potential (see FIG. 4.3). Recall that $g(\overline{\rho}_0) = 1 - U_{\rm top}(\overline{\rho}_0)/\Delta U$ for any arbitrary potential. However, crucially $U_{\rm top} \neq U(x = \overline{\rho}_0)$ for the non-monotonous potentials. Now, one may proceed by determining $U_{\rm top}(\overline{\rho}_0)$, or alternatively the inverted function $\overline{\rho}_0(U_{\rm top})$ from Eq. (4.1), the latter leads to

$$\overline{\rho}_0(U_{\rm top}) = \begin{cases} \frac{U_{\rm top}}{2\Delta U} & \text{for } 0 < \frac{U_{\rm top}}{\Delta U} < \frac{1}{3} \\ 2\frac{U_{\rm top}}{\Delta U} - \frac{1}{2}, & \text{for } \frac{1}{3} < \frac{U_{\rm top}}{\Delta U} < \frac{2}{3} \\ \frac{\frac{U_{\rm top}}{\Delta U}+1}{2}, & \text{for } \frac{2}{3} < \frac{U_{\rm top}}{\Delta U} < 1. \end{cases} \tag{4.3}$$

It should then be understood that the kinks in $\overline{\rho}_0(U_{\rm top})$ correspond to the local minimum and maximum of $U_{\rm pwl}$. These kinks would be inherited by $g(\overline{\rho}_0)$. Recalling

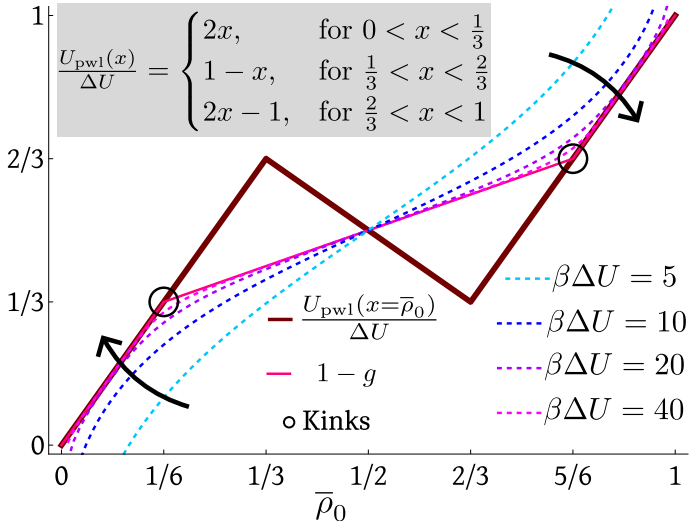

Figure 4.3: (Top) The piecewise linear potential $U_{\rm pwl}(x)$ is plotted (solid thick brown) together with the MEC prediction for $1-g$ (solid magenta). The black circles highlight the positions of the kinks in g. The dashed lines reveal the convergence of the finite $\beta\Delta U$ approximation scheme to the MEC $1-g$ curve. Noticeably, the convergence, marked by the black arrows, is faster away from the kinks.

$g(\overline{\rho}_0) = 1 - U_{\rm top}/\Delta U$, one can invert Eq. (4.3), to find (see FIG. 4.3)

$$1 - g(\overline{\rho}_0) = \begin{cases} 2\overline{\rho}_0 & \text{for } 0 < \overline{\rho}_0 < \frac{1}{6} \\ \frac{1}{2}\overline{\rho}_0 + \frac{1}{4} & \text{for } \frac{1}{6} < \overline{\rho}_0 < \frac{5}{6} \\ 2\overline{\rho}_0 - 1 & \text{for } \frac{5}{6} < \overline{\rho}_0 < 1 \end{cases} \tag{4.4}$$

The treatment above for $U_{\rm pwl}$ can be generalized to an arbitrary potential trap. It is the local minima and maxima of the potential trap that introduce kinks in $g(\overline{\rho}_0)$. Let n be the number of intersections of $U_{\rm top}$ with an arbitrary trapping potential $U(x)$. Unless $U_{\rm top}$ exactly intersects with a local maximum or minimum point, $n = 2m+1$ is an odd number larger or equal to one. The MEC implies that

$$\overline{\rho}_0(U_{\rm top}) = \sum_{i=0}^{m} (x_{2i+1} - x_{2i}) \,, \tag{4.5}$$

where $x_0 = 0$ and x_i is the i-th intersection of $U(x)$ with $U_{\rm top}$ (FIG. 4.2 (b) demonstrates the idea). The origin of the kinks observed in $g(\overline{\rho}_0)$ can be understood as

follows. See Fig.4.1(b). For small values of $\overline{\rho}_0$, the particles arrange themselves around the reflecting boundary in the MEC. As $\overline{\rho}_0$ increases further beyond a certain value, the MEC paradigm suggests that the particles begin to populate not only the region near the reflecting boundary but also the vicinity of the first potential minimum (which lies at a lower energy level than the second minimum; see FIG. 4.1(b)). This shift in spatial distribution of particles marks the emergence of the first kink in $g(\overline{\rho}_0)$ shown in FIG. 4.1. With subsequent increases in density, similar organizational shifts occur, leading to additional kinks in $g(\overline{\rho}_0)$. The number of kinks equals the number of local minima and maxima of the potential U as shown in FIG. 4.1(b). It should be noted that it is hard in general to provide an analytic expression of $g(\overline{\rho}_0)$ as it involves finding analytically the intersections of the arbitrary trap potential $U(x) = U_{\text{top}}$ for any $0 < U_{\text{top}} < 1$, and then invert Eq. (4.5). Nevertheless, a numerical inference of $g(\overline{\rho}_0)$ is straight-forward for any arbitrary trap potential and at any desired level of precision. Thus, we are able to represent $g(\overline{\rho}_0)$ for both monotonous and non-monotonous trap potentials using the MEC.

4.4 The kinks and thermodynamic phase transitions

Importantly, the MEC and the resulting kinks are obtained as asymptotic results in the $\beta\Delta U \to \infty$ limit. The kinks constitute dynamical phase transitions as the mean density is varied. However, the escape rate Φ_{MP}, or $g(\overline{\rho}_0)$, is expected to be analytic at finite $\beta\Delta U$. To build this intuition, let us draw a correspondence between the kinks in the escape problem and the critical phenomena in thermodynamics. A thermodynamic phase transition points to a non-analyticity in the thermodynamic potential, say the Helmholtz Free energy, when the temperature is varied beyond

a critical temperature. The non-analytic point is apparent only in the thermodynamic limit of an infinite system. Translating to the MEC, the *large system size* in thermodynamics corresponds to the $\beta\Delta U \to \infty$ limit and the *temperature* corresponds to the mean density $\overline{\rho}_0$, which can be externally controlled. Bridging this correspondence, we can define

$$\mathcal{F} = -\frac{1}{\beta\Delta U}\log\Phi_{\mathrm{MP}}, \quad \mathcal{R}_n = \frac{\partial^n \mathcal{F}}{\partial \overline{\rho}_0{}^n} \tag{4.6}$$

to correspond to the free energy per volume, where $\beta\Delta U$ serves as the volume parameter and $\mathcal{R}_n$ are the associated response functions. It is important to note that in the limit $\beta\Delta U \to \infty$, the free energy density $\mathcal{F}$ corresponds to $g(\overline{\rho}_0)$, and that the singular behavior arises from Φ_{MP} which corresponds to a partition function in statistical mechanics.

Crucially, the non-analytic nature of the escape rate becomes apparent only in the *thermodynamic limit*, i.e. at $\beta\Delta U \to \infty$. At finite $\beta\Delta U$, it is especially hard to observe the emerging kinks, as $\beta\Delta U$ is rather limited experimentally to order of 20, contrary to the macroscopic volume in thermodynamic systems (see Appendix D.2, FIG. D.2 and FIG. D.3). A standard method to observe phase transition is by measuring the scaling of response functions such as susceptibilities and other derivatives of the thermodynamic potentials. This essentially corresponds to looking at the derivatives of $\mathcal{F}$ and the scaling of the divergences close to the critical densities, i.e. where we expect the kinks. That is, instead of the MEC, it is required to determine Φ_{MP} for a finite $\beta\Delta U$. This has been achieved [105] in Chapter 3, by developing a perturbative approach, estimating g analytically at a finite (but large) $\beta\Delta U$ [1]. From the knowledge of Φ_{MP} at finite $\beta\Delta U$, the corresponding finite-$\beta\Delta U$ response functions can be obtained using Eq. (4.6). These response functions capture the signatures of kinks in g, thereby revealing the number of metastable states in the

[1] In [72] Chapter 2, an exact approach was developed. However, the treatment is much harder analytically, and numerically the estimation is limited to about $\beta\Delta U = 20$.

potential landscape.

Statistical physics states that finite systems can only lead to analytic thermodynamic observables. Therefore, phase transitions occur only in the thermodynamic limit of infinite system size. However, for a macroscopic particle number of the order of Avogadro's number, it is hard to tell the difference between a true divergence of, e.g. the response functions, and a large but finite increase close to the critical point. Here, $\beta\Delta U$ serves as the equivalent of the system size, whereas the density serves as the control parameter to manipulate toward the critical points. This implies that observing the kinks experimentally is unattainable. It is more practical to focus on the scaling properties of the diverging response functions. To see that, we recall that

$$\begin{aligned} \mathcal{F} &= g(\overline{\rho}_0) + \mathcal{F}_{\mathrm{s}} + \text{non-singular subleading terms}, \\ \mathcal{F}_{\mathrm{s}} &= \Delta U^{-\alpha} f_{\mathrm{s}} \left(\beta \Delta U \delta\rho^{\gamma}\right). \end{aligned} \tag{4.7}$$

The regular part is dominated by $g(\overline{\rho}_0)$ at large $\beta\Delta U$, and the singular part is given by a singular scaling function f_{s}. Here $\delta\rho$ is the distance from the critical density, and $\alpha, \gamma > 0$ are critical exponents. We note, however, that the inference of kinks in $g(\overline{\rho}_0)$ doesn't require the exact determination of these critical exponents.

4.5 Response functions for an interacting lattice gas model

To demonstrate the emergence of the kinks through the response functions, we focus on the symmetric simple exclusion process (SSEP). We start with the general expression for the escape rate namely $\Phi_{\mathrm{MP}} \asymp A^2 \mathrm{e}^{-\beta\Delta \mathrm{U}}$, as derived in Chapter 3. Here, one can infer A from the value of the equilibrium density profile at the absorbing

boundary using Eq. (3.10)

For the SSEP particles in a piecewise linear potential U_{pwl}, Eq. (3.10) can be solved to get an expression for A in the "finite size" limit, revealing the precursor to the criticality in the escape rate in the "finite size" limit (see Appendix D.1). This determines Φ_{MP} at finite $\beta\Delta U$. Subsequently, the corresponding free energy density $\mathcal{F}$ is computed from Φ_{MP} using Eq. (4.6) and is shown in FIG. 4.3 as dashed curves for various $\beta\Delta U$ values. We next examine in greater detail the regime $0 < \overline{\rho}_0 < 1/6$ where the finite size expression of A (and, therefore the escape rate) can be made simpler (see Appendix D.1). However, the analysis could be extended to the full range of $\overline{\rho}_0$, doing so in the main text would introduce technical complexity, going against our pedagogical purposes. Thus, we provide a full numerical analysis of the piecewise linear potential in Appendix D.1.

We can now write the corresponding free-energy in the finite size limit following (4.6)

$$\begin{aligned} \mathcal{F} &= \mathcal{F}_0 + \mathcal{F}_{\text{s}}, \\ \mathcal{F}_{\text{s}} &= -\frac{1}{\beta\Delta U} \log \frac{-1+\sqrt{1+12\mathrm{e}^{-2\delta\rho\beta\Delta \mathrm{U}}}}{6}, \end{aligned} \tag{4.8}$$

where $\delta\rho = 1/6 - \overline{\rho}_0$ measuring the distance from the critical density $\overline{\rho}_0 = 1/6$. Here $\mathcal{F}_0 = 2/3$ is a regular contribution that will not lead to the divergence of the response functions. We note that there are subleading terms in $\mathcal{F}_0$, that are discarded in our perturbative approach. $\mathcal{F}_{\text{s}}$ is the singular part of the associated free energy. The singularity appears at $\delta\rho\beta\Delta U \to \infty$ which corresponds to a finite $\delta\rho$ (distance from the critical density) and infinite $\beta\Delta U$. It is then clear that observing the singularity directly from $\mathcal{F}$ is impractical. In other words, the formation of the kinks will become apparent only at exceptionally large values of $\beta\Delta U \approx 100$. Therefore, to observe the precursors of the kinks, we turn to the response functions. The response functions accentuate the singular part of $\mathcal{F}$, i.e. $\mathcal{R}_n \propto (\beta\Delta U)^{n-1}$ when keeping

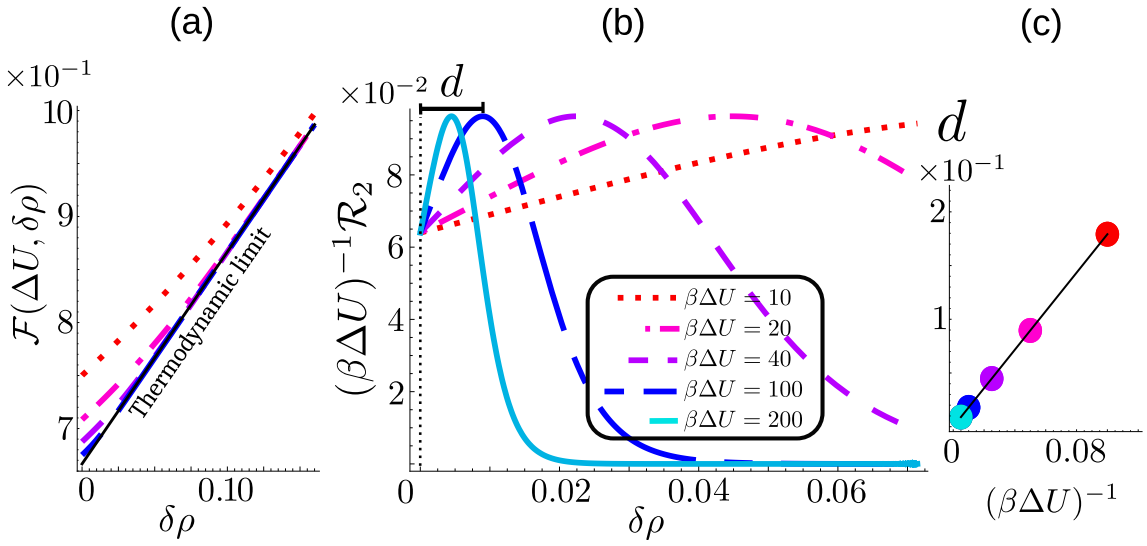

Figure 4.4: (a) The "free energy" $\mathcal{F}$ is calculated for finite $\beta\Delta U$ values, and compared with the MEC result ($\beta\Delta U = \infty$) for SSEP particles subjected to the U_{pwl} trapping potential. It is evident that the convergence is better away from the critical point at $\delta\rho = 0$. However, to infer the criticality, we need to consider the response function $\mathcal{R}_2$. (b) Rescaled response function $\mathcal{R}_2/(\beta\Delta U)$ for different $\beta\Delta U$ as found from Eq. (4.8). The precursor of the kink manifest as a scalable peak, at distance $1/\beta\Delta U$ from the expected kink. (c) Distance d of the peaks from the expected critical point is shown to scale like $1/\beta\Delta U$. We remind that in finite systems, the singularities characteristic of critical phenomena are rounded and shifted: response functions exhibit smooth peaks rather than divergences. As the system size increases, these peaks grow sharper and their location approaches the true critical point in the thermodynamic limit. Here, we observe the same for d as $\beta\Delta U$ replaces the system size [1].

$\beta\Delta U\delta\rho$ finite. FIG. 4.4 demonstrates our findings. We first show that while $\mathcal{F}$ converges to its MEC value as we increase $\beta\Delta U$, the convergence is slower close to the critical point, i.e. for $\delta\rho \to 0$. Moreover, we demonstrate the scaling behavior of the response function $\mathcal{R}_2$.

Finding an analytical expression for $\mathcal{F}$ for arbitrary potential landscape turns out to be completely intractable, even for the SSEP within the perturbative approach. Nevertheless, inference of the kinks through the response functions is not limited to an analytic treatment alone, but can be probed using numerical techniques using the response functions. This is demonstrated in Appendix D.2 for nonlinear trap potentials with multiple metastabilities – the appearance of similar potential energy

barriers in the activation gating of the bacterial ion channels is quite ubiquitous [114]. It is demonstrated in Appendix (see FIG. D.2 and FIG. D.3) how $\mathcal{F}$ systematically converges to the MEC limit in the large $\beta\Delta U$ limit while the response functions clearly indicate the emergence of the kinks. In a nutshell, the local minima and maxima of the potential can be inferred from the response functions, obtained from escape time measurements, without prior knowledge of the trap potential.

4.6 Discussion

In this chapter, we have revisited the survival probability of interacting particles located in a deep trap potential. The particle escape rate follows the generalized Arrhenius form $\Phi_{\rm MP} \asymp {\rm e}^{-\beta\Delta {\rm U} g(\overline{\rho}_0)}$, where $g(\overline{\rho}_0)$ can be asymptotically assessed via the MEC. It was shown that in the excluded volume universality, i.e. for lattice gas models where the lattice site occupancy is capped, $g(\overline{\rho}_0)$ becomes singular in $\beta\Delta U \to \infty$ when the trap potential introduces local minima and maxima. More precisely, local maxima and minima of the trap potential lead to kinks in $g(\overline{\rho}_0)$. Thus, reversing the logic, measurement of kinks in the many-body $g(\overline{\rho}_0)$ allows to infer the number of the single particle long-lived states (metastabilities) induced by the trap potential local minima. The salient point of this work is proposing a statistical test, based on the measureable mean escape time of the many-body problem, that allows to quantify the number of long-lived states in the single-particle activation problem.

By establishing a correspondence between the kinks in $g(\overline{\rho}_0)$ in the escape problem and thermodynamic phase transitions, we introduced the free energy $\mathcal{F}$ and the associated response functions $\mathcal{R}_n$ in Eq. (4.6). The response functions $\mathcal{R}_n$ (for $n \geq 2$) capture the signature of emergence of kinks at finite $\beta\Delta U$ values, which would otherwise manifest only in the asymptotic limit $\beta\Delta U \to \infty$. In the example

considered here, we found that the critical exponents related to the scaling functions (see Eq. (4.7)) are $\alpha = \gamma = 1$. However, we emphasize that determining the exact values of these exponents is not essential (and lies beyond the scope of the present study), identifying the onset of them is sufficient for our problem. Thus, our key objective has been to develop a framework that can identify the criticality, rather than its precise nature. Notably, one might be tempted to claim universality of the critical exponents due to symmetries of the Lagrangian. However, a recent work [115] by one of us suggests that while the critical exponents are indeed universal for smooth potentials, they can be different for non-differentiable piecewise linear potentials. This is indeed what we have observed numerically (see captions of Figs. D.1, D.2 and D.3).

As a proof of concept, it was demonstrated that this approach allows to infer the position of the kinks in an analytically solvable model – the piecewise linear potential. Additionally, we demonstrate in the Appendices that our method allows to infer the number of metastabilities of models that are not susceptible to analytical investigations. It is important to stress that there are obvious limits to the method. For example, if two extremal points in the potential are in close proximity, or if the trap potential introduces a very rugged landscape, the sharpness of the response function scaling test is reduced.

Experimentally, we expect our method to be useful in analyzing transport of interacting particles through a narrow channel, and against a potential gradient. The robust experimental setup by Thorneywork et al. [33] that recently designed colloid transport in the presence of multiple traps by an optical tweezers setup could be a potential avenue to validate our method. Within this setup, collecting measurements on the particle escape rates at different particle densities would allow us to predict the number of local extrema of the potential gradient. We recall that for the initial conditions, one would have to consider the particles to be located well within

the trap, never to be too close to the absorbing boundary. Additionally, our analysis would change dramatically if a macroscopic set of particles would be detached from the MEC, and repositioned around a local minimum of the potential. In an alternative setup, one could also consider tracking the current of a boundary driven setup with an additional bulk drive represented by the trap. Here, initial conditions become immaterial, as the steady state current is associated with the mean escape rate. This setup and its implications will be discussed in a subsequent publication. It is important to emphasize that the response function approach becomes particularly useful when escape times become too large due to large energy barriers, at which the kinks in the data become apparent. Higher-order response functions enhance the peaks – the precursors of the kinks – allowing their identification at lower energy barriers. However, this improvement comes at the cost of increased data acquisition, as higher-order responses require measurements of escape rates over a denser range of densities. Since the determination of escape rates is itself experimentally challenging and prone to under-sampling [116–118], the optimal order of the response function must be chosen with care, depending on the specific experimental conditions.

In this work, we have restricted the trap potential to $1D$. Nevertheless, we point out that the treatment can be extended to higher dimensions, as well as to multi-channel activation problems. It would be interesting to consider also non-diffusive activation processes introducing interacting systems [119, 120], as well as particles with soft interactions, going beyond lattice gas models [121, 122]. Finally, it may be interesting to apply novel approaches to use the finite $\beta\Delta U$ scaling close to the critical points of the escape rate Φ_{MP} in order to obtain better predictions of the behavior away from the criticality [123].

Chapter 5

Speeding up Brownian escape via intermediate finite potential barriers

The contents of this chapter has been published in [124]

As discussed in Chapter 1, the exponential factor in the conventional Arrhenius law, Eq. (1.5), is universal in the sense that it depends solely on the height of the potential barrier. In contrast, the pre-exponential factor is non-universal and depends sensitively on the form of the underlying potential landscape. Consequently, the barrier-crossing time can be modulated through appropriate modifications of the potential profile. This observation provides the motivation for the present chapter, in which we investigate how controlled reshaping of the potential landscape, while preserving the overall barrier height, can be employed to reduce the barrier-crossing time.

Despite extensive research in escape processes over the past several decades, the problem of systematically manipulating the shape of a potential landscape to reduce the mean first-passage time (MFPT) associated with barrier crossing remains relatively less explored. (We recall that, within the first-passage formalism, the mean barrier-crossing time is referred to as the MFPT.) A notable initial contribution in this area is due to Wagner and Kiefhaber [67], who numerically studied the effect of partially folded intermediates along the reaction pathway on the rates

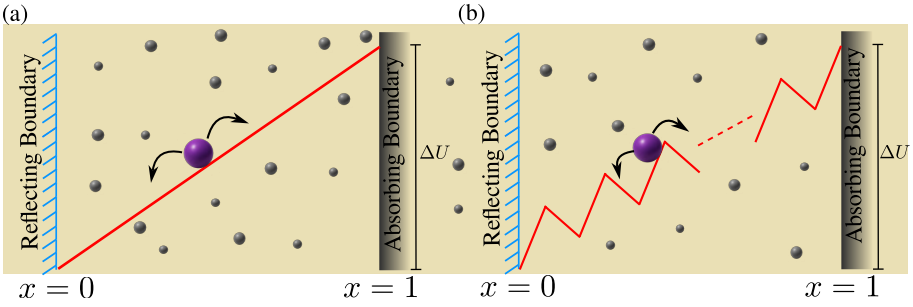

Figure 5.1: Panel (a): Schematic of a Brownian particle (large sphere) that starts at $x = 0$, which is a reflecting boundary, and is eventually absorbed at $x = 1$, which is the absorbing boundary, after overcoming a potential barrier of height ΔU. By altering the potential structure by introducing intermediate potential barriers as in panel (b), we would like to examine whether the mean first-passage time to reach the absorbing boundary can be reduced than that from the unaltered potential configuration as in panel (a). The Brownian particle is assumed to be in contact with a thermal bath surrounded by the bath particles (indicated by the smaller spheres).

of protein folding. By modeling the folding process as the diffusion of reaction coordinates in a potential energy landscape, they showed that placing intermediates within the barrier, without changing its overall height, can enhance folding rates if the intermediate barriers are of moderate heights. Another important contribution in this direction was made by Palyulin and Metzler [68], who demonstrated that replacing a simple linear potential with a piecewise linear potential consisting of two segments (while maintaining a fixed barrier height ΔU) allows for tuning the segment slopes to minimize the MFPT. It was shown that the optimal MFPT achieved in this segmented configuration was lower than that of the original linear potential. Another crucial development along this line was due to Chupeau et al. [34], who experimentally demonstrated that the MFPT of the Brownian particle for reaching a target can be reduced by guiding it through a suitably engineered potential barrier profile. This acceleration of the first-passage process was observed in both the underdamped and overdamped regimes.

This naturally leads to the following compelling questions: Can a faster completion be achieved when a potential is composed of multiple segments instead of just

two? Can the systematic control of the potential shape—achieved through structural modifications of individual segments—indeed expedite the completion process? The purpose of this work is to study a comprehensive model combined with theory and simulations to address such questions. By leveraging the knowledge of such arrangements, it may become possible to design potential landscapes that serve as regulators of transport, where modifications to the potential shape can systematically control the rate at which large molecules, ions, or metabolites escape through confining channels.

To investigate these questions, we consider a prototypical set-up of a Brownian particle diffusing in a landscape depicted in Fig. 5.1(a); the particle starts at position $x = 0$, which acts as a reflecting boundary while the boundary at $x = 1$ is absorbing. Let $\mathcal{T}$ denote the MFPT for the particle to reach $x = 1$ by crossing the potential barrier of height ΔU. Now, consider the alternative setup shown in Fig. 5.1(b), where the potential is replaced with a piecewise structure by introducing multiple intermediate barriers of smaller heights—creating several linear segments—while keeping the overall barrier height ΔU unchanged. We denote the MFPT in this modified potential by $\mathcal{T}^{\text{mod}}$. The central question we explore is whether a suitably chosen piecewise linear potential can yield a lower MFPT, such that $\mathcal{T}^{\text{mod}} < \mathcal{T}$? Using analytical tools from first-passage theory [20], we show that by carefully tuning the slopes of the individual segments in the piecewise linear potential, the MFPT can be significantly reduced. Moreover, we find that increasing the number of intermediate barriers—i.e., the number of adjustable segments—further decreases the MFPT, yielding a powerful control for optimizing escape times. These insights are not limited to linear potentials. We extend our analysis to non-linear landscapes as well, demonstrating that analogous improvements in MFPT can be achieved by replacing smooth non-linear potentials with carefully constructed piecewise non-linear profiles, as illustrated in Fig. 5.4(b). These general findings establish the introduction of intermediate barriers as a general and robust technique for facilitating faster

barrier crossing in diffusive systems.

This chapter is organized in the following way. The system set up is described in section 5.1. This section further discusses the first-passage formalism to compute the MFPT. In section 5.2.1, we review the case of single barrier [68] and extend to other potentials in section 5.2.2. Section(5.3) discusses the impact of introducing multiple intermediate barriers in both linear and non-linear potential landscapes. It is shown that a systematic arrangement of barriers can lead to a successive reduction in the MFPT with increasing number of barriers employed. We conclude in Sec. 5.4 with a future outlook. Some additional details (including the effect of intermediate barriers to the fluctuations in first-passage time) are included to the Appendix E.

5.1 Setup and review of the first-passage formalism

Consider a Brownian particle, whose position $x(t)$ is described by the overdamped Langevin equation in an external potential $U(x)$ [3, 4]

$$\dot{x}(t) = -\frac{U'(x)}{\gamma} + \sqrt{2D}\xi(t), \tag{5.1}$$

where $\xi(t)$ is a Gaussian white noise with the following statistical properties

$$\langle \xi(t) \rangle = 0, \qquad \langle \xi(t)\xi(t') \rangle = \delta(t - t'). \tag{5.2}$$

By the fluctuation dissipation theorem, $D = k_B T/\gamma$, where γ is the viscosity of the surrounding medium, which we assume to be unity, implying $D = k_B T$. We confine the particle in the region $x \in [0, 1]$ as shown in Fig. 5.1(a). The particle starts from $x_0 \in [0, 1]$ and it must surmount a potential barrier of height $\Delta U = U(x =$

$1) - U(x = 0)$, in order to be absorbed at $x = 1$. Furthermore, without loss of generality, we set $U(x = 0) = 0$ which implies that $U(x = 1) = \Delta U$.

In this specific set up, the MFPT, $\mathcal{T}(x_0)$, is the average time it takes for the particle to get absorbed at $x = 1$ starting from an initial position $x_0 \in [0, 1]$. To find $\mathcal{T}(x_0)$, we start by writing the backward Fokker Planck equation, for the survival probability $\mathcal{S}(t, x_0)$, which denotes the probability that the particle has not been absorbed up to time t, given that it started at position x_0 at $t = 0$. From $\mathcal{S}(t, x_0)$, the first-passage time density is derived using

$$\mathcal{F}(t, x_0) = -\frac{\partial}{\partial t}\mathcal{S}(t, x_0), \tag{5.3}$$

where $\mathcal{F}(t, x_0)dt$ represents the probability that the particle has been absorbed in the time between t and $t + dt$. The MFPT is then obtained using the following relation

$$\mathcal{T}(x_0) = \int_0^\infty t\,\mathcal{F}(t, x_0)dt, \tag{5.4}$$

which satisfies the following backward Fokker-Planck equation [20]:

$$-U'(x_0)\frac{\partial}{\partial x_0}\mathcal{T}(x_0) + k_B T\frac{\partial^2}{\partial x_0^2}\mathcal{T}(x_0) = -1, \tag{5.5}$$

where note that the initial position x_0 is now being treated as a variable [20]. To determine $\mathcal{T}(x_0)$, this equation must be solved subject to the two boundary conditions

$$\partial_{x_0}\mathcal{T}(x_0)\Big|_{x_0=0} = 0, \quad \text{and} \qquad \mathcal{T}(x_0 = 1) = 0. \tag{5.6}$$

To compute the corresponding MFPT for an arbitrary potential, sometimes it is useful to recast Eq. (5.5) into an integral form [20]

$$\mathcal{T}(x_0) = \frac{1}{k_B T}\int_{x_0}^{1} dx'' e^{U(x'')/k_B T}\int_0^{x''} dx' e^{-U(x')/k_B T}, \tag{5.7}$$

where we have already imposed the boundary conditions. Setting $x_0 = 0$, we will henceforth denote the MFPT as $\mathcal{T}$. Moreover, we will also adopt the following notation: U_N^{L} refers to a potential with N barriers/kinks, where each segment is linear. The associated MFPT for this potential is denoted by $\mathcal{T}_N^{\mathrm{L}}$. Similarly, U_N^{H} represents a potential with N barriers/kinks, where each segment is harmonic. The corresponding MFPT for this potential is denoted by $\mathcal{T}_N^{\mathrm{H}}$.

5.2 Introducing one intermediate barrier

In this section, we demonstrate that introducing an intermediate barrier (or kink) in potential landscapes and adjusting the strength of the segments on either side of the kink, while keeping the kink position and overall barrier height fixed, can reduce the MFPT compared to the original potential profile.

In subsection 5.2.1, we briefly reproduce the results of Palyulin and Metzler [68] for the case of a linear potential. In subsection 5.2.2, we extend it to consider a harmonic potential, investigating whether such modification results in a reduction of the MFPT in this case as well.

5.2.1 MFPT reduction in linear potential

Consider a linear potential described as follows:

$$\frac{U_0^{\mathrm{L}}(x)}{\Delta U} = x, \qquad 0 \leq x \leq 1 \tag{5.8}$$

To determine the MFPT associated with this potential, we solve Eq. (5.5) subject to the two boundary conditions in Eq. (5.6). This leads to the following expression

for the MFPT for the particle starting at $x_0 = 0$:

$$\mathcal{T}_0^{\mathrm{L}} = \frac{1}{\Delta U^2}(k_B T e^{\Delta U/k_B T} - \Delta U - k_B T). \tag{5.9}$$

We now modify the linear potential into a piecewise-linear form consisting of two segments, defined as:

$$\frac{U_1^{\mathrm{L}}(x)}{\Delta U} = \begin{cases} k_1 x, & 0 \le x \le a \\ k_2(x-a) + k_1 a, & a \le x \le 1 \end{cases} \tag{5.10}$$

where, k_1 and k_2 can be thought of as the strength of the potential segments which can take any real values. Imposing the setup constraint $U_1^{\mathrm{L}}(x = 1) = \Delta U$ implies

$$\Delta U = \Delta U[k_1 a + k_2(1-a)] \tag{5.11}$$

Fig. 5.2(a) depicts this potential, Eq. (5.10), for one particular values of k_1, k_2 and a. To determine the associated MFPT, we solve Eq. (5.5) separately over two regions: Region I, defined on the interval $x_0 \in [0, a]$, and Region II, defined on $x_0 \in [a, 1]$. The general solutions in each region contain constants of integration, which are determined by enforcing the two boundary conditions, together with the following matching conditions at the position of the kink (see Appendix E.1 for details)

$$\mathcal{T}_{1,I}^{\mathrm{L}}(x_0 = a) = \mathcal{T}_{1,II}^{\mathrm{L}}(x_0 = a) \tag{5.12}$$

and

$$\partial_{x_0}\mathcal{T}_{1,I}^{\mathrm{L}}(x_0 = a) = \partial_{x_0}\mathcal{T}_{1,II}^{\mathrm{L}}(x_0 = a) \tag{5.13}$$

where, $\mathcal{T}_{1,I}^{\mathrm{L}}(x_0)$ (or $\mathcal{T}_{1,II}^{\mathrm{L}}(x_0)$) denotes the MFPT if the particle starts in region I (or II). Applying these conditions determines the MFPT as a function of x_0. For

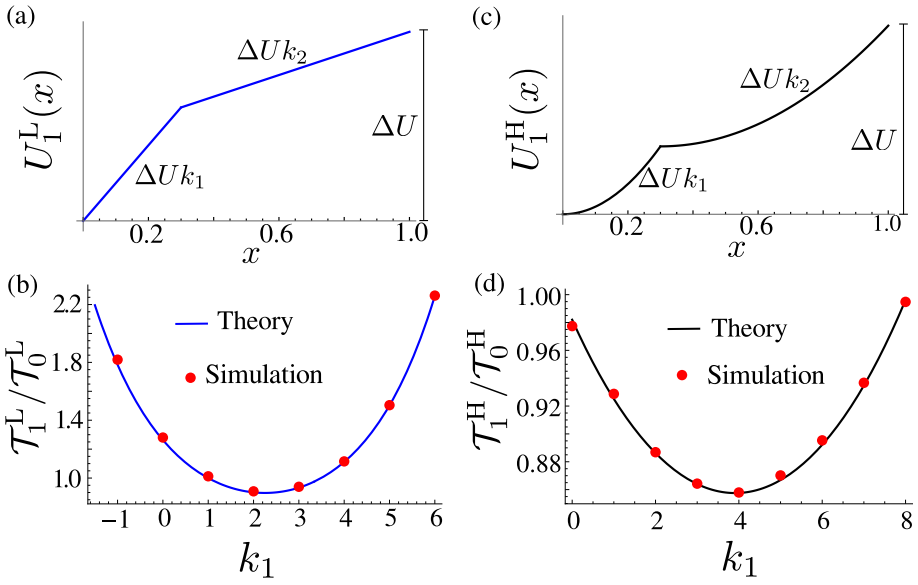

Figure 5.2: Panels (a) & (c): Piecewise linear and harmonic potential with a single kink at $x = a = 0.3$. Panel (b): The inverse speed up factor, $\mathcal{T}_1^{\mathrm{L}}/\mathcal{T}_0^{\mathrm{L}}$, for linear case is plotted as a function of k_1 with $\Delta U = 3$ and $a = 0.3$. For a range of k_1 values, $\mathcal{T}_1^{\mathrm{L}}/\mathcal{T}_0^{\mathrm{L}}$ is less than 1, implying that the modification has accelerated the process completion in these regimes. Panel (d): The inverse speed-up factor, $\mathcal{T}_1^{\mathrm{H}}/\mathcal{T}_0^{\mathrm{H}}$, for harmonic case is plotted as a function of k_1 for $\Delta U = 3$ and $a = 0.3$. Similar to the linear case, $\mathcal{T}_1^{\mathrm{H}}/\mathcal{T}_0^{\mathrm{H}} < 1$ for several k_1 values. Simulation data are shown as points, and the analytical solution is plotted as continuous curve and $k_B T$ is taken to be 1.

$x_0 = 0$, it takes the following form

$$\begin{aligned}\mathcal{T}_1^{\mathrm{L}} = &-\frac{k_BT}{\Delta U^2}\Big(\frac{1}{k_1^2}+\frac{1}{k_2^2}\Big) - \frac{a}{k_1\Delta U} - \frac{1-a}{k_2\Delta U} + \frac{k_BT}{k_1k_2\Delta U^2} \\ &+ \frac{k_BT}{\Delta U^2}\Big(\frac{1}{k_1^2}-\frac{1}{k_1k_2}\Big)e^{ak_1\Delta U/k_BT} + \frac{k_BT}{k_1k_2\Delta U^2}e^{\Delta U/k_BT} \\ &+ \frac{k_BT}{\Delta U^2}\Big(\frac{1}{k_2^2}-\frac{1}{k_1k_2}\Big)e^{k_2(1-a)\Delta U/k_BT}\end{aligned} \tag{5.14}$$

At fixed values of a and ΔU, MFPT only depends on k_1 and k_2. However, due to the constraint in Eq. (5.11), only one of k_1 and k_2 is free. We take k_1 to be the free parameter so that k_2 is automatically determined by $k_2 = (1 - k_1a)/(1 - a)$. In Fig. 5.2(b), we plot $\mathcal{T}_1^{\mathrm{L}}/\mathcal{T}_0^{\mathrm{L}}$ as a function of k_1 for fixed $a = 0.3$. Quite interestingly, for a range of k_1 values, this ratio remains below unity, implying that the modification leads to a reduction in the MFPT compared to the unmodified case in this parameter regime. This reduction can be attributed to the interplay of the times taken in traversing the two segments of the modified linear potential [68]. By tuning the strengths k_1 and k_2, the additional time required to cross the steeper segment—relative to crossing the same spatial portion of unmodified potential with strength ΔU—can be outweighed by the time gained on the shallower segment. For appropriate choices of k_1 and k_2, this trade-off leads to a net decrease in the MFPT compared to the unmodified case. To quantify this, we introduce the factor speed-up which will be discussed next.

Maximal speedup for the process completion:

We define the speedup factor as the ratio of the MFPT corresponding to the original unmodified potential to that corresponding to the potential modified by the introduction of intermediate barrier(s). In the present case, it is given by $\mathcal{T}_0^{\mathrm{L}}/\mathcal{T}_1^{\mathrm{L}}$. A ratio less than unity indicates that the modification results in slowing down the process, whereas a ratio greater than unity signifies the acceleration of the process.

In Fig. 5.2(b), we plot the inverse of this factor with k_1 for a given a, which shows that for a range of k_1 values, the inverse speedup factor $\mathcal{T}_1^{\mathrm{L}}/\mathcal{T}_0^{\mathrm{L}} < 1$, implying that in this range the first passage process is accelerated by the modified potential, as compared to the unmodified one.

Further, as k_1 is varied, the inverse speed-up factor $\mathcal{T}_1^{\mathrm{L}}/\mathcal{T}_0^{\mathrm{L}}$ exhibits a minimum at a specific value, denoted by k_1^*. We denote this minimum MFPT by $\mathcal{T}_1^{\mathrm{L}^*} = \mathcal{T}_1^{\mathrm{L}}|_{k_1=k_1^*}$, so that the speed-up ratio $\mathcal{T}_0^{\mathrm{L}}/\mathcal{T}_1^{\mathrm{L}^*}$ is maximum. The inverse maximal speedup factor is plotted as a function of a in Fig. 5.3(b). For $a < 1/2$, the optimal strengths satisfy $k_1^* > k_2^*$, whereas for $a > 1/2$, $k_1^* < k_2^*$, indicating that in the optimal configuration (See Fig. 5.3(a) for a few representative optimal potential profiles.), the region with the steeper strength occupies a smaller fraction of the spatial domain. Interestingly, $\mathcal{T}_1^{\mathrm{L}^*}/\mathcal{T}_0^{\mathrm{L}} \leq 1$, with equality only at $a = 1/2$. This implies that the minimum MFPT is strictly smaller than the MFPT of the unmodified linear potential, or in other words, the maximal speed-up ratio is greater than 1 for all $a \neq 1/2$. At $a = 1/2$, the equality $\mathcal{T}_1^{\mathrm{L}^*} = \mathcal{T}_0^{\mathrm{L}}$ arises because the optimal strengths satisfy $k_1^* = k_2^*$ (see Fig. 5.3(b)), indicating that the optimal potential coincides with the original linear potential. These observations demonstrate that introducing an intermediate barrier into a linear potential enables a robust reduction in MFPT and, therefore, a robust speeding-up of the process completion across the entire range of a.

5.2.2 MFPT reduction in harmonic potential

We now turn our attention to the motion in the presence of a harmonic potential described by

$$\frac{U_0^{\mathrm{H}}(x)}{\Delta U} = x^2, \qquad 0 \leq x \leq 1. \tag{5.15}$$

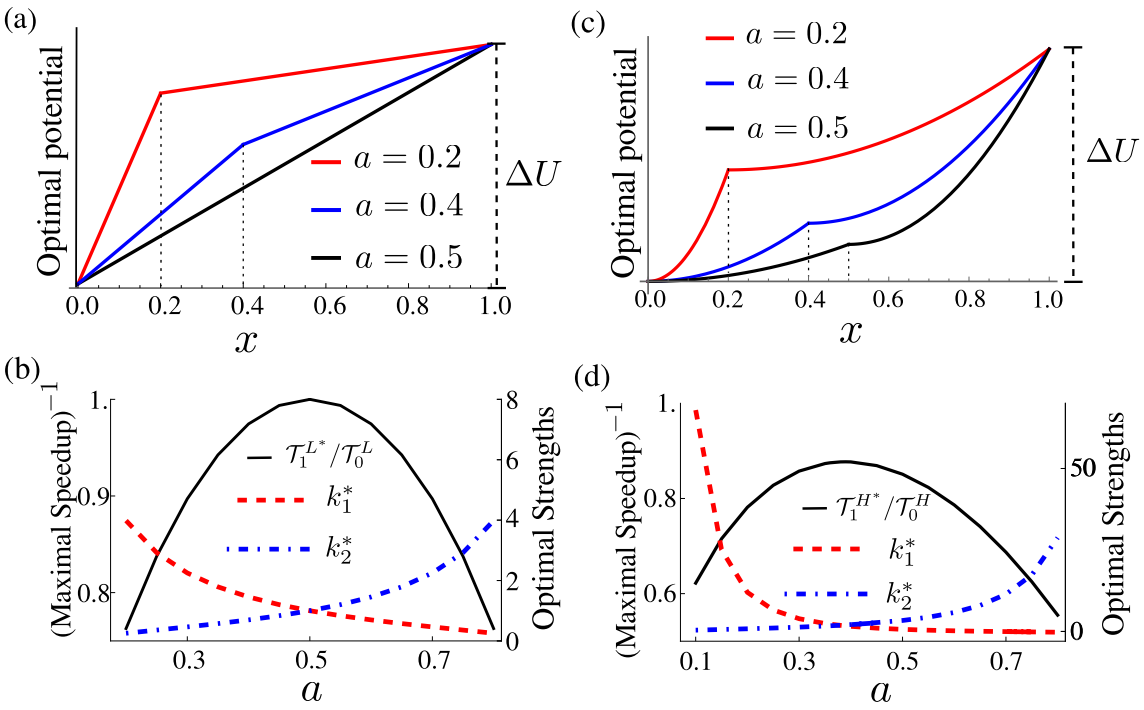

Figure 5.3: Panels (a) & (c) show the optimal potential profiles (for various values of a) for the case of one kink in linear and harmonic potentials respectively. Panel (b) shows the variation of the inverse maximal speed-up factor and the corresponding optimal strengths with a, for the linear case, with $\Delta U = 3$. The left vertical axis represents this dimensionless factor, while the right vertical axis indicates the corresponding optimal strengths, k_1^* and k_2^*. For $a = 0.5$, we observe $k_1^* = k_2^*$, implying that the optimal potential is the original linear potential itself in this case from panel (a). Panel (d) depicts the variation of these quantities for harmonic case, for $\Delta U = 3$. It shows that the inverse maximal speed-up factor never reaches unity. Similar to the linear case, there exists a range of a values for which $k_1^* > k_2^*$, while for other values, $k_2^* > k_1^*$ as shown in panel (d). The MFPTs are determined analytically and the corresponding optimal values have been found numerically, while fixing k_BT to unity.

The corresponding MFPT for the particle, starting at $x_0 = 0$, can be obtained by solving Eq. (5.5) with the two boundary conditions, and reads [100]

$$\mathcal{T}_0^{\mathrm{H}} = \frac{1}{2k_BT}\,{}_2F_2\Big(1,1;\frac{3}{2},2;\frac{\Delta U}{k_BT}\Big) \tag{5.16}$$

where ${}_pF_q(a_1,\cdots,a_p;b_1,\cdots,b_q;z)$ stands for the generalized hypergeometric function. We now introduce a kink in the harmonic potential at $x = a$ (see Fig. 5.2(c)) defining a piecewise harmonic potential as follows

$$\frac{U_1^{\mathrm{H}}(x)}{\Delta U} = \begin{cases} k_1x^2, & 0 \le x \le a \\ k_2(x-a)^2 + k_1a^2 & a \le x \le 1 \end{cases} \tag{5.17}$$

where, k_1 and k_2 denote the strength of the potential segments which can take any real value. The set up constraint naturally implies

$$U_1^{\mathrm{H}}(x=1) = \Delta U = \Delta U[k_1a^2 + k_2(1-a)^2]. \tag{5.18}$$

The associated MFPT for this modified potential is derived following Section 5.2.1, yielding

$$\begin{aligned}\mathcal{T}_1^{\mathrm{H}} = {} & \frac{e^{\frac{a^2k_1\Delta U}{k_BT}}\,\pi\, erf\left(\frac{a\sqrt{k_1\Delta U}}{\sqrt{k_BT}}\right)\, erfi\left(\frac{(1-a)\sqrt{k_2\Delta U}}{\sqrt{k_BT}}\right)}{4\sqrt{k_1k_2}\Delta U} \\ & - \frac{\pi\, erf\left(\frac{(1-a)\sqrt{k_2\Delta U}}{\sqrt{k_BT}}\right)\, erfi\left(\frac{(-1+a)\sqrt{k_2\Delta U}}{\sqrt{k_BT}}\right)}{4k_2\Delta U} \\ & + \frac{a^2}{2k_BT}\,{}_2F_2\left(1,1;\frac{3}{2},2;\frac{a^2k_1\Delta U}{k_BT}\right) \\ & - \frac{(-1+a)^2}{2k_BT}\,{}_2F_2\left(1,1;\frac{3}{2},2;-\beta\right),\end{aligned} \tag{5.19}$$

where $\beta = (1-a)^2k_2\Delta U/k_BT$ and $erf(z) = \frac{2}{\sqrt{\pi}}\int_0^z e^{-y^2}dy$ denotes the error function, $erfi(z) = -i\,\mathrm{erf}(iz)$ denotes the imaginary error function. Following a similar approach as in Section 5.2.1, we obtain Fig. 5.2(d), which illustrates the dependence

of the inverse speed-up factor, $\mathcal{T}_1^{\mathrm{H}}/\mathcal{T}_0^{\mathrm{H}}$, on k_1 for the harmonic case. As in the linear case, $\mathcal{T}_1^{\mathrm{H}}/\mathcal{T}_0^{\mathrm{H}} < 1$ over a range of k_1, indicating a reduced MFPT for the modified potential compared to the unmodified harmonic case.

Maximal speedup for the process completion:

Like the piecewise-linear potential, the inverse speed-up factor exhibits a minimum as shown in Fig. 5.2(d), which corresponds to the maximal speedup of the process completion. Further, Fig. 5.3(d) presents the variation of the inverse maximal speed-up factor, $\mathcal{T}_1^{\mathrm{H}^*}/\mathcal{T}_0^{\mathrm{H}}$, and optimal strengths k_1^* and k_2^* with a, where k_1^* (and k_2^*) for a given a corresponds to the minimum MFPT and, therefore, the maximal speedup in the process completion for that specific value of a. See Fig. 5.3(c) for a few representative optimal potential profiles. Further, Fig. 5.3(d) shows that there exists a range of the parameter a such that $k_1^* > k_2^*$, and at other values, $k_2^* > k_1^*$. Interestingly, we find $\mathcal{T}_1^{\mathrm{H}^*}/\mathcal{T}_0^{\mathrm{H}} < 1$ for all a, demonstrating a robust reduction in the optimal MFPT across the entire range of a, thus showcasing a similar optimization.

5.3 Introducing multiple intermediate barriers

Previously, we analyzed the effect of incorporating a single intermediate barrier on the controlled reduction of the mean first-passage time (MFPT). The aim of this section is to extend this analysis by introducing multiple intermediate barriers in the potential structure. As a means to achieve this, the potential is restructured into segments with alternating strengths of k_1 and k_2, starting with k_1; an illustration for a three-segment case is provided in Fig. 5.4. This introduces intermediate barriers, with their number N equal to one less than the number of segments, $N + 1$. For simplicity, we assume the kinks are uniformly spaced in the interval $x \in [0, 1]$, located at $x = a, 2a, \ldots, Na$ with $a = 1/(N + 1)$, where N is the number of kinks.

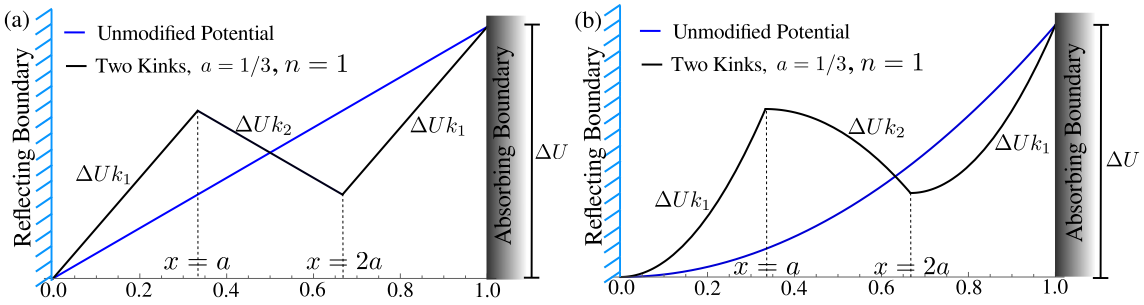

Figure 5.4: The figure presents the linear and harmonic potentials (in blue) along with their corresponding modified potentials after introducing $N = 2n = 2$ kinks (in black), as shown in panels (a) and (b), respectively. The modified potentials consist of segments with alternating strengths k_1 and k_2. In both cases, the kinks are equally spaced and positioned at $x = a$ and $x = 2a$, where $a = 1/3$.

5.3.1 Observation I: Intermediate barriers resulting from even number of segmentations do not facilitate the further reduction of the MFPT with increasing segments

Let us consider the linear potential as in Eq. (5.8), partitioned now into $N + 1$ segments by introducing N kinks, where N is assumed to be odd. The potential then consists of $(N + 1)/2$ segments each with strengths k_1 and k_2. Under this condition, the set up constraint, $U_N^{\mathrm{L}}(x = 1) = \Delta U$, implies:

$$U_N^{\mathrm{L}}(x = 1) = \Delta U = \Delta U \frac{N+1}{2} k_1 a + \Delta U \frac{N+1}{2} k_2 a \tag{5.20}$$

We analytically solve Eq. (5.5) to compute the MFPT, $\mathcal{T}_N^{\mathrm{L}}$, using mathematica. This computation involves the two boundary conditions and $2N$ connecting conditions, two per kink (see Appendix E.1 for the details). Following the method in Section 5.2, we determine the minimum MFPT, $\mathcal{T}_N^{\mathrm{L}^*}$, for various odd values of N and compute the inverse maximal speed-up factor, $\mathcal{T}_N^{\mathrm{L}^*}/\mathcal{T}_0^{\mathrm{L}}$. Fig. 5.5(a) shows its variation along with the corresponding optimal strengths k_1^* and k_2^* as a function of odd N. The

result $\mathcal{T}_N^{\mathrm{L}^*}/\mathcal{T}_0^{\mathrm{L}} = 1$ for all odd N shows that introducing such intermediate barriers does not reduce the MFPT in the linear case.

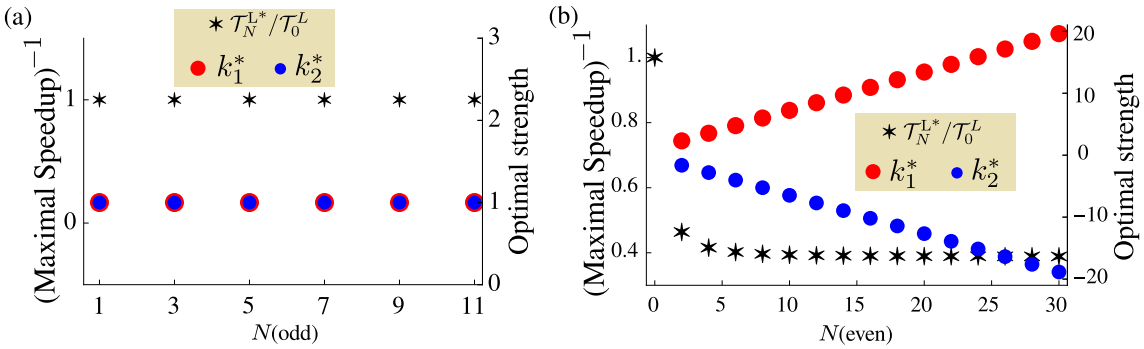

Figure 5.5: Variation of the inverse maximal speed-up factor, $\mathcal{T}_N^{\mathrm{L}^*}/\mathcal{T}_0^{\mathrm{L}}$, and the optimal strengths, with the number of kinks N. The left vertical axis represents the inverse maximal speed-up factor, while the right vertical axis corresponds to optimal strengths, k_1^* and k_2^*. The barrier height is fixed at $\Delta U = 5$ and $k_B T = 1$. To obtain these results, the MFPT for a given N is first computed analytically using Mathematica and the corresponding optimal MFPT is evaluated by numerical minimization. Panel (a) shows that for any odd N, the inverse maximal speed-up factor is unity, indicating no reduction in the MFPT. In these cases, the optimal strengths satisfy $k_1^* = k_2^*$. Panel (b) illustrates the behavior for even values of $N = 2n$. The inverse maximal speed-up factor is less than 1 and decreases monotonically, indicating successive reduction of the MFPT with increasing N. The case $N = 0$ corresponds to the unmodified linear potential.

We now analyse the case of harmonic potential. Similar to the case of linear potential, the constraint for $N+1$ harmonic segments(N odd) is

$$U_N^{\mathrm{H}}(x=1) = \Delta U = \Delta U \frac{N+1}{2} k_1 a^2 + \Delta U \frac{N+1}{2} k_2 a^2 \tag{5.21}$$

Following the same procedure as for the linear case, we compute the inverse maximal speed-up factor, $\mathcal{T}_N^{\mathrm{H}^*}/\mathcal{T}_0^{\mathrm{H}}$, and the corresponding optimal strengths k_1^* and k_2^*. Figure 5.6(a) shows their dependence on odd N. While the modified harmonic potential yields a lower MFPT than the unmodified case, the minimal MFPT increases with N, indicating that the maximum reduction occurs at $N = 1$. Thus, adding more kinks does not further accelerate the absorption.

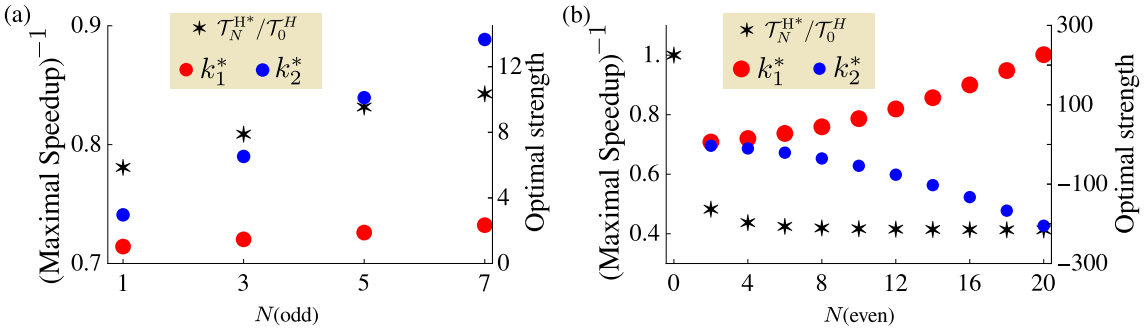

Figure 5.6: Variation of the inverse maximal speed-up factor, $\mathcal{T}_N^{\mathrm{H}^*}/\mathcal{T}_0^{\mathrm{H}}$, and the optimal strengths with N. The barrier height is fixed at $\Delta U = 5$ and $k_BT = 1$. Panel (a): For odd N, the inverse speed-up factor is less than one, indicating reduced MFPT as compared to that for unmodified potential. However, additional kinks does not lead to further reduction. Panel (b) illustrates the behavior for even values of $N = 2n$, where the introduction of kinks leads to a reduction in the optimal MFPT. Moreover, the minimal MFPT decreases monotonically with increasing N, indicating that the introduction of additional kinks further reduces the MFPT. The case $N = 0$ corresponds to the unmodified harmonic potential.

5.3.2 Observation II: Intermediate barriers resulting from odd number of segmentations of potential landscapes do facilitate the successive reduction of the MFPT

Let us now modify the linear potential as in Eq. (5.8) by dividing it into three segments (two kinks) as shown in Fig. 5.4(a). The resulting piecewise-linear potential is given by

$$\frac{U_2^{\mathrm{L}}(x)}{\Delta U} = \begin{cases} k_1 x & 0 \le x \le a \\ k_2(x-a) + k_1 a & a \le x \le 2a \\ k_1(x-2a) + (k_1+k_2)a & 2a \le x \le 1 \end{cases} \tag{5.22}$$

Here, the kinks are located at $x = a$ and $x = 2a$, with $a = 1/3$. Imposing the constraint $U_2^{\mathrm{L}}(x = 1) = \Delta U$ yields $\Delta U = \Delta U[2k_1 + k_2]a$. Generalizing to N kinks (with even N), the potential is divided into $N + 1$ segments. Letting $n = N/2$, the

condition $U_N^{\mathrm{L}}(x=1) = \Delta U$ gives:

$$\Delta U = \Delta U(n+1)k_1 a + \Delta U n k_2 a \tag{5.23}$$

The inverse maximal speed-up factor, $\mathcal{T}_N^{\mathrm{L}^*}/\mathcal{T}_0^{\mathrm{L}}$, along with the corresponding optimal strengths k_1^* and k_2^* for various even values of N, is computed following the procedure outlined in Section 5.3.1. As shown in Fig. 5.5(b), the inverse maximal speed-up factor decreases with increasing N, satisfying $\mathcal{T}_N^{\mathrm{L}^*}/\mathcal{T}_0^{\mathrm{L}} < 1$ for all $N > 0$ (with $N = 0$ corresponding to the unmodified linear potential). This monotonic decrease indicates that adding more such intermediate barriers is beneficial.

We now analyze the case of harmonic potential. As an example, consider partitioning the harmonic potential in Eq. (5.15) into three segments, by introducing two kinks. The resulting piecewise-harmonic potential is given by

$$\frac{U_2^{\mathrm{H}}(x)}{\Delta U} = \begin{cases} k_1 x^2 & 0 \le x \le a \\ k_2(x-a)^2 + k_1 a^2 & a \le x \le 2a \\ k_1(x-2a)^2 + (k_1+k_2)a^2 & 2a \le x \le 1 \end{cases} \tag{5.24}$$

See Fig. 5.4(b) for a schematic of this potential. Imposing $U_2^{\mathrm{H}}(x=1) = \Delta U$ implies $\Delta U = \Delta U(2k_1 + k_2)a^2$. For any N(even) number of kinks, the constraint becomes

$$U_N^{\mathrm{H}}(x=1) = \Delta U = \Delta U(n+1)k_1 a^2 + \Delta U n k_2 a^2 \tag{5.25}$$

where, $n = N/2$. A similar analysis to that for the linear case reveals that the inverse maximal speed-up factor, $\mathcal{T}_N^{\mathrm{H}^*}/\mathcal{T}_0^{\mathrm{H}}$, decreases monotonically with increasing number of such intermediate barriers, or equilvalently, with increasing even N. See Fig. 5.6(b). The figure also shows the variation of k_1^* and k_2^* with N.

We have thus demonstrated that the minimum MFPT decreases monotonically with

increasing even values of N in both the linear and harmonic cases. This monotonic decrease implies that the maximal speedup achievable in the completion time of the process increases with increasing even N, i.e., $\mathcal{T}_0^{\mathrm{L}}/\mathcal{T}_{N+2}^{\mathrm{L}^*} > \mathcal{T}_0^{\mathrm{L}}/\mathcal{T}_N^{\mathrm{L}^*}$ (similarly $\mathcal{T}_0^{\mathrm{H}}/\mathcal{T}_{N+2}^{\mathrm{H}^*} > \mathcal{T}_0^{\mathrm{H}}/\mathcal{T}_N^{\mathrm{H}^*}$ for the harmonic case) for all even N. This behavior is attributed to "additional degrees of freedom" which emanates from the incorporation of more kinks/barriers into the potential profile. Each pair of additional kinks (i.e., increasing N to $N+2$) seems to introduce greater control in shaping the potential profile as the enhanced degree redistributes the strengths of the uphill and downhill segments in a manner that reduces the overall traversal time, resulting in $\mathcal{T}_{N+2}^{\mathrm{L}^*} < \mathcal{T}_N^{\mathrm{L}^*}$ (and $\mathcal{T}_{N+2}^{\mathrm{H}^*} < \mathcal{T}_N^{\mathrm{H}^*}$).

We continue to investigate the behavior of the optimal potential profiles in the large and even $N \to \infty$ limit. To this end, we plotted the optimal profiles for large $N(= 30)$ in Fig. 5.7, which is helpful in understanding the asymptotic structure. To determine the scaling of the optimal strength k_1^*, we fitted the dataset $\{k_1^*, N\}$ for even values of N from $N = 2$ to $N = 20$, and confirmed that it correctly gives the result at larger values of N (up to $N = 100$). For $\Delta U = 5$, the resulting fit for the linear case is

$$k_1^* \approx 1.058 + 0.618\, N, \tag{5.26}$$

while for the harmonic case it is

$$k_1^* \approx 1.185 + 1.505\, N + 0.487\, N^2, \tag{5.27}$$

where the symbol $\approx$ indicates that the coefficients have been rounded to three decimal places. Once k_1^* is known, the corresponding value of k_2^* can be computed using the constraint equations, Eq. (5.23) for the linear case and Eq. (5.25) for the harmonic case.

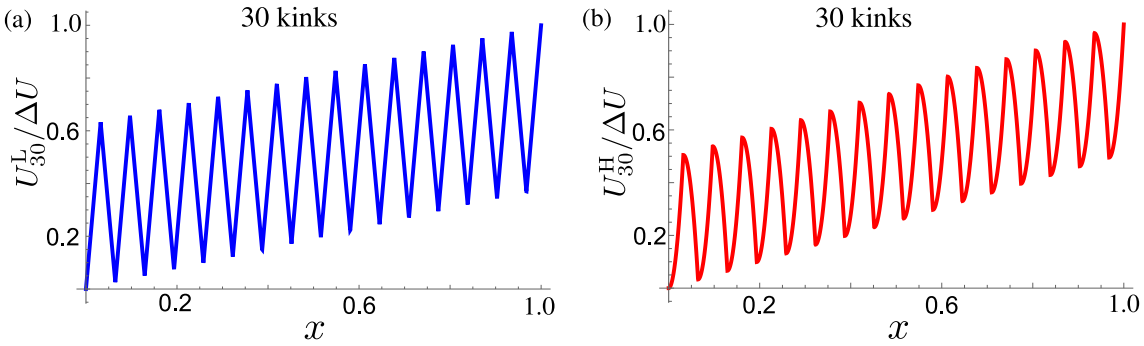

Figure 5.7: Panels (a) & (b): Optimally restructured potential configurations in linear and harmonic case for $N = 30$, $\Delta U = 5$ and $k_B T = 1$.

5.4 Conclusions and discussion

In this work, we investigate how the mean first-passage time (MFPT) of a Brownian particle can be controlled by tailoring the shape of the external potential. We show that the MFPT required for a particle to cross a potential barrier of height ΔU can be markedly reduced by systematically modifying the potential landscape, without altering the overall barrier height. In particular, we demonstrate that replacing a single large barrier with a sequence of smaller intermediate barriers—constructed by partitioning the landscape into segments via the introduction of kinks—leads to a significant acceleration of the first-passage process.

These observations were based on rigorous analysis of the MFPT in a linear and harmonic potential, both unperturbed and modified likewise. We began our analysis by demonstrating that the introduction of a single intermediate barrier in the potential can result in the reduction of the MFPT compared to that of the original unmodified potential. Building on this, we extended the study to the case of multiple equidistant kinks, denoted by N, and investigated the corresponding effects on the MFPT. We further examined a speed-up factor to quantitatively account for the efficacy of the transition rendered by the intermediate barriers. The results are summarized in Table 5.1.

Table 5.1: Summary of main results. We recall that $\mathcal{T}_N^{\mathrm{L}}$ denotes the MFPT for a piecewise linear potential with $N+1$ segments or N kinks. The case $N=0$ refers to the pure linear potential. The MFPT for the piecewise harmonic potential with N kinks is $\mathcal{T}_N^{\mathrm{H}}$, where again the case $N=0$ refers to the pure harmonic potential.

Potential Type	**No. of kinks (N)**	**Optimal Shape**	**MFPT Behavior with N**
Piecewise Linear	Even	Non-uniform segment strengths	$\mathcal{T}_N^{\mathrm{L}^*} < \mathcal{T}_0^{\mathrm{L}}$ and $\mathcal{T}_N^{\mathrm{L}^*}$ monotonically decreases with N
	Odd	Uniform linear potential	Linear case always optimal
Piecewise Harmonic	Even	Non-uniform segment strengths	$\mathcal{T}_N^{\mathrm{H}^*} < \mathcal{T}_0^{\mathrm{H}}$ and $\mathcal{T}_N^{\mathrm{H}^*}$ monotonically decreases with N
	Odd	Non-uniform segment strengths	$\mathcal{T}_N^{\mathrm{H}^*} < \mathcal{T}_0^{\mathrm{H}}$ for some N, but $\mathcal{T}_N^{\mathrm{H}^*}$ increases with N

Similar to the MFPT, another important observable in the study of first-passage processes is the variance of the first-passage time(FPT), which typically characterizes the fluctuations around the MFPT. While the MFPT is the average time required for a stochastic process to reach the target for the first time, the variance quantifies the deviation around the MFPT. Although a detailed investigation of the variance of the FPT lies beyond the objective of this work, we briefly examine it for a few cases. We first study the variance corresponding to linear potential (as in Eq. (5.8)), and that corresponding to modified linear potential with one intermediate barrier (see Eq. (5.10)). We then follow this analysis for the case of harmonic potential (as in Eq. (5.15)) and for modified harmonic potential with one intermediate barrier (see Eq. (5.17)). Skipping details from the analysis presented in Appendix E.2, we can conclude that adding intermediate barrier can also reduce the fluctuations of the escape time of a Brownian particle.

In summary, this study has demonstrated that modifying the potential landscape

can be an effective strategy for reducing the mean first-passage time (MFPT) and the variance of the first-passage time of an overdamped Brownian particle. In particular, the piecewise harmonic potential offers a realistic and experimentally accessible model. It can be readily implemented using arrays of optical traps [125–127], making it a practical framework for experimentalists and a promising tool for exploring such mechanisms in real systems.

This work also points out to several important directions that remain open. Although our findings suggest that introducing intermediate barriers into complex potential landscapes generally lowers the MFPT, a rigorous theoretical proof of this observation is certainly lacking. Establishing such a result or identifying the extent to which these controls are robust would be a crucial step forward, with potential implications for processes such as molecular or ionic transport through membranes and channels [33, 71]. Another promising direction is to explore the optimal number of subdivisions in complex potential landscapes, extending similar ideas as in [128], where the potential was partitioned into linear segments within a specific setup which preserves the area under the potential. Unlike our current work that achieves MFPT reduction by tuning the strengths of the potential segments, this optimization with regard to the number of barriers could be another prospective robust control over the barrier crossing time. In addition, it would be worthwhile to investigate whether similar reductions in first-passage times can be achieved for inertial, underdamped Brownian particles through analogous modifications of the potential. Another interesting direction involves examining the effect of intermediate barriers in anomalous diffusive systems. Indeed, a study by Palyulin and Metzler [129] demonstrated that the first-passage dynamics of a subdiffusive continuous-time random walk can be accelerated by introducing a finite potential barrier. However, the influence of multiple intermediate barriers (as well as their effect to other non-diffusive processes such as [130]), as done in this paper, on the MFPT in such systems remains to be explored.

Another promising direction would be to investigate whether introducing intermediate barriers can accelerate the mean first-passage time (MFPT) in stochastic processes with multiplicative noise, such as geometric Brownian motion [131]. Finally, it would be interesting to explore the combined optimization effects arising from the interplay between intermediate barriers and stochastic resetting. However, one may need to adapt an annealed resetting algorithm [132] to see such an effect in confined geometries such as ion channels [60, 71, 133].

Chapter 6

Conclusions

Concluding, this thesis was broadly divided into two parts. The first part was dedicated to the formulation of the Arrhenius law for interacting diffusive systems, along with an analysis of its inference properties. The second part examined the role of finite intermediate barriers in accelerating the barrier-crossing dynamics of a single Brownian particle. In what follows, we summarize the central results arising from this thesis and outline potential directions for future research.

In Chapters 2, 3, and 4, we have presented a detailed study of the generalized Arrhenius law for interacting diffusive systems. In Chapter 2, we derived this generalized form and demonstrated that, in contrast to the conventional Arrhenius law, the exponential term is non-universal, in the sense that it depends on detailed features of the potential landscape and interparticle interactions, and hence is not determined solely by the barrier height. Despite this non-universality, our analysis revealed the emergence of two distinct universality classes, which we termed the Arrhenius universality class and the excluded-volume universality class. Systems with excluded-volume interactions fall into the excluded-volume universality class, wherein the exponential term in the escape rate assumes a common form across different models. In contrast, systems without excluded-volume interactions belong to the Arrhenius universality class, for which the exponential term reduces to

that of the conventional Arrhenius law. In Chapter 3, we presented a perturbative hydrodynamic approach to analytically validate the existence and the range of validity for the two universality classes. In Chapter 4, we illustrated how one can use the generalized Arrhenius law for interacting diffusive systems with excluded volume interactions to count the number of metastable states in an unknown energy landscape.

Despite these advances in the formulation of the Arrhenius law for interacting systems, several important regimes remain unexplored. One such direction is the extension to multi-species interacting systems, where the diffusivity and mobility become matrices [104]. Understanding how inter-species interactions influence the Arrhenius law constitutes an interesting open problem. Another important avenue is the investigation of the Arrhenius law in non-diffusive interacting systems [119, 120], as well as in systems with soft interactions that go beyond lattice gas models [121, 122]. A further promising direction is the numerical inference of metastable states in unknown potential landscapes using polymer systems [134], which provide a natural and physically realistic platform to test the inference property of the generalized Arrhenius law developed in Chapter 4.

In Chapter 5, we investigated the dynamics of a single Brownian particle in a confined domain, where the particle must surmount a potential barrier of height ΔU prior to absorption. We showed that appropriate modifications of the potential landscape, achieved through the introduction of finite intermediate barriers while preserving the overall barrier height, can lead to a substantial reduction in the mean barrier-crossing time. Moreover, we demonstrated that the inclusion of additional intermediate barriers can further enhance this reduction, thereby systematically expediting the crossing dynamics. This effect was observed to hold for both linear and nonlinear potential landscapes.

An important direction for future research is to investigate the effect of introducing

finite intermediate barriers on the mean barrier-crossing time of active particles [13, 135–137], where a nontrivial interplay between self-propulsion and the modified potential landscape is expected to arise. Another promising avenue is to examine the influence of intermediate barriers on barrier-crossing dynamics in viscoelastic media in which the evolution of the particle is non-Markovian [138]. In addition, it would be worthwhile to explore alternative mechanisms for reducing the mean barrier-crossing time. One such approach is to consider space-dependent diffusivity [139] and to determine the constrained optimal diffusivity profile, that minimizes the mean crossing time. The imposition of constraint is essential as the unconstrained optimal diffusivity profile is trivially infinite everywhere. A natural example of such a constraint is a fixed diffusivity budget, whereby the spatial integral of the diffusivity over the domain is held constant.

A further direction is to extend the analysis presented in Chapter 5 to higher-dimensional systems. In such settings, the presence of multiple escape pathways introduces additional complexity, and it would be of great interest to investigate how the interplay between these pathways and intermediate barriers influences the barrier-crossing dynamics, and whether a comparable reduction in the crossing time can be achieved as in one dimension.

Bibliography

[1] Mehran Kardar. *Statistical physics of fields*. Cambridge University Press, 2007.

[2] Peter Hänggi and Fabio Marchesoni. Introduction: 100years of brownian motion. *Chaos: An Interdisciplinary Journal of Nonlinear Science*, 15(2), 2005.

[3] William Coffey and Yu P Kalmykov. *The Langevin equation: with applications to stochastic problems in physics, chemistry and electrical engineering*, volume 27. World Scientific, 2012.

[4] Robert Zwanzig. *Nonequilibrium statistical mechanics*. Oxford university press, 2001.

[5] Kerson Huang. *Introduction to statistical physics*. Chapman and Hall/CRC, 2009.

[6] Udo Seifert. Stochastic thermodynamics: principles and perspectives. *The European Physical Journal B*, 64(3):423–431, 2008.

[7] Luca Peliti and Simone Pigolotti. *Stochastic thermodynamics: an introduction*. Princeton University Press, 2021.

[8] Lorenzo Bertini, Alberto De Sole, Davide Gabrielli, Giovanni Jona-Lasinio, and Claudio Landim. Macroscopic fluctuation theory. *Reviews of Modern Physics*, 87(2):593–636, 2015.

[9] Lorenzo Bertini, Alberto De Sole, Davide Gabrielli, Giovanni Jona-Lasinio, and Claudio Landim. Macroscopic fluctuation theory for stationary non-equilibrium states. *Journal of Statistical Physics*, 107(3):635–675, 2002.

[10] Lorenzo Bertini, A De Sole, Davide Gabrielli, Giovanni Jona-Lasinio, and Claudio Landim. Non equilibrium current fluctuations in stochastic lattice gases. *Journal of statistical physics*, 123(2):237–276, 2006.

[11] Bernard Derrida. Non-equilibrium steady states: fluctuations and large deviations of the density and of the current. *Journal of Statistical Mechanics: Theory and Experiment*, 2007(07):P07023–P07023, 2007.

[12] Ron Elber, Dmitrii E Makarov, and Henri Orland. *Molecular kinetics in condensed phases: theory, simulation, and analysis*. John Wiley & Sons, 2020.

[13] Eric Woillez, Yongfeng Zhao, Yariv Kafri, Vivien Lecomte, and Julien Tailleur. Activated escape of a self-propelled particle from a metastable state. *Physical review letters*, 122(25):258001, 2019.

[14] Henry Eyring. The activated complex in chemical reactions. *The Journal of chemical physics*, 3(2):107–115, 1935.

[15] Merdith G Evans and Michael Polanyi. Some applications of the transition state method to the calculation of reaction velocities, especially in solution. *Transactions of the Faraday Society*, 31:875–894, 1935.

[16] Keith James Laidler, J Keith, et al. *Chemical kinetics*, volume 2. McGraw-Hill New York, 1965.

[17] Hendrik Anthony Kramers. Brownian motion in a field of force and the diffusion model of chemical reactions. *physica*, 7(4):284–304, 1940.

[18] Peter Hänggi, Peter Talkner, and Michal Borkovec. Reaction-rate theory: fifty years after kramers. *Reviews of modern physics*, 62(2):251, 1990.

[19] Vladimir Ivanovič Mel'nikov. The kramers problem: Fifty years of development. *Physics Reports*, 209(1-2):1–71, 1991.

[20] Crispin Gardiner. *Stochastic methods*, volume 4. Springer Berlin Heidelberg, 2009.

[21] Abraham Nitzan. Activated rate processes in condensed phases: The kramers theory revisited. *Advances in Chemical Physics: Evolution of Size Effects in Chemical Dynamics, Part 2*, pages 489–555, 1988.

[22] Jeffrey R Moffitt, Yann R Chemla, and Carlos Bustamante. Methods in statistical kinetics. In *Methods in enzymology*, volume 475, pages 221–257. Elsevier, 2010.

[23] Dmitrii E Makarov. *Single molecule science: physical principles and models*. CRC Press, 2015.

[24] Benny Carmeli and Abraham Nitzan. Theory of activated rate processes: Bridging between the kramers limits. *Physical Review Letters*, 51(4):233, 1983.

[25] Félix Ginot, Juliana Caspers, Matthias Krüger, and Clemens Bechinger. Barrier crossing in a viscoelastic bath. *Physical Review Letters*, 128(2):028001, 2022.

[26] Brandon R Ferrer, Juan Ruben Gomez-Solano, and Alejandro V Arzola. Fluid viscoelasticity triggers fast transitions of a brownian particle in a double well optical potential. *Physical Review Letters*, 126(10):108001, 2021.

[27] Andrei Militaru, Max Innerbichler, Martin Frimmer, Felix Tebbenjohanns, Lukas Novotny, and Christoph Dellago. Escape dynamics of active particles in multistable potentials. *Nature Communications*, 12(1):2446, 2021.

[28] Eric Woillez, Yariv Kafri, and Nir S Gov. Active trap model. *Physical Review Letters*, 124(11):118002, 2020.

[29] Lorenzo Caprini, Umberto Marini Bettolo Marconi, Andrea Puglisi, and Angelo Vulpiani. Active escape dynamics: The effect of persistence on barrier crossing. *The Journal of chemical physics*, 150(2), 2019.

[30] Lorenzo Caprini, Fabio Cecconi, and Umberto Marini Bettolo Marconi. Correlated escape of active particles across a potential barrier. *The Journal of Chemical Physics*, 155(23), 2021.

[31] Micha Peleg, Mark D Normand, and Maria G Corradini. The arrhenius equation revisited. *Critical reviews in food science and nutrition*, 52(9):830–851, 2012.

[32] Jeppe C Dyre. Colloquium: The glass transition and elastic models of glass-forming liquids. *Reviews of modern physics*, 78(3):953–972, 2006.

[33] Alice L Thorneywork, Jannes Gladrow, Yujia Qing, Marc Rico-Pasto, Felix Ritort, Hagan Bayley, Anatoly B Kolomeisky, and Ulrich F Keyser. Direct detection of molecular intermediates from first-passage times. *Science advances*, 6(18):eaaz4642, 2020.

[34] Marie Chupeau, Jannes Gladrow, Alexei Chepelianskii, Ulrich F Keyser, and Emmanuel Trizac. Optimizing brownian escape rates by potential shaping. *Proceedings of the National Academy of Sciences*, 117(3):1383–1388, 2020.

[35] Sameernandan Upadhyayula and Eli Pollak. Uniform semiclassical instanton rate theory. *The Journal of Physical Chemistry Letters*, 14(44):9892–9899, 2023.

[36] Alexander M Berezhkovskii and Dmitrii E Makarov. Single-molecule test for markovianity of the dynamics along a reaction coordinate. *The journal of physical chemistry letters*, 9(9):2190–2195, 2018.

[37] Dmitrii E Makarov. Barrier crossing dynamics from single-molecule measurements. *The Journal of Physical Chemistry B*, 125(10):2467–2476, 2021.

[38] A Barbier-Chebbah, O Bénichou, R Voituriez, and Thomas Guérin. Long-term memory induced correction to arrhenius law. *Nature Communications*, 15(1):7408, 2024.

[39] Apurba Biswas and Thomas Guérin. Correlations between rare events due to long-term memory. *arXiv preprint arXiv:2512.15479*, 2025.

[40] Mesfin Asfaw and Yohannes Shiferaw. Exploring the dynamics of dimer crossing over a kramers type potential. *The Journal of Chemical Physics*, 136(2), 2012.

[41] Esha Lyngdoh and WL Reenbohn. Escape rate of a dimer under the influence of additive colored noise: Ornstein–uhlenbeck process. *Physica A: Statistical Mechanics and its Applications*, 651:129975, 2024.

[42] RK Singh. Kramers problem for a dimer: Effect of noise correlations. *Physical Review E*, 95(4):042132, 2017.

[43] Guillaume Stirnemann and Damien Laage. Communication: On the origin of the non-arrhenius behavior in water reorientation dynamics. *The Journal of chemical physics*, 137(3), 2012.

[44] Rossitza Pentcheva, Kristen A Fichthorn, Matthias Scheffler, T Bernhard, Rupert Pfandzelter, and Helmut Winter. Non-arrhenius behavior of the island density in metal heteroepitaxy: Co on cu (001). *Physical review letters*, 90(7):076101, 2003.

[45] ACP Rosa Junior, Clebson Cruz, Wanisson Silva Santana, and Marcelo Albano Moret. Characterization of the non-arrhenius behavior of supercooled

liquids by modeling nonadditive stochastic systems. *Physical Review E*, 100(2):022139, 2019.

[46] Dirk Hennig, Colm Mulhern, Lutz Schimansky-Geier, GP Tsironis, and Peter Hänggi. Cooperative surmounting of bottlenecks. *Physics Reports*, 586:1–51, 2015.

[47] Kirone Mallick, Hiroki Moriya, and Tomohiro Sasamoto. Exact solution of the macroscopic fluctuation theory for the symmetric exclusion process. *Physical Review Letters*, 129(4):040601, 2022.

[48] Martin R Evans and Tom Hanney. Nonequilibrium statistical mechanics of the zero-range process and related models. *Journal of Physics A: Mathematical and General*, 38(19):R195–R240, 2005.

[49] Julian Kappler, Jan O Daldrop, Florian N Brünig, Moritz D Boehle, and Roland R Netz. Memory-induced acceleration and slowdown of barrier crossing. *The Journal of Chemical Physics*, 148(1), 2018.

[50] Martin R Evans, Satya N Majumdar, and Grégory Schehr. Stochastic resetting and applications. *Journal of Physics A: Mathematical and Theoretical*, 53(19):193001, 2020.

[51] Shamik Gupta and Arun M Jayannavar. Stochastic resetting: A (very) brief review. *Frontiers in Physics*, 10:789097, 2022.

[52] Martin R Evans and Satya N Majumdar. Diffusion with stochastic resetting. *Physical review letters*, 106(16):160601, 2011.

[53] Arnab Pal, Anupam Kundu, and Martin R Evans. Diffusion under time-dependent resetting. *Journal of Physics A: Mathematical and Theoretical*, 49(22):225001, 2016.

[54] Martin R Evans and Satya N Majumdar. Diffusion with resetting in arbitrary spatial dimension. *Journal of Physics A: Mathematical and Theoretical*, 47(28):285001, 2014.

[55] Shamik Gupta, Satya N Majumdar, and Grégory Schehr. Fluctuating interfaces subject to stochastic resetting. *Physical review letters*, 112(22):220601, 2014.

[56] Arnab Pal, Sarah Kostinski, and Shlomi Reuveni. The inspection paradox in stochastic resetting. *Journal of Physics A: Mathematical and Theoretical*, 55(2):021001, 2022.

[57] Marco Biroli, Hernan Larralde, Satya N Majumdar, and Grégory Schehr. Extreme statistics and spacing distribution in a brownian gas correlated by resetting. *Physical Review Letters*, 130(20):207101, 2023.

[58] Benjamin De Bruyne, Satya N Majumdar, and Grégory Schehr. Optimal resetting brownian bridges via enhanced fluctuations. *Physical Review Letters*, 128(20):200603, 2022.

[59] Arnab Pal, Viktor Stojkoski, and Trifce Sandev. Random resetting in search problems. In *Target Search Problems*, pages 323–355. Springer, 2024.

[60] Suvam Pal, Denis Boyer, Leonardo Dagdug, and Arnab Pal. Channel-facilitated transport under resetting dynamics. *The Journal of Chemical Physics*, 161(14), 2024.

[61] Rishu Kumar Singh, Ralf Metzler, and Trifce Sandev. Resetting dynamics in a confining potential. *Journal of Physics A: Mathematical and Theoretical*, 53(50):505003, 2020.

[62] Saeed Ahmad, Indrani Nayak, Ajay Bansal, Amitabha Nandi, and Dibyendu Das. First passage of a particle in a potential under stochastic resetting: A

vanishing transition of optimal resetting rate. *Physical Review E*, 99(2):022130, 2019.

[63] Karol Capała and Bartłomiej Dybiec. Optimization of escape kinetics by reflecting and resetting. *Chaos: An Interdisciplinary Journal of Nonlinear Science*, 33(10), 2023.

[64] Somrita Ray and Shlomi Reuveni. Diffusion with resetting in a logarithmic potential. *The Journal of chemical physics*, 152(23), 2020.

[65] Thomas Wellens, Vyacheslav Shatokhin, and Andreas Buchleitner. Stochastic resonance. *Reports on progress in physics*, 67(1):45–105, 2004.

[66] Marc Höll, Alon Nissan, Brian Berkowitz, and Eli Barkai. Controls that expedite first-passage times in disordered systems. *Physical Review E*, 108(3):034124, 2023.

[67] Clemens Wagner and Thomas Kiefhaber. Intermediates can accelerate protein folding. *Proceedings of the National Academy of Sciences*, 96(12):6716–6721, 1999.

[68] Vladimir V Palyulin and Ralf Metzler. How a finite potential barrier decreases the mean first-passage time. *Journal of Statistical Mechanics: Theory and Experiment*, 2012(03):L03001, 2012.

[69] Jörg Kärger, Sergey Vasenkov, and Scott M Auerbach. Diffusion in zeolites. In *Handbook of zeolite science and technology*, pages 446–548. CRC Press, 2003.

[70] Marc Gershow and Jene Andrew Golovchenko. Recapturing and trapping single molecules with a solid-state nanopore. *Nature nanotechnology*, 2(12):775–779, 2007.

[71] Leonardo Dagdug, Jason Peña, and Ivan Pompa-García. Diffusion under confinement. *A Journey Through Counterintuition, Springer*, 2024.

[72] Vishwajeet Kumar, Arnab Pal, and Ohad Shpielberg. Arrhenius law for interacting diffusive systems. *Physical Review E*, 109(3):L032101, 2024.

[73] Tal Agranov and Baruch Meerson. Narrow escape of interacting diffusing particles. *Physical Review Letters*, 120(12):120601, 2018.

[74] Sanjib Sabhapandit and Satya N Majumdar. Freezing transition in the barrier crossing rate of a diffusing particle. *Physical Review Letters*, 125(20):200601, 2020.

[75] Alan J Bray, Satya N Majumdar, and Grégory Schehr. Persistence and first-passage properties in nonequilibrium systems. *Advances in Physics*, 62(3):225–361, 2013.

[76] Satya N Majumdar, Arnab Pal, and Grégory Schehr. Extreme value statistics of correlated random variables: a pedagogical review. *Physics Reports*, 840:1–32, 2020.

[77] Kirone Mallick. The exclusion process: A paradigm for non-equilibrium behaviour. *Physica A: Statistical Mechanics and its Applications*, 418:17–48, 2015.

[78] Jaeoh Shin, Alexander M Berezhkovskii, and Anatoly B Kolomeisky. Biased random walk in crowded environment: Breaking uphill/downhill symmetry of transition times. *The Journal of Physical Chemistry Letters*, 11(11):4530–4535, 2020.

[79] Cécile Appert-Rolland, Bernard Derrida, Vivien Lecomte, and Frédéric Van Wijland. Universal cumulants of the current in diffusive systems on a ring. *Physical Review E—Statistical, Nonlinear, and Soft Matter Physics*, 78(2):021122, 2008.

[80] Ohad Shpielberg, Takahiro Nemoto, and Joao Caetano. Universality in dynamical phase transitions of diffusive systems. *arXiv preprint arXiv:1807.01099*, 2018.

[81] Bernard Derrida and Tridib Sadhu. Large deviations conditioned on large deviations i: Markov chain and langevin equation. *Journal of Statistical Physics*, 176(4):773–805, 2019.

[82] Bernard Derrida and Tridib Sadhu. Large deviations conditioned on large deviations ii: Fluctuating hydrodynamics: B. derrida, t. sadhu. *Journal of Statistical Physics*, 177(1):151–182, 2019.

[83] Davide Gabrielli and PL Krapivsky. Gradient structure and transport coefficients for strong particles. *Journal of Statistical Mechanics: Theory and Experiment*, 2018(4):043212, 2018.

[84] Ohad Shpielberg, Yaroslav Don, and Eric Akkermans. Numerical study of continuous and discontinuous dynamical phase transitions for boundary-driven systems. *Physical Review E*, 95(3):032137, 2017.

[85] Herbert Spohn. *Large scale dynamics of interacting particles*. Springer Science & Business Media, 2012.

[86] Shlomi Reuveni, Iddo Eliazar, and Uri Yechiali. Asymmetric inclusion process as a showcase of complexity. *Physical review letters*, 109(2):020603, 2012.

[87] Ohad Shpielberg and Arnab Pal. Thermodynamic uncertainty relations for many-body systems with fast jump rates and large occupancies. *Physical Review E*, 104(6):064141, 2021.

[88] Yongjoo Baek, Yariv Kafri, and Vivien Lecomte. Extreme current fluctuations of boundary-driven systems in the large-n limit. *Journal of Statistical Mechanics: Theory and Experiment*, 2016(5):053203, 2016.

[89] Thierry Bodineau and Bernard Derrida. Current fluctuations in nonequilibrium diffusive systems: an additivity principle. *Physical review letters*, 92(18):180601, 2004.

[90] Ohad Shpielberg and Eric Akkermans. Le chatelier principle for out-of-equilibrium and boundary-driven systems: Application to dynamical phase transitions. *Physical review letters*, 116(24):240603, 2016.

[91] Ohad Shpielberg. Geometrical interpretation of dynamical phase transitions in boundary-driven systems. *Physical Review E*, 96(6):062108, 2017.

[92] Baruch Meerson, Arkady Vilenkin, and PL Krapivsky. Survival of a static target in a gas of diffusing particles with exclusion. *Physical Review E*, 90(2):022120, 2014.

[93] DW0129 Jepsen. Dynamics of a simple many-body system of hard rods. *Journal of Mathematical Physics*, 6(3):405–413, 1965.

[94] E Barkai and R Silbey. Diffusion of tagged particle in an exclusion process. *Physical Review E—Statistical, Nonlinear, and Soft Matter Physics*, 81(4):041129, 2010.

[95] Pavel L Krapivsky, Sidney Redner, and Eli Ben-Naim. *A kinetic view of statistical physics*. Cambridge University Press, 2010.

[96] Stefan Grosskinsky, Frank Redig, and Kiamars Vafayi. Condensation in the inclusion process and related models. *Journal of Statistical Physics*, 142(5):952–974, 2011.

[97] Stefan Grosskinsky, Frank Redig, and Kiamars Vafayi. Dynamics of condensation in the symmetric inclusion process. 2013.

[98] J Shepard Bryan, Prithviraj Basak, John Bechhoefer, and Steve Pressé. Inferring potential landscapes from noisy trajectories of particles within an optical feedback trap. *iscience*, 25(9), 2022.

[99] Olga K Dudko, Gerhard Hummer, and Attila Szabo. Intrinsic rates and activation free energies from single-molecule pulling experiments. *Physical review letters*, 96(10):108101, 2006.

[100] Masoud Abkenar, Thomas H Gray, and Alessio Zaccone. Dissociation rates from single-molecule pulling experiments under large thermal fluctuations or large applied force. *Physical Review E*, 95(4):042413, 2017.

[101] Jan Gieseler, Juan Ruben Gomez-Solano, Alessandro Magazzù, Isaac Pérez Castillo, Laura Pérez García, Marta Gironella-Torrent, Xavier Viader-Godoy, Felix Ritort, Giuseppe Pesce, Alejandro V Arzola, et al. Optical tweezers—from calibration to applications: a tutorial. *Advances in Optics and Photonics*, 13(1):74–241, 2021.

[102] Carlos Pérez-Espigares, Pedro L Garrido, and Pablo I Hurtado. Weak additivity principle for current statistics in d dimensions. *Physical Review E*, 93(4):040103, 2016.

[103] Eric Akkermans, Thierry Bodineau, Bernard Derrida, and Ohad Shpielberg. Universal current fluctuations in the symmetric exclusion process and other diffusive systems. *Europhysics Letters*, 103(2):20001, 2013.

[104] Thierry Bodineau and Bernard Derrida. Phase fluctuations in the abc model. *Journal of Statistical Physics*, 145(3):745–762, 2011.

[105] Vishwajeet Kumar, Arnab Pal, and Ohad Shpielberg. Emerging universality classes in thermally assisted activation of interacting diffusive systems: A perturbative hydrodynamic approach. *The Journal of Chemical Physics*, 160(13), 2024.

[106] Yariv Kafri, Erel Levine, David Mukamel, Gunter M Schütz, and J Török. Criterion for phase separation in one-dimensional driven systems. *Physical review letters*, 89(3):035702, 2002.

[107] James S Langer. Statistical theory of the decay of metastable states. *Annals of Physics*, 54(2):258–275, 1969.

[108] Claude Kipnis, Carlo Marchioro, and Errico Presutti. Heat flow in an exactly solvable model. *Journal of Statistical Physics*, 27(1):65–74, 1982.

[109] Chikashi Arita, PL Krapivsky, and Kirone Mallick. Generalized exclusion processes: Transport coefficients. *Physical Review E*, 90(5):052108, 2014.

[110] Vishwajeet Kumar, Arnab Pal, and Ohad Shpielberg. Inferring intermediate states by leveraging the many-body arrhenius law. *The Journal of Chemical Physics*, 163(22), 2025.

[111] Xin Li and Anatoly B Kolomeisky. Mechanisms and topology determination of complex chemical and biological network systems from first-passage theoretical approach. *The Journal of chemical physics*, 139(14), 2013.

[112] David J Wales. Dynamical signatures of multifunnel energy landscapes. *The Journal of Physical Chemistry Letters*, 13(27):6349–6358, 2022.

[113] KL Sebastian and Alok KR Paul. Kramers problem for a polymer in a double well. *Physical Review E*, 62(1):927, 2000.

[114] Tobias Linder, Bert L de Groot, and Anna Stary-Weinzinger. Probing the energy landscape of activation gating of the bacterial potassium channel kcsa. *PLOS Computational Biology*, 9(5):e1003058, 2013.

[115] Timo Schorlepp and Ohad Shpielberg. Systematic analysis of critical exponents in continuous dynamical phase transitions of weak noise theories. *Physical Review E*, 111(6):064113, 2025.

[116] Rick Bebon and Aljaž Godec. Controlling uncertainty of empirical first-passage times in the small-sample regime. *Physical Review Letters*, 131(23):237101, 2023.

[117] Cai Dieball, Yasamin Mohebi Satalsari, Angel B Zuccolotto-Bernez, Stefan U Egelhaaf, Manuel A Escobedo-Sánchez, and Aljaž Godec. Precisely controlled colloids: a playground for path-wise non-equilibrium physics. *Soft Matter*, 21(11):2170–2181, 2025.

[118] Christoph Zunke, Jörg Bewerunge, Florian Platten, Stefan U Egelhaaf, and Aljaž Godec. First-passage statistics of colloids on fractals: Theory and experimental realization. *Science advances*, 8(3):eabk0627, 2022.

[119] Benjamin Doyon, Gabriele Perfetto, Tomohiro Sasamoto, and Takato Yoshimura. Ballistic macroscopic fluctuation theory. *SciPost Physics*, 15(4):136, 2023.

[120] Cédric Bernardin and Raphaël Chetrite. Macroscopic fluctuation theory for ginzburg–landau dynamics with long-range interactions: C. bernardin, r. chetrite. *Journal of Statistical Physics*, 192(1):7, 2025.

[121] Rahul Dandekar, PL Krapivsky, and Kirone Mallick. Dynamical fluctuations in the riesz gas. *Physical Review E*, 107(4):044129, 2023.

[122] Saikat Santra, Jitendra Kethepalli, Sanaa Agarwal, Abhishek Dhar, Manas Kulkarni, and Anupam Kundu. Gap statistics for confined particles with power-law interactions. *Physical Review Letters*, 128(17):170603, 2022.

[123] David Hathcock and James P Sethna. Phase transitions beyond criticality: extending ising universal scaling functions to describe entire phases. *arXiv preprint arXiv:2402.18531*, 2024.

[124] Vishwajeet Kumar, Ohad Shpielberg, and Arnab Pal. Speeding up brownian escape via intermediate finite potential barriers. *Chaos: An Interdisciplinary Journal of Nonlinear Science*, 35(11), 2025.

[125] David G Grier and Yael Roichman. Holographic optical trapping. *Applied optics*, 45(5):880–887, 2006.

[126] Yael Roichman, Victor Wong, and David G Grier. Colloidal transport through optical tweezer arrays. *Physical Review E—Statistical, Nonlinear, and Soft Matter Physics*, 75(1):011407, 2007.

[127] Brandon R Ferrer and Juan Ruben Gomez-Solano. Experimental measurement of mean transition path velocities of colloidal particles surmounting energy barriers. *New Journal of Physics*, 26(12):123022, 2024.

[128] Mulugeta Bekele, G Ananthakrishna, and N Kumar. Optimal barrier subdivision for kramers' escape rate. *Pramana*, 46(6):403–410, 1996.

[129] Vladimir V Palyulin and Ralf Metzler. Speeding up the first-passage for subdiffusion by introducing a finite potential barrier. *Journal of Physics A: Mathematical and Theoretical*, 47(3):032002, 2014.

[130] Karol Capała, Amin Padash, Aleksei V Chechkin, Babak Shokri, Ralf Metzler, and Bartłomiej Dybiec. Lévy noise-driven escape from arctangent potential wells. *Chaos: An Interdisciplinary Journal of Nonlinear Science*, 30(12), 2020.

[131] Viktor Stojkoski, Trifce Sandev, Ljupco Kocarev, and Arnab Pal. Geometric brownian motion under stochastic resetting: A stationary yet nonergodic process. *Physical Review E*, 104(1):014121, 2021.

[132] Gourab Kumar Sar, Arnob Ray, Dibakar Ghosh, Chittaranjan Hens, and Arnab Pal. Resetting-mediated navigation of an active brownian searcher in a homogeneous topography. *Soft Matter*, 19(24):4502–4518, 2023.

[133] Siddharth Jain, Denis Boyer, Arnab Pal, and Leonardo Dagdug. Fick–jacobs description and first passage dynamics for diffusion in a channel under stochastic resetting. *The Journal of Chemical Physics*, 158(5), 2023.

[134] Murugappan Muthukumar. *Polymer translocation*. CRC press, 2016.

[135] Abhishek Dhar, Anupam Kundu, Satya N Majumdar, Sanjib Sabhapandit, and Grégory Schehr. Run-and-tumble particle in one-dimensional confining potentials: Steady-state, relaxation, and first-passage properties. *Physical Review E*, 99(3):032132, 2019.

[136] Mathis Guéneau, Satya N Majumdar, and Grégory Schehr. Run-and-tumble particle in one-dimensional potentials: mean first-passage time and applications. *Physical Review E*, 111(1):014144, 2025.

[137] Benjamin Walter, Gunnar Pruessner, and Guillaume Salbreux. First passage time distribution of active thermal particles in potentials. *Physical Review Research*, 3(1):013075, 2021.

[138] Arup Biswas, Johan LA Dubbeldam, Trifce Sandev, and Arnab Pal. A resetting particle embedded in a viscoelastic bath. *Chaos: An Interdisciplinary Journal of Nonlinear Science*, 35(3), 2025.

[139] Alexandre Rosas, Italo'Ivo Lima Dias Pinto, and Katja Lindenberg. Kramers' rate for systems with multiplicative noise. *Physical Review E*, 94(1):012101, 2016.

[140] Bernard Derrida. Lecture notes on large deviations in non-equilibrium diffusive systems. *SciPost Physics Lecture Notes*, page 106, 2025.

[141] Paul Cecil Martin, Eric D Siggia, and Harvey A Rose. Statistical dynamics of classical systems. *Physical Review A*, 8(1):423, 1973.

[142] Alex Kamenev. *Field theory of non-equilibrium systems*. Cambridge University Press, 2023.

[143] Alexander Altland and Ben D Simons. *Condensed matter field theory*. Cambridge university press, 2010.

[144] Lorenzo Bertini, Alberto De Sole, Davide Gabrielli, Gianni Jona-Lasinio, and Claudio Landim. Current fluctuations in stochastic lattice gases. *Physical review letters*, 94(3):030601, 2005.

[145] Eldad Bettelheim, Naftali R Smith, and Baruch Meerson. Inverse scattering method solves the problem of full statistics of nonstationary heat transfer in the kipnis-marchioro-presutti model. *Physical Review Letters*, 128(13):130602, 2022.

[146] Alberto Imparato, Vivien Lecomte, and Frédéric Van Wijland. Equilibriumlike fluctuations in some boundary-driven open diffusive systems. *Physical Review E—Statistical, Nonlinear, and Soft Matter Physics*, 80(1):011131, 2009.

[147] Pablo I Hurtado, Carlos P Espigares, Jesús J del Pozo, and Pedro L Garrido. Thermodynamics of currents in nonequilibrium diffusive systems: theory and simulation. *Journal of Statistical Physics*, 154(1):214–264, 2014.

[148] L Bertini, Alberto De Sole, D Gabrielli, Giovanni Jona-Lasinio, and C25485962009JSP Landim. Towards a nonequilibrium thermodynamics: a self-contained macroscopic description of driven diffusive systems. *Journal of Statistical Physics*, 135(5):857–872, 2009.

[149] Avi Aminov, Yariv Kafri, and Mehran Kardar. Fluctuation-induced forces in nonequilibrium diffusive dynamics. *Physical review letters*, 114(23):230602, 2015.

[150] PL Krapivsky, Kirone Mallick, and Tridib Sadhu. Large deviations in single file diffusion. *arXiv preprint arXiv:1405.1014*, 2014.

[151] Aurélien Grabsch, Pierre Rizkallah, and Olivier Bénichou. Joint distribution of currents in the symmetric exclusion process. *SciPost Physics*, 16(1):016, 2024.

[152] Ohad Shpielberg and Takahiro Nemoto. Imitating nonequilibrium steady states using time-varying equilibrium force in many-body diffusive systems. *Physical Review E*, 100(3):032104, 2019.

[153] Bernard Derrida, Benoît Douçot, and P-E Roche. Current fluctuations in the one-dimensional symmetric exclusion process with open boundaries. *Journal of Statistical physics*, 115(3):717–748, 2004.

[154] David Hartich and Aljaž Godec. Duality between relaxation and first passage in reversible markov dynamics: rugged energy landscapes disentangled. *New Journal of Physics*, 20(11):112002, 2018.

[155] David Hartich and Aljaž Godec. Interlacing relaxation and first-passage phenomena in reversible discrete and continuous space markovian dynamics. *Journal of Statistical Mechanics: Theory and Experiment*, 2019(2):024002, 2019.

[156] Gioia Carinci, Cristian Giardina, Claudio Giberti, and Frank Redig. Duality for stochastic models of transport. *Journal of Statistical Physics*, 152(4):657–697, 2013.

[157] Gunter M Schütz. Conditioned stochastic particle systems and integrable quantum spin systems. In *From Particle Systems to Partial Differential Equations II: Particle Systems and PDEs II, Braga, Portugal, December 2013*, pages 371–393. Springer, 2015.

[158] Erel Levine, David Mukamel, and GM Schütz. Zero-range process with open boundaries. *Journal of statistical physics*, 120(5):759–778, 2005.

Appendix A

The macroscopic fluctuation theory

A.1 Introduction

The macroscopic fluctuation theory (MFT) provides a hydrodynamic framework for characterizing fluctuations in interacting diffusive systems driven out of thermodynamic equilibrium. The theory is based on a coarse-grained description of the system, referred to as fluctuating hydrodynamics [85], in which the state of the system is described in terms of the local density and the associated particle currents. The microscopic stochastic dynamics are effectively encoded through fluctuating hydrodynamic equations that govern the evolution of these fields.

Building on the fluctuating hydrodynamics equation, the starting step in MFT consists of constructing a path-integral representation for the probability of observing a given history of the density and current fields, denoted by the trajectories $\{\rho(x,s), j(x,s)\}$. In the limit of large system size, the path integral is dominated by its saddle point, so that the evaluation of fluctuation probabilities reduces to a variational problem. The optimal fluctuation trajectory is therefore obtained by minimizing the associated action functional, which leads to the corresponding Euler–Lagrange equations.

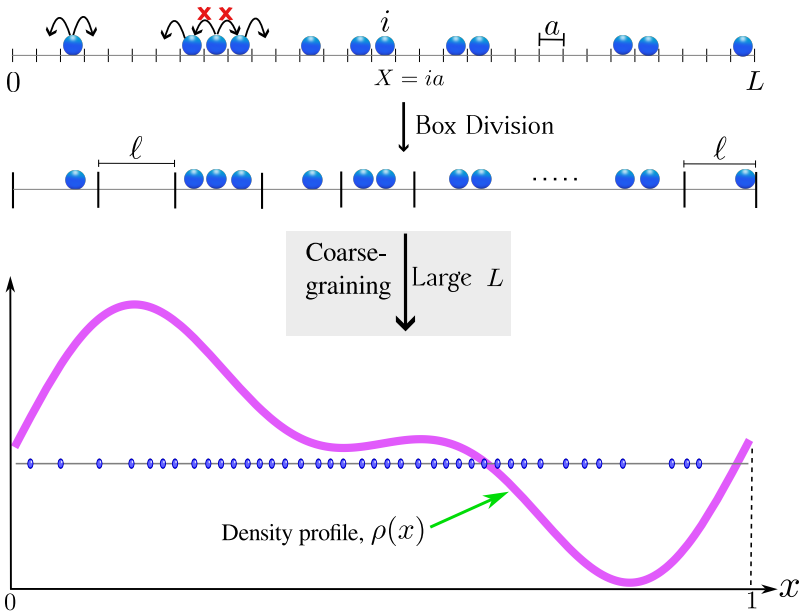

Figure A.1: The coarse-graining process: The top panel illustrates the microscopic dynamics of an exclusion process on a lattice. The middle panel depicts the process of division of the system into boxes of size ℓ, which is necessary to define the local density(see Eq. (A.1)). After coarse graining via diffusive rescaling, the system is described in terms of macroscopic density $\rho(x)$. The bottom panel shows a representative density profile.

In this chapter, we briefly discuss the coarse-graining description of interacting diffusive systems and subsequently state the fluctuating hydrodynamic equations that form the starting point for the formulation of macroscopic fluctuation theory.

A.2 Coarse-graining in diffusive systems, fluctuating hydrodynamics and the macroscopic fluctuation theory

To briefly explain the idea of coarse-graining, let us consider an example of an exclusion process on a lattice in 1-D as shown in top panel in FIG. A.1, where a is the lattice spacing. The particle diameter is considered to be smaller than the lattice spacing a, and thus its information becomes irrelevant upon coarse-graining. In other

words, the particle diameter does not influence the hydrodynamic description. The position of the i^{th} lattice is $X = ia$. We assume L to be large, so that a rescaled, dimensionless, continuous spatial coordinate $x = X/L$ could be introduced. Since the system is diffusive, we could also introduce a macroscopic time, $s = \tau/L^2$. The dimensions of other quantities transcend accordingly. (We note, however, that throughout the thesis we set $a = 1$ for simplicity, thereby rendering all quantities effectively dimensionless.) Following the review by Derrida [140], we can now define a macroscopic density. To this end, the system is partitioned into boxes of length ℓ (see middle panel of Fig. A.1) such that $a \ll \ell \ll L$. The local macroscopic density $\rho(x, \tau)$ is then defined as the total number of particles contained within a box of size ℓ, where the box begins at the lattice site with index $i = Lx/a$ and extends over a physical length ℓ, divided by ℓ. Mathematically,

$$\rho(x, s) = \frac{1}{\ell} \sum_{i=\frac{Lx}{a}}^{\frac{Lx}{a}+\frac{\ell}{a}-1} \eta_i(\tau = L^2 s), \tag{A.1}$$

where, η_i denotes the occupation variable at site i, which for models with excluded-volume for example take the value 1 if the site is occupied by a particle, and 0 if it is vacant. Note that the dimension of the density in Eq. (A.1) is $(\text{length})^{-1}$ (However, when $a = 1$, the density is effectively dimensionless). Further, since there is no sink or source of particle in the bulk, a continuity equation can be written in the bulk in terms of macroscopic density and current.

At the hydrodynamic (large L) limit, the dynamics of density $\rho(x, s)$ and current density $j(x, s)$ (of any interacting-diffusive systems) are encapsulated in the fluctuating hydrodynamics equations (restricted here to one-dimension and a single particle

species for brevity)

$$\partial_s \rho = -\partial_x j \tag{A.2a}$$

$$j = J(\rho) + \sqrt{2D_0\chi/L}\,\xi(x,s), \tag{A.2b}$$

$$J(\rho) = -D(\rho)\partial_x\rho - \chi(\rho)\beta\partial_x U. \tag{A.2c}$$

where, $D_0 = 1/\beta = k_B T$. $D(\rho)$ and $\chi(\rho)$ are the density-dependent diffusivity and mobility which encapsulate the diffusive dynamics. In other words, all the interparticle interactions of the dynamics of diffusive systems are captured in D and χ. Further, these quantities are not entirely independent; they are related via Einstein's equation [8]

$$D(\rho) = \chi(\rho) f''(\rho). \tag{A.3}$$

In Eq. (A.3), $\beta = 1/k_B T$ has been assumed to be unity and $f(\rho)$ is the equilibrium free energy density. In Eq. (A.2) $x \in [0,1]$ and $s \in [0,t]$ are diffusively rescaled. Eq. (A.2a) is the continuity equation for the bulk, which takes care of the fact that particles can leave the system only through the boundaries. Eq. (A.2b) describes the current density using a Langevin equation [1], where the deterministic part is given by Fick's law of the current J. The Fick's law current in (A.2c) depends on the diffusivity D and mobility χ, which are typically local functions of the density. Fick's law implies that the current stems both from a density gradient and from an external forcing due to the potential gradient $\partial_x U$. See Fig A.2. Importantly, D, χ are experimentally measurable. The noise term in (A.2b) is weak as we consider a large system size L. $\xi(x,s)$ is a white noise term in both x and s, satisfying

$$\langle \xi(x,s)\xi(x',s')\rangle = \delta(x-x')\delta(s-s'). \tag{A.4}$$

[1] The Langevin equation has a weak noise, and therefore, time discretization questions are immaterial.

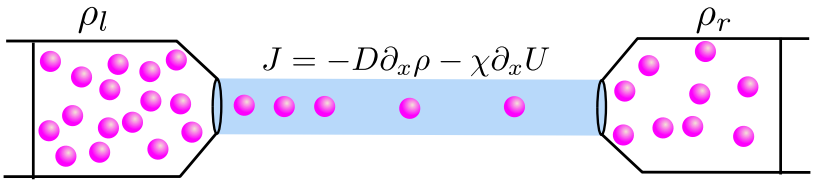

Figure A.2: Fick's law for a one dimensional boundary driven system. The boundaries are coupled to particle reservoirs at densities ρ_l, ρ_r correspondingly.

The noise strength in Eq. (A.2b) is found to depend on the mobility χ in order to satisfy the Gallavotti-Cohen fluctuation relations [11].

The starting point of the macroscopic fluctuation theory (MFT) is to write the probability weight for observing a trajectory $\{\rho, j\}$ during the time window $[0, t]$. Employing the Martin-Siggia-Rose formalism [141–143], this probability is given by the following relation

$$\text{Prob}\left[\{\rho, j\}\right] \asymp \exp\left[-\frac{L}{D_0}\int_0^t ds \int_0^1 dx \, \frac{\left(j - J(\rho)\right)^2}{4\chi}\right]\delta(\partial_s\rho + \partial_x j) \qquad \text{(A.5)}$$

where $\asymp$ indicates possible possible logarithmic corrections. The delta functional enforces the local conservation law, implying that the density and current fields are not entirely independent; they must satisfy the continuity equation.

The MFT is a coarse grained theory, and hence, large systems are assumed. The fundamental formula [Eq. (A.5)] reveals that calculations are dominated by the saddle point due to the large L limit we consider. Hence the problem converts into a variational problem. This fact helped facilitating a large number of results within the MFT framework, from calculations of full counting statistics [47, 103, 144–147], non-equilibrium correlations [148], first passage problems [73, 92], and more [149–152].

Appendix B

The additivity principle

One of the central problems in non-equilibrium statistical physics is to understand the fluctuations of currents in systems maintained out of equilibrium by boundary driving. A paradigmatic setup consists of a one-dimensional diffusive system connected at its boundaries to two reservoirs imposing different densities or temperatures. In such situations, the system reaches a non-equilibrium steady state (NESS) characterized by a non-zero average current.

A natural approach to understand the properties of such a system is to focus on macroscopic observables such as the time-integrated current. For a system of size L, let Y_t denote the integrated current over a long time t. The probability of observing such an integrated current assumes the following large deviation form [89]:

$$P_L\Big(q = \frac{Y_t}{t}, \rho_l, \rho_r\Big) \sim e^{-t\mathcal{I}_L(q,\rho_l,\rho_r)} \tag{B.1}$$

where ρ_l and ρ_r denotes the density of the left and the right reservoir respectively. $\mathcal{I}_L(q, \rho_l, \rho_r)$ denotes the large deviation function (LDF) which depends on L, q, ρ_l and ρ_r. Moreover, the LDF also depends on coupling between reservoirs and the system [89]. However, for notational simplicity, this dependence is not made explicit in Eq. (B.1).

However, determining $\mathcal{I}_L(q, \rho_l, \rho_r)$ remains, in general, a highly non-trivial problem. In particular, within most theoretical approaches, the computation of current cumulants becomes progressively more difficult with increasing order, rendering a direct characterization of the full distribution intractable. In this context, Bodineau and Derrida [89] introduced the additivity principle, which provides a simple yet powerful framework to compute the large deviation function, and thereby the full statistics of current fluctuations. By postulating this principle, they showed that the full statistics of current fluctuations can be expressed in terms of the first two cumulants.

The additivity principle [89] provides a remarkably simple way to compute current fluctuations in diffusive systems. The central idea of the additivity principle is to relate the probability of sustaining a given current in a large system to the probabilities of sustaining the same current in smaller subsystems. More precisely, consider a system of size L connected to two reservoirs at densities ρ_l and ρ_r. The probability of observing an integrated current q in the system at large times is given by Eq. (B.1). Now, suppose the system is divided into two subsystems of lengths $L - L'$ and L'. Bodineau and Derrida then assumed that for large system size L and the current q is of the order $1/L$, the large deviation function obeys the additivity principle given as

$$\mathcal{I}_L(q, \rho_l, \rho_r) = \min_{\rho}[\mathcal{I}_{L-L'}(q, \rho_l, \rho) + \mathcal{I}_{L'}(q, \rho, \rho_r)]. \tag{B.2}$$

The above property, (Eq. (B.2)), immediately implies the following relation for the probability

$$P_L(q, \rho_l, \rho_r, t) = \max_{\rho}\Big[P_{L-L'}(q, \rho_l, \rho, t)\, P_{L'}(q, \rho, \rho_r, t)\Big]. \tag{B.3}$$

It is clear from Eq. (B.3) that the two subsystems behave effectively independently,

except for the constraint imposed at their interface, where the intermediate density ρ is selected so as to maximize the overall probability.

They [89] then introduced the scaling hypothesis $\mathcal{I}_L(q, \rho_l, \rho_r) = L^{-1}G(Lq, \rho_l, \rho_r)$ and proceeded by iteratively decomposing the system of size L into smaller and smaller subsystems. If each subsystem is very small, the density difference at the two ends of the subsystem would be very small. This implies that for small currents q of the order of L^{-1}, each subsystem is approximately in equilibrium. This then implies that the current will exhibit Gaussian fluctuation, around its mean value determined by Fick's law [153]. In the continuum limit, one then obtains the following expression of the function G [89]

$$G(q) = \min_{\rho(x)} \int_0^1 \frac{[q + D(\rho)\partial_x \rho(x)]^2}{4\chi(\rho(x))} dx \tag{B.4}$$

where, $D(\rho)$ is the diffusivity and $\chi(\rho)$ is the mobility. So, the determination of $G(q)$ and therefore of the current LDF $\mathcal{I}_L$ reduces to a simple static variational problem. Specifically, the minimization over $\rho(x)$ leads to the Euler-Lagrange equation which must be supplemented by the boundary conditions, $\rho(x = 0) = \rho_l$ and $\rho(x = 1) = \rho_r$ in order to determine the optimal density profile $\rho(x)$. This optimal density profile can then be used in Eq. (B.4) to determine G and hence the LDF $\mathcal{I}_L$.

After determining the function G, the computation of the current cumulants follows in a standard manner via the scaled cumulant generating function. We define $\psi(\lambda)$ as

$$\psi(\lambda) \equiv \lim_{t\to\infty} \frac{1}{t} \ln\langle e^{\lambda Y_t}\rangle. \tag{B.5}$$

The function $\psi(\lambda)$ is obtained from G through a Legendre transform. Using the

scaling relation $\mathcal{I}_L(q) = L^{-1}G(Lq)$, one obtains

$$\psi(\lambda) = \frac{1}{L}\max_q \left[\lambda q - G(q, \rho_l, \rho_r)\right]. \tag{B.6}$$

Once $\psi(\lambda)$ is known, the cumulants of the integrated current can be obtained by successive derivatives with respect to λ. In particular, the n-th cumulant per unit time is given by

$$\frac{\langle Y_t^n \rangle_c}{t} = \left.\frac{d^n \psi(\lambda)}{d\lambda^n}\right|_{\lambda=0}. \tag{B.7}$$

Thus, the knowledge of $\psi(\lambda)$, and hence of G, allows one to determine all current cumulants in a systematic manner.

Appendix C

Appendix for Chapter 2

C.1 The survival probability of an overdamped particle

The purpose of this section is to show that the survival probability for a single particle can be inferred from the ground state energy of the Fokker-Planck Hamiltonian $\hat{H}_{FP}$.

Let $P(x,t)$ be the probability density of an over-damped particle. Given an initial probability distribution, the evolution of the probability density is given by the Fokker-Planck equation

$$\partial_t P = D_0 \partial_{xx} P + \partial_x (P \partial_x U), \tag{C.1}$$

where $U(x)$ is the potential, $D_0 = k_B T$ and we have set the friction coefficient to 1. We consider the potential trap in $x = [0, L]$ with reflecting boundary conditions at $x = 0$ corresponding to the center of the potential trap

$$D_0 \partial_x P + P \partial_x U|_{x=0} = 0, \tag{C.2}$$

and absorbing boundary conditions at $x = L$ corresponding to the peak of the potential trap

$$P|_{x=L} = 0. \tag{C.3}$$

The survival probability – the probability that the particle has not been absorbed upto time t – is given by

$$\mathcal{S}(t) = \int_0^L dx\, P(x,t). \tag{C.4}$$

with $\mathcal{S}(t=0) = 1$ and $\mathcal{S}(t \to \infty) = 0$. At large times, significantly larger than the diffusive time L^2/D_0, the survival probability is expected to follow a large deviation form $\mathcal{S}(t) \asymp \mathrm{e}^{-\Phi t}$, where we recall that Φ is the escape rate, given by the AL. Here, $\asymp$ implies $\Phi = -\lim_{t\to\infty} \frac{1}{t} \log \mathcal{S}(t)$. While we focus here on the long time statistics of the survival probability, we note that the short time statistics contain useful information [33].

An explicit solution for the survival probability in the presence of an arbitrary potential $U(x)$ does not exist. However, several methods exist to capture the large time behavior. One such way is to convert the Fokker-Planck equation into an imaginary-time Schrödinger equation [20]. This can be done by considering the transformation $P(x,t) = \mathrm{e}^{-U(x)/2D_0}\psi(x,t)$ such that $\psi(x,t)$ satisfies the imaginary time Schrödinger equation. Namely

$$\begin{aligned} -\partial_t \psi &= \hat{H}_{FP}\psi, \\ \hat{H}_{FP}/D_0 &= -\partial_{xx} + \frac{1}{4}\left(\frac{\partial_x U}{D_0}\right)^2 - \frac{\partial_{xx}U}{2D_0}. \end{aligned} \tag{C.5}$$

Quantum-mechanically, the presence of reflecting and absorbing boundaries implies that the particle is bounded. This in turn implies that the energy spectrum of the

system would be discrete [1]. Hence, we can now write,

$$\psi(x,t) = \sum_n C_n \phi_n(x) e^{-E_n t}, \tag{C.6}$$

where, E_n is the n-th eigenvalue of the Hamiltonian $\hat{H}_{FP}$ in Eq.(C.5), ϕ_n are the corresponding eigenfunctions, and C_n are coefficients determined by the initial conditions.

The transformation to the quantum problem is useful when considering the large time limit as it is easy to see that $\psi \sim \mathrm{e}^{-\mathrm{E_0 t}}$, where E_0 is the ground state energy of $\hat{H}_{FP}$. Translating the same to the survival probability [Eq.(C.4)], one should have, in the large time limit,

$$\mathcal{S}(t) \asymp \mathrm{e}^{-\mathrm{tE_0}}, \tag{C.7}$$

which allows us to identify $E_0 = \Phi$. Moreover, we notice that initial conditions hardly effect the long time behaviour [2]. The argument can be extended to M *non-interacting particles* such that

$$\mathcal{S}(t) \asymp \mathrm{e}^{-\mathrm{tME_0}}, \tag{C.8}$$

from which one can identify that $\Phi = ME_0$ for M non-interacting particles, where E_0 is the ground state energy of the single particle Hamiltonian $\hat{H}_{FP}$ [3]. Here, it is important to stress that we will consider the limit of large M, L, but a fixed density $\overline{\rho}_0 = M/L$ and then take the large $\Delta U/D_0$ limit. Under these conditions, the activation of a single particle remains exponentially rare. Conversely, if one

[1] We assume here that U is smooth and bounded.

[2] With the obvious exception that the initial condition $\psi(x, t = 0)$ is almost completely orthogonal to the ground state. Or physically, the particle starts close to the absorbing boundary.

[3] To be precise, it is possible that for a large enough M, Φ shows discrepancies from the mean escape time [154, 155]. Nevertheless, here we will consider $M, L \to \infty$ but the density is kept constant. In this limit, the non-interacting case typically implies $\Phi \sim \rho \frac{\Delta U}{D_0} \mathrm{e}^{-\frac{\Delta \mathrm{U}}{\mathrm{D_0}}}$

fixes the trap size and the energy barrier, while increasing the number of particles, the typical activation times need not be long anymore and Φ will typically not be associated with the escape rate [154, 155].

C.2 The SSEP survival probability with a linear potential

The purpose of this section is to present in full the derivation of the survival probability of SSEP particles subjected to the linear potential $\tilde{U}(x) = \Delta\tilde{U}x$. Let us first recall that for the SSEP, $D = 1, \chi = \rho(1-\rho)$. The F-transformation (2.7) implies $\rho = \sin^2 F$. Thus, the corresponding Euler-Lagrange equation (2.8) and the boundary conditions (2.9) in the presence of the linear potential are respectively given by

$$\begin{aligned} -\partial_{xx}F + \frac{\Delta\tilde{U}^2}{16}\sin 4F &= \frac{1}{2}\Lambda \sin 2F \\ \partial_x F + \frac{\Delta\tilde{U}}{4}\sin 2F|_{x=0} &= F|_{x=1} = 0, \end{aligned} \tag{C.9}$$

where we take $F \in [0, \pi/2]$ to keep $\chi^{1/2}$ non-negative.

Eq. (C.9) is an autonomous equation and can thus be simplified by setting $v = \partial_x F$. Then, $\partial_{xx}F = v\frac{dv}{dF}$. Now, v and F can be integrated independently in Eq. (C.9) leading to

$$v^2 = \Lambda \cos 2F - \frac{1}{32}\Delta\tilde{U}\cos 4F + H_0, \tag{C.10}$$

where H_0 is a constant of integration. Using the boundary conditions, and making the transformation $y = \cos 2F$ leads to the derivation of Eq. (2.12), where we have assumed that the slope of $y(x)$ is monotonously increasing due to the monotonicity of the potential. To find $\Delta\tilde{U}$, we merely integrate Eq. (2.12) with respect to x and

y independently at the limit $x \in [0,1]$ and correspondingly $y \in [y_0, 1]$. This leads to $C_0 = \Delta\tilde{U}/2$ (see the definition of C_k in Eq. (2.13)). For the density, we recall that

$$\overline{\rho}_0 = \int dx \rho(x) = \int dx \sin^2 F. \tag{C.11}$$

Using the y transformation as well as Eq. (2.12), we find $\overline{\rho}_0 = \frac{1}{2}(1 - \frac{C_1}{C_0})$ or $\Delta\tilde{U}\overline{\rho}_0 = C_0 - C_1$. Finally, using the relation between C_0 and C_1 to $\overline{\rho}_0, \Delta\tilde{U}$, we can express

$$\begin{aligned}
\frac{\Phi_{\rm SSEP}}{D_0 L} &= \int dx \, (\partial_x F + \frac{\Delta\tilde{U}}{4} \sin 2F)^2 && \text{(C.12)} \\
&= \int dx \, (\frac{\partial_x y}{2\sqrt{1-y^2}} - \frac{\Delta\tilde{U}}{4}\sqrt{1-y^2})^2 && \text{(C.13)} \\
&= \frac{1}{4}\Delta\tilde{U}(y_0 - 1) + \int dx \, \frac{(dy/dx)^2}{4(1-y^2)} + \frac{\Delta\tilde{U}^2}{16}(1-y^2) \\
&= \frac{C_0}{2}(y_0 - 1 + C_0 - C_2 + 4\lambda(C_1 - y_0 C_0)),
\end{aligned}$$

where we have used Eqs. (2.10) and (2.11). In order to evaluate $\Phi_{\rm SSEP}$ as a function of $\Delta\tilde{U}$ and $\overline{\rho}_0$, it is now necessary to evaluate the C_k integrals [Eq. (2.13)]. We consider two limiting cases.

C.2.1 The low density limit

In the limit $1 - y_0 \ll \lambda \ll 1$, we find the small density limit with at $\Delta\tilde{U} \gg 1$. This can be easily inferred since $y_0 \to 1$ implies that the highest density point in the regime is small. The integrals can then be approximated

$$\begin{aligned}
C_0 &= -\frac{1}{2}\lambda(1 + \log\lambda) && \text{(C.14)} \\
C_0 - C_1 &= \frac{1}{2}\delta y(1 + 4\lambda + 2\lambda\log\lambda) \\
C_0 - C_2 &= \delta y(1 + 4\lambda + 2\lambda).
\end{aligned}$$

Using the C_k values in Eq. (C.12) allows to evaluate $\Phi_{\rm SSEP}$ to leading order. We find as expected the AL

$$\frac{\Phi_{\rm SSEP}}{D_0 L} = \Delta\tilde{U}^2 \overline{\rho}_0 \mathrm{e}^{-\Delta\tilde{\mathrm{U}}}. \tag{C.15}$$

We note that to leading order, one can infer from the $C_0 - C_1$ calculation that $\delta y = 2\Delta\tilde{U}\overline{\rho}_0$. The C_0 leading order in Eq. (C.14) suggests $\lambda = \mathrm{e}^{-\Delta\tilde{\mathrm{U}}}$.

C.2.2 The finite density limit

The finite density limit arises in the limit of $\delta y = 1 + y_0 \ll \lambda \ll 1$, where we expect our results to be valid. Note that taking the limits in the opposite order leads to diverging integrals. Evaluating the C_k integrals, we find

$$\begin{aligned} C_0 &= \frac{1}{2}\log(\frac{2}{\lambda\delta y}) + \lambda(3 - \log(\frac{2}{\lambda\delta y})) - \lambda\delta y(2 + \log\frac{\lambda\delta y}{2}), \\ C_1 &= \frac{1}{2}\log\frac{\delta y}{2\lambda} - \lambda\log\frac{\lambda\delta y}{2} - \lambda \\ C_2 &= \delta y - 2 - \frac{1}{2}\log\frac{\delta y\lambda}{2} + \lambda\log\frac{\delta y}{2\lambda^3} - \lambda + \lambda\delta y\log\frac{\delta y\lambda}{2}. \end{aligned} \tag{C.16}$$

To leading order, the relations $C_0 = \Delta\tilde{U}/2$ and $C_0 - C_1 = \Delta\tilde{U}\overline{\rho}_0$ allow to infer $\delta y = \mathrm{e}^{-\Delta\tilde{\mathrm{U}}\overline{\rho}_0}$ and $\lambda = 2\mathrm{e}^{-\Delta\tilde{\mathrm{U}}(1-\overline{\rho}_0)}$. One expects $\Phi_{\rm SSEP}$ to have the form of a vanishing series expansion in $\lambda, \delta y \to 0$. This implies that the expected leading order is $\Phi_{\rm SSEP} \propto \lambda + O(\delta y, \lambda^2, \delta y^2, \lambda\delta y)$. This leads to the announced result $\Phi_{\rm SSEP} \propto \mathrm{e}^{-\Delta\tilde{\mathrm{U}}(1-\overline{\rho}_0)}$. An exact leading order calculation following Eq. (C.12) then suggests

$$\frac{\Phi_{\rm SSEP}}{D_0 L} = 2\Delta\tilde{U}\mathrm{e}^{-\Delta\tilde{\mathrm{U}}(1-\overline{\rho}_0)}. \tag{C.17}$$

Eq. (C.17) expands on Eq. (2.14) of the main text, as the pre-exponential polynomial function A is now explicit. Notice that the vanishing density limit cannot be obtained from this result as we have assumed $\delta y \to 0$, i.e. $y_0 \to -1$.

C.3 The SIP survival probability with a linear potential

The purpose of this section is to provide the detailed calculation of Φ for the SIP with the linear potential $\tilde{U}(x) = \Delta\tilde{U}x$. Let us first recall that for the SIP, $D = 1, \chi = \rho(1+\rho)$. The F-transformation (2.7) implies $\rho = \sinh^2 F$. Thus, the corresponding Euler-Lagrange equation (2.8) and the boundary conditions (2.9) in the presence of the linear potential are respectively given by

$$\begin{aligned} -\partial_{xx}F + \frac{\Delta\tilde{U}^2}{16}\sinh 4F &= \frac{1}{2}\Lambda \sinh 2F \\ \partial_x F + \frac{\Delta\tilde{U}}{4}\sinh 2F|_{x=0} &= F|_{x=1} = 0, \end{aligned} \tag{C.18}$$

where we take $F \in [0, \infty)$ to to avoid duplicity.

Eq. (C.18) is an autonomous equation and like the SSEP case, it can be simplified by setting $v = \partial_x F$. Then, $\partial_{xx}F = \frac{dv}{dF}v$. Now, v and F can be integrated independently in Eq. (C.18) leading to

$$v^2 = \Lambda \cosh 2F - \frac{1}{32}\Delta\tilde{U}\cosh 4F + H_0, \tag{C.19}$$

where H_0 is a constant of integration. Using the boundary conditions and making the transformation $y = \cos 2F$, we find

$$\frac{dy}{dx} = -\frac{1}{2}\Delta\tilde{U}\sqrt{y^2-1}\sqrt{y^2 - 1 + 8\lambda(y_0 - y)}. \tag{C.20}$$

Here, $y_0 = y(x = 0)$ and where we have assumed that the slope of $y(x)$ is monotonously decreasing due to the monotonicity of the potential. At this point,

we again define the C_k-integral for this case

$$C_k = \int_1^{y_0} \frac{y^k dy}{\sqrt{y^2-1}\sqrt{y^2-1+8\lambda(y_0-y)}} \tag{C.21}$$

for $1 \leq y_0 < \infty$. To find $\Delta\tilde{U}$, we merely integrate Eq. (C.20) with respect to x and y independently at the limit $x \in [0,1]$ and correspondingly $y \in [1, y_0]$. This leads to $C_0 = \Delta\tilde{U}/2$. For the density, we recall that

$$\overline{\rho}_0 = \int dx \rho(x) = \int dx \sinh^2 F. \tag{C.22}$$

Using the y transformation as well as Eq. (C.20), we find $\overline{\rho}_0 = \frac{1}{2}(\frac{C_1}{C_0} - 1)$ or similarly $\Delta\tilde{U}\overline{\rho}_0 = C_1 - C_0$.

Finally, using the relation between C_0 and C_1 to $\overline{\rho}_0, \Delta\tilde{U}$, we can express Φ_{SIP}

$$\begin{aligned}
\frac{\Phi_{\text{SIP}}}{D_0 L} &= \int dx \, (\partial_x F + \frac{\Delta\tilde{U}}{4} \sinh 2F)^2 && \text{(C.23)} \\
&= \int dx \, (\frac{\partial_x y}{2\sqrt{y^2-1}} + \frac{\Delta\tilde{U}}{4}\sqrt{y^2-1})^2 && \text{(C.24)} \\
&= -\frac{1}{4}\Delta\tilde{U}(y_0-1) + \int dx \, \frac{(dy/dx)^2}{4(y^2-1)} + \frac{\Delta\tilde{U}^2}{16}(y^2-1) \\
&= \frac{C_0}{2}(1 - y_0 + C_2 - C_0 + 4\lambda(y_0 C_0 - C_1)).
\end{aligned}$$

In order to evaluate Φ_{SIP} as a function of $\Delta\tilde{U}$ and $\overline{\rho}_0$, it is necessary to evaluate the C_k-integrals. We consider two limiting cases.

C.3.1 The low density limit

In the limit $\delta y = y_0 - 1 \ll \lambda \ll 1$, we find the small density limit as well as $\Delta\tilde{U} \gg 1$. This can be easily inferred since $y_0 \to 1$ implies that the highest density point in

the regime is small. The integrals can then be approximated

$$\begin{aligned} C_0 &= -\frac{1}{2}\log\lambda - \lambda(1+\log\lambda) \\ C_1 - C_0 &= \frac{1}{2}\delta y + \delta y\lambda(2+\log\lambda) \\ C_2 - C_0 &= \delta y + 2\delta y\lambda(2+\log\lambda). \end{aligned} \tag{C.25}$$

Using the evaluated C_k integrals allows to evaluate $\Phi_{\rm SIP}$ to leading order. We find as expected the AL

$$\frac{\Phi_{\rm SIP}}{D_0 L} = \Delta\tilde{U}^2\overline{\rho}_0 \mathrm{e}^{-\Delta\tilde{\mathrm{U}}}. \tag{C.26}$$

We note that to leading order, one can infer from the $C_1 - C_0$ calculation that $\delta y = 2\Delta\tilde{U}\overline{\rho}_0$. From the C_0 evaluation, we infer $\lambda = \mathrm{e}^{-\Delta\tilde{\mathrm{U}}}$.

C.3.2 The finite density limit

For the finite density limit and for $\Delta\tilde{U} \gg 1$, we consider the limits $\lambda \ll \mu = y_0\lambda \ll 1$. In these limits, evaluation of the C_k integrals leads to

$$\begin{aligned} C_0 &= \frac{1}{2}\log 2/\mu + O(\lambda/\mu, \mu\log\mu). \\ C_1 - C_0 &= -\log\frac{2\lambda}{\mu} + (2+\log\frac{\mu}{2})\mu + \frac{\lambda}{\mu} + O(\lambda) \\ C_2 - C_0 &= \mu/\lambda - 1 + 2\mu(1+\log\frac{\mu}{2}) + 2\lambda\log\frac{\mu}{2\lambda^2} + O(\lambda). \end{aligned} \tag{C.27}$$

The leading order results imply $\mu = 2\mathrm{e}^{-\Delta\tilde{\mathrm{U}}}$ and $\lambda = \mathrm{e}^{-\Delta\tilde{\mathrm{U}}(1+\overline{\rho}_0)}$. One expects $\Phi_{\rm SIP}$ to have the form of a vanishing series expansion in $\lambda, \mu \to 0$. This implies that the expected leading order is $\Phi_{\rm SSEP} \propto \mu + O(\lambda)$, confirming the announced result $\Phi_{\rm SIP} \propto \mathrm{e}^{-\Delta\tilde{\mathrm{U}}}$. An exact leading order calculation yields

$$\frac{\Phi_{\rm SIP}}{D_0 L} = \Delta\tilde{U}\mathrm{e}^{-\Delta\tilde{\mathrm{U}}}. \tag{C.28}$$

Eq. (C.28) expands on Eq. (2.17) of the main text, as the pre-exponential polynomial function A is now explicit.

C.4 The ground state energy and non-interacting particles

In this section, we give an alternative derivation of the long-time survival probability of non-interacting particles than the one presented in Sec. C.1. Starting from an arbitrary diffusive process of interacting particles, captured by D and χ, the MFT suggests that the inverse mean escape time is recast by the following minimization problem

$$\begin{aligned} \frac{\Phi}{D_0 L} &= \min_F \int dx\, J_F^2 - \Lambda(\rho(F) - \overline{\rho}_0) \\ J_F &= \partial_x F + \frac{1}{2}\chi^{1/2}\partial_x \tilde{U}, \end{aligned} \tag{C.29}$$

with the boundary conditions in Eq. (2.9). The corresponding Euler-Lagrange equation is given by Eq. (2.8) and Φ is then given by Eq. (2.11). Integrating by parts, we find the two identities

$$\begin{aligned} \int dx\, (\partial_x F)^2 &= F\partial_x F|_{x=0}^{x=1} - \int dx\, F\partial_{xx} F \\ \int dx\, \partial_x F \partial_x \tilde{U}\chi^{1/2} &= F\partial_x \tilde{U}\chi^{1/2}|_{x=0}^{x=1} - \int dx\, F(\frac{\chi'}{2\chi^{1/2}}\partial_x F\partial_x \tilde{U} + \chi^{1/2}\partial_{xx}\tilde{U}). \end{aligned} \tag{C.30}$$

Using the two identities above and substituting them in Eq. (2.11), we find

$$\begin{aligned} \frac{\Phi}{D_0 L} &= \int dx\, (\partial_x F + \frac{1}{2}\chi^{1/2}\partial_x \tilde{U})^2 \\ &= F J_F|_{x=0}^{x=1} + \int dx\, F(-\partial_{xx}F - \frac{1}{2}\chi^{1/2}\partial_{xx}\tilde{U}) \\ &\quad + \int dx\, (\chi - F\chi'/2)\frac{\partial_x F\partial_x \tilde{U}}{2\chi^{1/2}} + \frac{1}{4}\chi(\partial_x \tilde{U})^2, \end{aligned} \tag{C.31}$$

Notice that $FJ_F = 0$ at the two boundaries $x = 0, 1$ according to the boundary conditions. Furthermore, using the Euler-Lagrange equation, we find

$$\frac{\Phi}{D_0 L} = \frac{1}{2}\Lambda \int dx\, F \frac{\delta\rho[F]}{\delta F} + \int dx\, \frac{\partial_x \tilde{U}}{2\chi^{1/2}}(\chi - \chi' F/2) J_F, \tag{C.32}$$

where $\frac{\delta\rho[F]}{\delta F} = 2\chi^{1/2}/D$.

For non-interacting particles, $D = 1$, $\rho = F^2$ and consequently $\chi = F^2$. Therefore, $\chi - \chi' F/2$ vanishes and $\Phi_{\mathrm{NI}} = D_0 L \overline{\rho}_0 \Lambda = D_0 M \Lambda$ is obtained. Moreover, the Euler-Lagrange equation in this case becomes the eigenvalue problem $\hat{H}_{FP} F = D_0 \Lambda F$, where $\hat{H}_{FP}$ is given by Eq. (C.5) with the appropriate boundary conditions. Therefore, ΛD_0 is an eigenvalue of the Fokker-Planck Hamiltonian. The minimization problem dictates that we choose the lowest eigenvalue, i.e. $D_0\Lambda$ is the ground state energy of the Fokker-Planck Hamiltonian. This implies that $D_0\Lambda = E_0$ and hence $\Phi_{\mathrm{NI}} = M E_0$.

Recall that for the SSEP and SIP, we have an exact solution for the linear potential. In this case we have assumed a fixed Λ as well as $F|_{x=0}$ and inferred the corresponding $\overline{\rho}_0, \Delta\tilde{U}$. So, there is no ambiguity on which eigenvalue to use. Numerically, for the linear potential as well as for the other tested potentials, there exists more than one eigenvalue. Furthermore, numerical investigations suggest that Φ is minimized at the lowest eigenvalue Λ of the Euler-Lagrange equation. A proof that Λ should always be the ground state energy is still lacking, and will be pursued elsewhere.

C.5 Numerical procedure (the shooting method)

Fig. 2.2 of the main text employs a shooting method to obtain the g values for the SSEP and the SIP subjected to different potentials. In this section, we describe in

detail this shooting method algorithm and discuss the sources of numerical errors.

For any given process, finding the survival probability amounts to finding the optimal fluctuation that minimizes Φ. In practice, this reduces to solving the Euler-Lagrange equation (2.8) of the main text, subjected to the boundary conditions $F|_{x=1} = J_F|_{x=0} = 0$. For a general process, or even for a given process with a general potential U, it is unlikely to recover an analytic solution for Eq. (2.8). To that end, we introduce a numerical solution.

The difficulty of solving the Euler-Lagrange Eq. (2.8) does not arise from the non-linearity of the equation. First, the reflecting boundary condition allows multiple solutions to the equation. Furthermore, Eq. (2.8) is a (non-linear) eigenvalue problem, leading to a set of Λ eigenvalues. Consequently, a naive numerical protocol will always yield the trivial $F = 0$ solution, in which, the mean density constraint is not immediately enforced.

To overcome these problems, consider the following. Rather than fixing $\overline{\rho}_0, \Delta\tilde{U}$ and searching for $\Lambda, F|_{x=0}$ that solve Eq. (2.8), we fix a value $F|_{x=0} = f_0$. We then solve the Euler-Lagrange equation, Eq. (2.8), for a set of values $\Lambda \in [0, \Lambda_{\max}]$. Within this range, we identify the eigen-functions F as solutions that satisfy $F|_{x=1} = 0$. In Fig. C.1 we see that there are discrete Λ values where $F|_{x=1}$ indeed vanishes. Here of course the precision in which Λ is determined depends on the simulation time for numerically searching for the value when $(F|_{x=1})^2$ is minimal.

From the eigen-state F for a given Λ, the initial particle density $\overline{\rho}_0$ can be inferred by integrating the solution according to Eq. (C.11) (here for the SSEP). By scanning the range of solutions of Λ, f_0 at a given $\Delta\tilde{U}$, one can infer the optimal fluctuation found at $\overline{\rho}_0$. The precision in approaching the exact eigen-values and the desired initial density $\overline{\rho}_0$ is quite satisfying. For the relative deviations in the initial density around 10^{-4} and in Λ being around 10^{-7}, it is typically sufficient to have a run time of one minute.

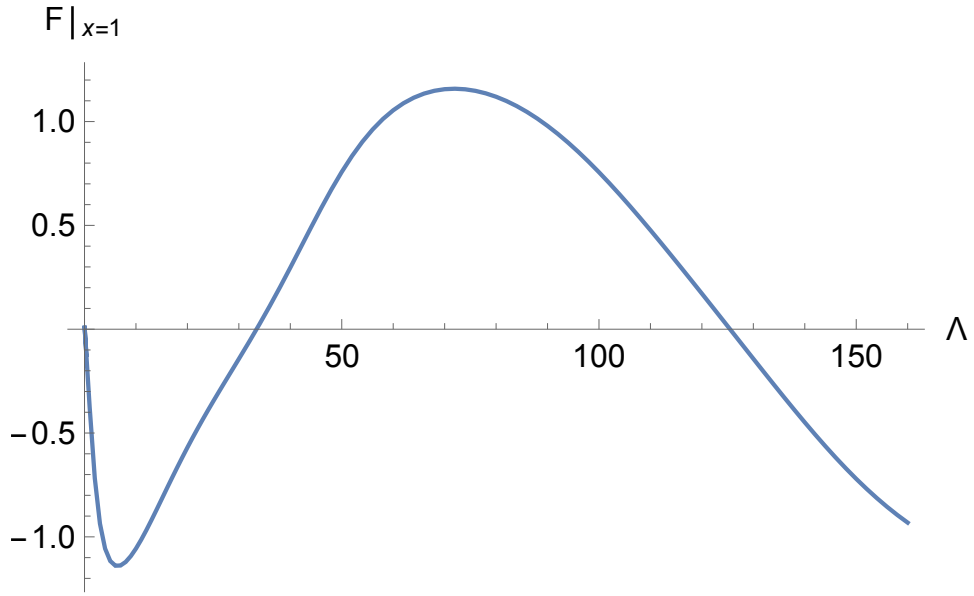

Figure C.1: For the SSEP with the potential $U = \Delta U x^2$, we fix $F_{x=0} = 1.2$ and solve the Euler-Lagrange equation (6) for the alternative boundary conditions for the set of Λ values. The plot shows the value of F at the right boundary. Clearly, there is a discrete set of Λ eigen-values corresponding to an eigen-function F satisfying the real boundary conditions.

At this point, the reader should understand that typically the shooting method gives satisfactory and quick solution to the Euler-Lagrange equation (2.8). Nevertheless, fitting the resulting g factor can be non trivial and result in numerical estimation errors. This is typically not due to the fact that there is a finite precision in determining the mean density $\overline{\rho}_0$ and the eigen-value Λ. Typically, there is no ambiguity around finding the ground state. Indeed, the main problem is two fold. First, $\Phi \asymp \mathrm{e}^{-\Delta \tilde{\mathrm{U}} \mathrm{g}}$ is merely a large $\Delta U g \gg D_0$ approximation. Namely, there are higher order exponential decays. For example, in the SSEP subjected to a linear potential, there is a competition between the two exponentials; $\mathrm{e}^{-\Delta \mathrm{U}(1-\overline{\rho}_0)}$ and $\mathrm{e}^{-\Delta \mathrm{U}}$. For small initial densities, but not vanishingly small, it is hard to differentiate the two comparable contributions, which may skew the fitting. Consider the mean density $\overline{\rho}_0 \sim 0.1$ and $\Delta \tilde{U} \sim 10$. This implies that the pre-exponentials become meaningful and are likely to introduce errors into the determination of g. This scenario is demonstrated in Fig. 2.2 of the main text, as the largest deviation from the analytical projection occurs in this region. It is thus understood that the pre-exponentials are always the

leading source of numerical erroneous estimation of g. This implies that one can always try to push for higher $\Delta\tilde{U}$ values. Realistically, the numerical code has to crunch numbers between $e^{-\Delta\tilde{U}}$ to roughly $e^{\Delta\tilde{U}(1-g)}$. This severely limits the possible range of $\Delta\tilde{U}$ one can hope to deal with numerically. Despite these possible sources for numerical errors, Fig. 2.2 of the main text agrees with the generalized AL remarkably well.

Appendix D

Appendix for Chapter 4

D.1 Survival probability for the piecewise linear potential

In this section, we find the escape rate of SSEP from the piecewise linear potential trap U_{pwl} defined in the main text. Within the MFT, the SSEP is characterized by $D = 1$ and $\chi = \rho(1-\rho)$. The F transformation (2.7) leads to $\rho = \sin^2 F$. Thus one recovers $\omega^2 = \mathrm{e}^{-\beta\Delta\mathrm{U}}\mathrm{A}^2$ (see Chapter 3), where A can be recovered from (see Chapter 3)

$$1 - \overline{\rho}_0 = \int dx \, \frac{1}{1 + A^2 \mathrm{e}^{-\beta \mathrm{U(x)}}}. \tag{D.1}$$

where $\beta = 1/D_0 = 1/k_B T$. For the piecewise linear potential, (D.1) can be solved exactly, leading to

$$\mathrm{e}^{-2\beta\Delta\mathrm{U}\overline{\rho}_0} = \frac{1 + \mathrm{A}^2\mathrm{k}^3}{1 + \mathrm{A}^2} \left(\frac{1 + \mathrm{A}^2\mathrm{k}^2}{1 + \mathrm{A}^2\mathrm{k}} \right)^3. \tag{D.2}$$

In the regime $0 < \overline{\rho}_0 < 1/6$, we expect from the MEC that $A^2 \asymp \mathrm{e}^{2\beta\Delta\mathrm{U}\overline{\rho}_0}$, and so $A^2k^2, A^2k^3 \to 0$ in the large $\beta\Delta U$ limit, where we recall the definition $k = \mathrm{e}^{-\beta\Delta\mathrm{U}/3}$.

Under these approximations, (D.2) can be relaxed into

$$\mathrm{e}^{\beta\Delta\mathrm{U}(2\overline{\rho}_0-1/3)} = \mathrm{b}(1+\mathrm{b})^3, \tag{D.3}$$

where $b = A^2k$. For $\overline{\rho}_0$ at a finite distance away from the critical density $1/6$, b is exponentially small in $\beta\Delta U$. Thus, one can relax $b(1+b)^3 \approx b(1+3b)$, discarding cubic contributions from b. This results in the quadratic b equation, with a single positive root, leading to $\Phi_{\mathrm{MP}} \asymp \mathrm{e}^{-\frac{2}{3}\beta\Delta\mathrm{U}}\mathrm{b}$, where

$$b = \frac{1}{6}\left(-1+\sqrt{1+12\mathrm{e}^{-2\delta\rho\beta\Delta\mathrm{U}}}\right) \tag{D.4}$$

and $\delta\rho = 1/6 - \overline{\rho}_0$. This reproduces Eq. (4.8) of the main text when Eq. (4.6) in the main text is used to determine $\mathcal{F}$.

So far, we have focused on an analytical analysis of the escape rate for the piecewise linear potential. Since we have employed approximation techniques, restricted the analysis to the range $0 < \overline{\rho}_0 < 1/6$, and since it is likely that most potential cannot be analyzed analytically, we turn to present the numerical analysis of the piecewise linear potential. FIG. D.1 presents the response functions corresponding to the piecewise linear potential over the entire range of $\overline{\rho}_0$. The numerical method outlined here is general and not limited to the case of the piecewise linear potential. It has also been utilized to compute the scaling functions for two additional potentials, as described in Appendix D.2. The numerical steps are as follows :

1. Fix $\beta\Delta U$ at some finite value.

2. For this $\beta\Delta U$ value, an array of A is constructed. This is the most technical step of the numerics, as the elements of the array must be carefully selected to cover the entire range of $\overline{\rho}_0$, from 0 to 1. It can be checked, using (D.1), that selecting the elements of the array to range from 0 to $e^{2\beta\Delta U}$ fulfils this requirement.

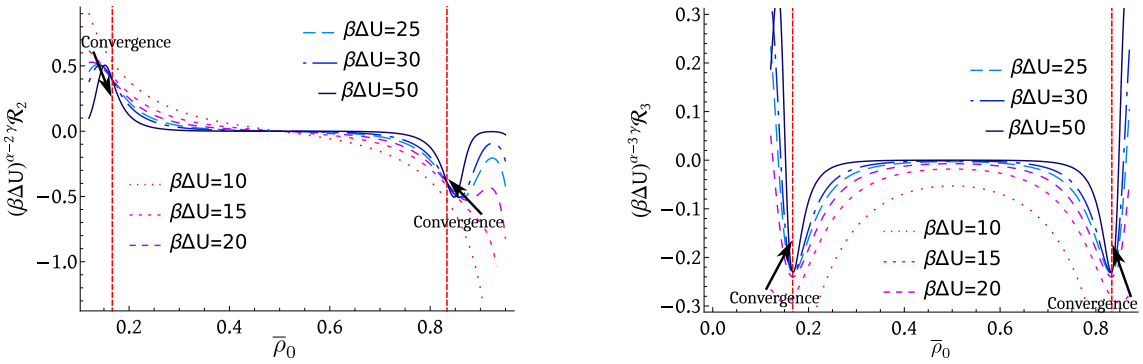

(a) (b)

Figure D.1: The rescaled response functions $\mathcal{R}_n/(\beta\Delta U)^{n\gamma-\alpha}$ for the piecewise linear potential U_{pwl} (see Fig. 4.3 of the main text) are shown for $n = 2$ (panel (a)) and $n = 3$ (panel (b)), and for different $\beta\Delta U = \{10, 15, 20, 25, 30, 50\}$, as indicated by the plot legends. The response functions are obtained by first applying the perturbative approach outlined in Sec. D.1 and in the main text. After computing Φ_{MP}, we use Eq. 4.6 of the main text to determine $\mathcal{R}_n$ for different $\beta\Delta U$. The two vertical dashed red lines highlight the positions of the expected kinks, as determined by the MEC argument. The scaling behavior with $\alpha = \gamma = 1$ predicted from the theoretical analysis is confirmed. One can observe that the scaling convergence is reasonable starting from $\beta\Delta U = 15$, and thus the response functions are able to capture the locations of the kinks at finite $\beta\Delta U$ values. It is noteworthy that such high values of $\beta\Delta U$ are required due to the limitations of the perturbative approach. We expect real data to collapse even for lower $\beta\Delta U$ values.

3. For every element of the array of A, the corresponding $\overline{\rho}_0$ is computed using (D.1) and the corresponding response function is computed using $\mathcal{F} = -\frac{1}{\beta\Delta U}\text{Log}\Big(\text{element of array of } A \times e^{-\beta\Delta U}\Big)$.

4. At the end of step (3), we have $\mathcal{F}$ for different values of $\overline{\rho}_0$ ranging from 0 to 1. The second and the third derivatives of $\mathcal{F}$ are then computed numerically to yield $\mathcal{R}_2$ and $\mathcal{R}_3$ respectively.

5. Steps (1) to (4) are then repeated to find $\mathcal{F}$, $\mathcal{R}_2$ and $\mathcal{R}_3$ for different values of $\beta\Delta U$.

Note that in FIG. D.1, as $\beta\Delta U$ increases, the peaks in $\mathcal{R}_2$ and $\mathcal{R}_3$ progressively shift towards the true position of the kink in the function $g(\overline{\rho}_0)$, as predicted by the MEC argument (also see FIG. 4.3 in the main text). This is quite common in

thermodynamic phase transitions as well.

In Appendix D.2, we demonstrate that inferring the kinks in the function g using response functions is not restricted to the case of piecewise linear potentials. Instead, we show that this approach is applicable to arbitrary potential landscapes. However, before proceeding, it is important to first discuss the experimental applicability of the method.

Experimentally, the escape rate Φ_{MP} of the rightmost particle can be measured for various particle densities $\overline{\rho}_0$. From the obtained values of Φ_{MP}, the function $\mathcal{F}$ can be determined using Eq. 4.6 in the main text. Once $\mathcal{F}$ is known, the response functions $\mathcal{R}_2$ and $\mathcal{R}_3$ can be obtained by evaluating the second and the third order derivative, respectively, of $\mathcal{F}$ with respect to $\overline{\rho}_0$. These response functions will then reveal the kinks in the function g through the peaks observed in the response functions.

D.2 Inferring metastable states in nonlinear potential traps

To demonstrate the predictive power of our theory, and potential pitfalls, we turn to analyze two general trap potentials that cannot be handled analytically. Such potentials appear ubiquitously in various biological settings as mentioned in the main text. In the first case, the potential is given by

$$U_{\mathrm{TE}}/\Delta U = \frac{1}{2}(x + \sin^2(3\pi x/2)), \tag{D.5}$$

which exhibits two kinks in $g(\overline{\rho}_0)$ according to the MEC. In the second case, we take the following form of the potential

$$U_{XS}/\Delta U = \frac{1}{8}(6x + 2\sin^2(5\pi x/2)), \tag{D.6}$$

which features 4 kinks in $g(\overline{\rho}_0)$ according to the MEC. We demonstrate that the response functions $\mathcal{R}_2$ and $\mathcal{R}_3$ successfully capture these kinks in both cases.

D.2.1 Inferring kinks in $g(\overline{\rho}_0)$ for $\mathbf{U_{TE}/\Delta U = \frac{1}{2}(x + \sin^2(3\pi x/2))}$

Let us first consider the trap potential U_{TE}. All the results in this section are obtained numerically. According to the MEC, g exhibits two kinks. See FIG. D.2(a). Yet, the emergence of the kinks cannot be identified directly, even for relatively high values of $\beta\Delta U$. The response functions $\mathcal{R}_2$ and $\mathcal{R}_3$ capture the emerging kinks in g at finite $\beta\Delta U$. Here we have numerically computed the response functions using the algorithm of Appendix D.1. The resulting function $\mathcal{F}$ and the response functions $\mathcal{R}_2$ and $\mathcal{R}_3$ are plotted in FIG. D.2 for several values of $\beta\Delta U$. As $\beta\Delta U$ is increased, the peaks in the response function shift progressively closer towards the expected position of the kinks, predicted by the MEC argument.

D.2.2 Inferring kinks in $g(\overline{\rho}_0)$ for $\mathbf{U_{XS}/\Delta U = \frac{1}{8}(6x + 2\sin^2(5\pi x/2)}$

In the present case, the function g, determined using the MEC argument, features four kinks, as shown in FIG. D.3. Following a similar approach as outlined in D.2.1, the functions $\mathcal{F}$ and the response functions $\mathcal{R}_2$ and $\mathcal{R}_3$ are computed, which is shown in FIG. D.3. It is evident from the figure that, at finite values of $\beta\Delta U$, the response function $\mathcal{R}_3$ successfully identifies the emergence of the four kinks, as well as their positions. However, $\mathcal{R}_2$ fails to detect the first kink, although it is still able to identify the emergence of the other three kinks. The reason for this failure stems from the perturbative approach employed in Chapter 3, which forms the basis for the current analysis, assumes the limit $\beta\Delta U\overline{\rho}_0 \gg 1$. In the case of the first kink, for

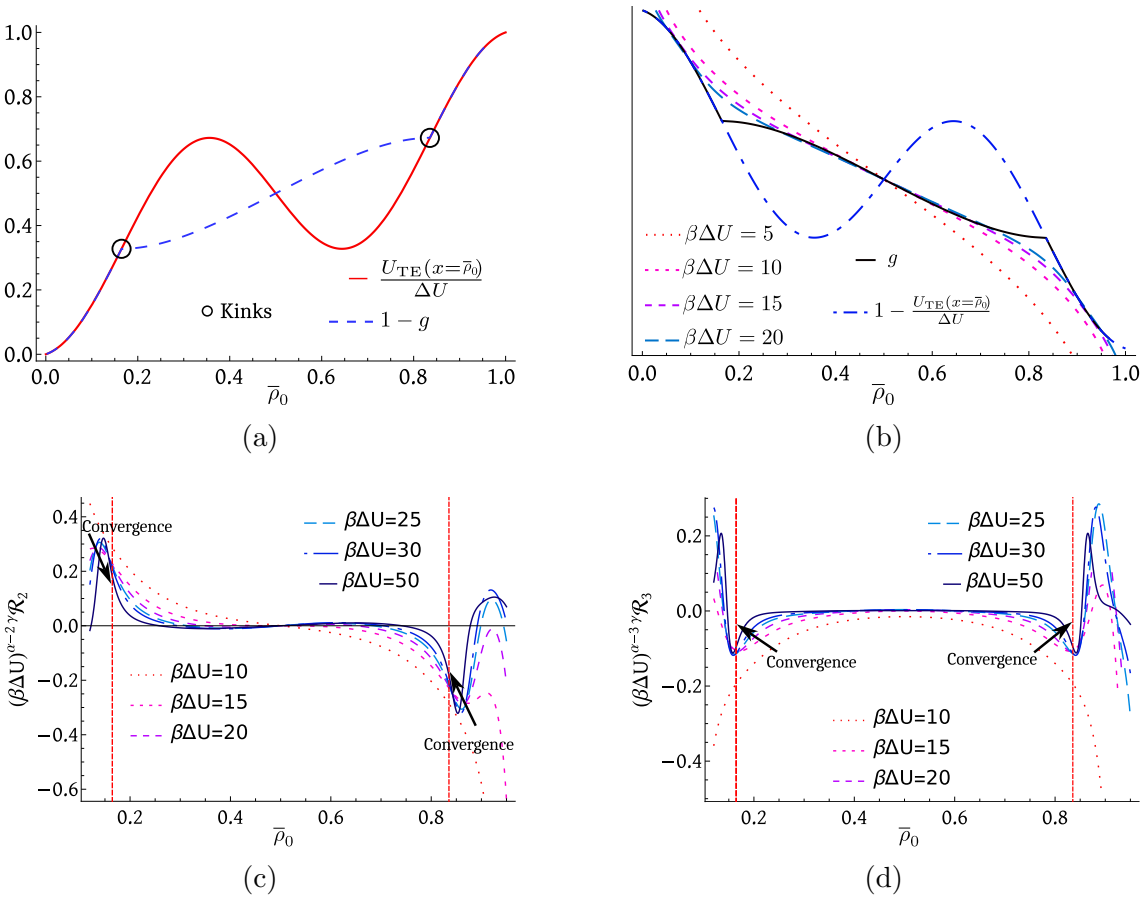

Figure D.2: Exploring metastabilities in a generic nonlinear potential landscape $U_{TE}/\Delta U = \frac{1}{2}\left(x + \sin^2(3\pi x/2)\right)$, which exhibits two local extrema. Panel (a): The potential $U_{\rm TE}/\Delta U$ and the corresponding $1 - g(\overline{\rho}_0)$ are shown as solid and dashed curves, respectively. The function g is determined using the MEC argument, as described in the main text. Panel (b): The function $1 - U_{\rm TE}/\Delta U$ (dashed blue) and $g(\overline{\rho}_0)$ (solid) are plotted, along with the effective free-energy curves $\mathcal{F}$ for $\beta\Delta U = \{5, 10, 15, 20\}$. As $\beta\Delta U$ increases, $\mathcal{F}$ converges to $g(\overline{\rho}_0)$, consistent with the limit $\beta\Delta U \to \infty$. The kinks in $g(\overline{\rho}_0)$ are not visible in $\mathcal{F}$ for finite $\beta\Delta U$, but emerge in the asymptotic limit where $\mathcal{F} \to g(\overline{\rho}_0)$. Panels (c) and (d): The rescaled response functions $\mathcal{R}_n/(\beta\Delta U)^{n\gamma-\alpha}$ are shown for $n = 2, 3$ and $\beta\Delta U = \{10, 15, 20, 25, 30, 50\}$. The peaks accurately identify the kink locations (vertical dashed red lines), demonstrating that the kinks can be detected even at finite $\beta\Delta U$. The scaling exponents are $\alpha = 1$ and $\gamma = 1.15$. While the precise values of α and γ are not essential for locating the kinks, the perturbative approach requires relatively large $\beta\Delta U$ (typically $\gtrsim 15$) to clearly resolve the divergences. In contrast, experimental data is not expected to suffer from this limitation. Away from the kinks, a faster convergence is observed, as expected.

which $\overline{\rho}_0$ is quite small, this approximation breaks down. Nevertheless, by increasing the value of $\beta\Delta U$ such that $\beta\Delta U\overline{\rho}_0 \gg 1$, the emergence of the first kink would also be identifiable in $\mathcal{R}_2$. It is important to note here that this is a limitation imposed by the perturbation theory. We do not expect such limitations if the escape rate data were obtained experimentally or through the direct simulation of the SSEP.

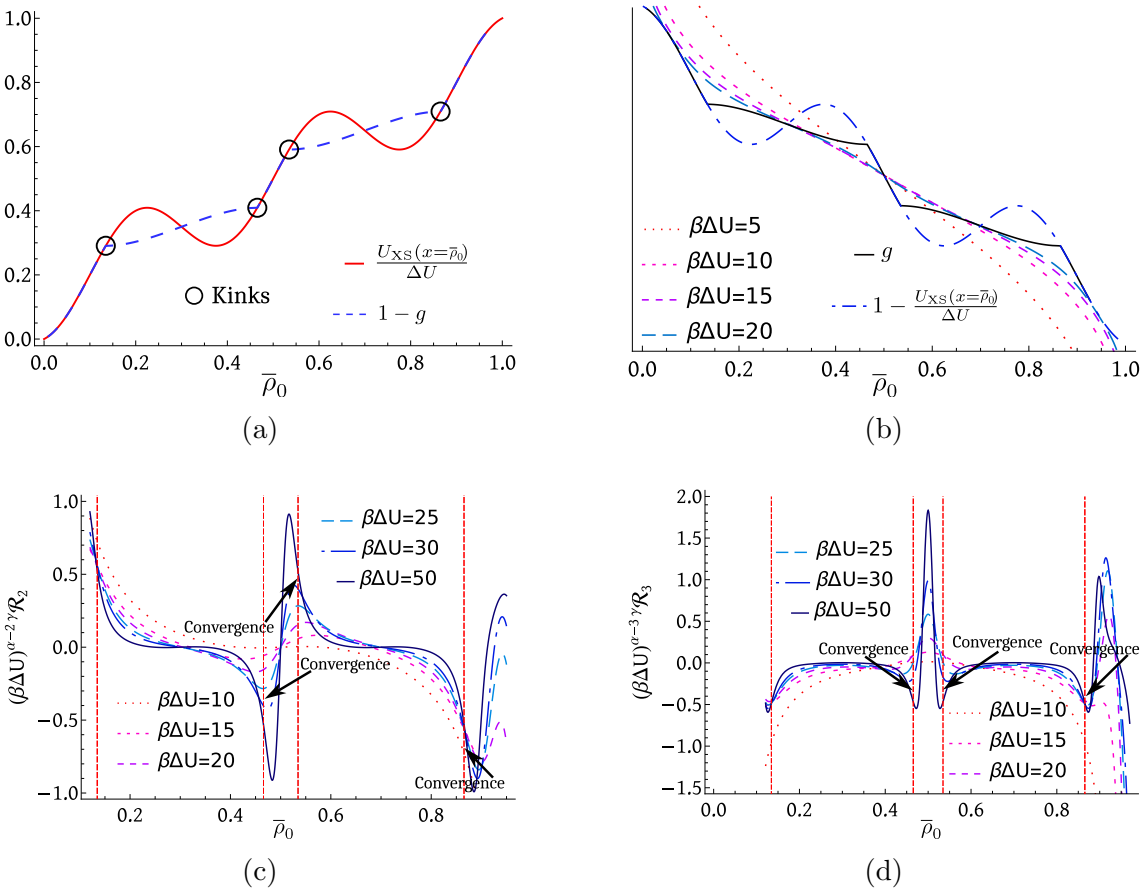

Figure D.3: Exploring metastabilities in a potential landscape $U_{XS}/\Delta U = \frac{1}{8}(6x + 2\sin^2(5\pi x/2))$, with four local extrema. Panel (a): The potential $U_{\rm XS}/\Delta U$ and $1-g$ are plotted as solid and dashed lines, with the actual positions of the kinks indicated. The locations of these kinks in g are determined using the MEC argument, which predicts four kinks, each corresponding to a local extremum of the potential. Panel (b): The functions $1 - U_{\rm XS}/\Delta U$ and g are plotted as dashed blue curve and a solid line, respectively, as indicated in the legend. The other legend labels represent the "free energies" curve for $\mathcal{F}$ for various values of $\beta\Delta U = \{5, 10, 15, 20\}$. The kinks become apparent only in the experimentally unfeasible limit $\beta\Delta U \to \infty$, in which case $\mathcal{F} \to g$. Panels (c) and (d): The rescaled response functions $\mathcal{R}_n/(\beta\Delta U)^{n\gamma-\alpha}$ are plotted to infer the locations of the kinks at finite $\beta\Delta U$ values. These response functions are shown for $n = 2, 3$ and for different values of $\beta\Delta U = \{10, 15, 20, 25, 30, 50\}$, as indicated in the legends. The scaling exponents are $\gamma = 1$, $\alpha = 1$. While the diverging peaks of the response functions accurately identify the kink positions (denoted by vertical dashed red lines), the scaling collapse is less pronounced. Nevertheless, extracting the scaling exponents is not essential for locating the kinks.

Appendix E

Appendix for Chapter 5

E.1 Discussions on connecting conditions and MFPT computation in the presence of intermediate barriers in linear and harmonic potentials

The aim of this appendix is to derive the matching conditions, for the case when a potential has a single and multiple kinks in it. Although such conditions are natural and can generically be found in textbooks such as [20], we provide this discussion for completeness. Consider a generic potential $U(x_0)$ which has a kink at $x_0 = a$. Therefore, $U'(x_0)$ is finitely discontinuous and $U''(x_0)$ is infinitely discontinuities at $x_0 = a$. For such potentials, these discontinuities appear in the left hand side (LHS) of the differential equation, Eq. (5.5). However, the right hand side (RHS) of Eq. (5.5) is identically equal to -1 and, hence, remains continuous, regardless of the form of the potential $U(x_0)$ on the LHS. It follows that the discontinuities on the LHS must cancel in such a way that the LHS becomes continuous, consistent with the continuity of the RHS.

There are two potential scenarios for the cancellation of this discontinuity

1. $\mathcal{T}'(x_0)$ is finitely discontinuous at $x_0 = a$ resulting in $\mathcal{T}''(x_0)$ being infinitely discontinuous there.

2. $\mathcal{T}'(x_0)$ is continuous at $x_0 = a$, while $\mathcal{T}''(x_0)$ is finitely discontinuous at that point.

The first possibility is rejected as an infinite discontinuity cannot cancel out a finite discontinuity. Therefore, we are left only with the second option. This implies that $\mathcal{T}''(x_0)$ must be finitely discontinuous at $x_0 = a$, which can get canceled by the finite discontinuity of $U'(x_0)$ at $x_0 = a$. It, therefore, follows that $\mathcal{T}'(x_0)$ must remain continuous at $x_0 = a$. This automatically implies that $\mathcal{T}(x_0)$ must also be continuous at this point. Thus, we have found the two connecting conditions : $\mathcal{T}(x_0)$ and $\mathcal{T}'(x_0)$ must be continuous at $x_0 = a$.

Note that the two connecting conditions can also be derived as follows. First, we recast Eq. (5.5) into the following form

$$k_B T \frac{d}{dx_0}\left[e^{-U(x_0)/k_B T}\frac{d}{dx_0}\mathcal{T}(x_0)\right] = -e^{-U(x_0)/k_B T}. \tag{E.1}$$

Since a is the position of the kink, we integrate Eq. (E.1) from $a-\epsilon$ to $a+\epsilon$, where ϵ is a small positive number. The right-hand side becomes zero because $e^{-U(x_0)/k_B T}$ is a continuous function, as $U(x_0)$ is continuous. Therefore, we obtain:

$$e^{-U(x_0)/k_B T}\frac{d}{dx_0}\mathcal{T}(x_0)\Big|_{x_0=a-\epsilon}^{x_0=a+\epsilon} = 0. \tag{E.2}$$

Since $e^{-U(x_0)/k_B T}$ is continuous at $x_0 = a$, the above equation implies that

$$\frac{d}{dx_0}\mathcal{T}(x_0 = a-\epsilon) = \frac{d}{dx_0}\mathcal{T}(x_0 = a+\epsilon). \tag{E.3}$$

Writing it in terms of the notations $\mathcal{T}^{\mathrm{L}}_{1,I}$ and $\mathcal{T}^{\mathrm{L}}_{1,II}$ used in Section 5.2.1, implies Eq. (5.12). Since the derivative of the function MFPT is continuous, it follows that the MFPT itself must also be continuous at $x_0 = a$. This yields Eqs. (5.12) and (5.13) of the main text.

The derivations of the connecting conditions, given in Eqs. (5.12) and (5.13), do not rely on any specific functional form of the potential $U(x_0)$. The only requirement for the validity of these conditions is that the potential $U(x_0)$ is continuous at $x_0 = a$, the position of the kink. Consequently, the same connecting conditions apply to the MFPT corresponding to the piecewise-harmonic potential defined in Eq. (5.17).

To compute the MFPT for the case of multiple intermediate barriers in a linear or harmonic potential, it is important to note that there are two connecting conditions at the position of each kink. In addition to these, we already have two boundary conditions: a reflecting boundary at $x_0 = 0$ and an absorbing boundary at $x_0 = 1$. Thus, for N kinks, we have a total of $2N + 2$ conditions that the MFPT function $\mathcal{T}(x_0)$ must satisfy. Furthermore, the presence of N kinks implies that the domain is divided into $N + 1$ segments or regions. The solution of the differential equation (Eq. (5.5)) within each region contains two undetermined integration constants. Therefore, across all $N + 1$ regions, there are $2(N + 1)$ integration constants in total. Since the number of independent conditions matches the number of unknown constants, all integration constants are uniquely determined. Consequently, the corresponding MFPT is fully specified.

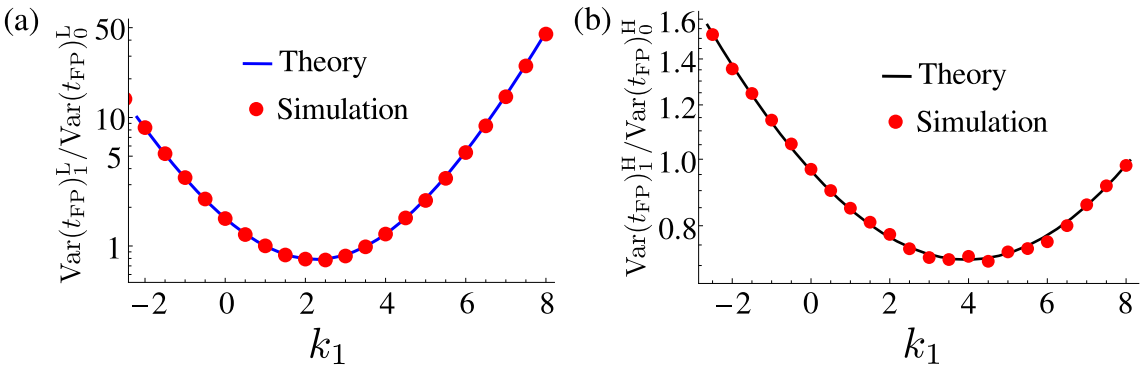

Figure E.1: Semi-logarithmic plots of the scaled variance of the FPT for $k_BT = 1$, $\Delta U = 3$ and $a = 0.3$, shown for (a) the piecewise linear potential (Eq. (5.10)) and (b) the piecewise harmonic potential (Eq. (5.17)). Solid lines represent the analytical solution of corresponding differential equations and the red dots correspond to the microscopic simulation of Eq. (5.1). The curves falling below unity reflect a reduction in the FPT variance.

E.2 Computation of variance in first-passage time for the linear and harmonic potentials with single intermediate barrier

In this section, we analyze the variance of the first-passage time (FPT) for a Brownian particle in the said potential configurations. We first consider the case of a linear potential, Eq. (5.8), and compare it to a modified linear potential that includes a single intermediate barrier, Eq. (5.10), while keeping the overall barrier height ΔU identical in both cases. Remarkably, we find that analogous to the behavior observed for the MFPT, the variance of the FPT in the modifed linear potential can be reduced relative to that in the purely linear potential (see Fig. E.1(a)). Then, we extend this analysis to the harmonic potential (Eq. (5.15)) and a modified harmonic potential with one intermediate barrier, Eq. (5.17). A similar trend is observed in this case as well, as illustrated in Fig. E.1(b).

To delve deeper, we start by denoting the second moment of the FPT by $\langle t_{\mathrm{FP}}^2 \rangle$.

Accordingly, its variance is expressed by

$$\mathrm{Var}(t_{\mathrm{FP}}) = \langle t_{\mathrm{FP}}^2 \rangle - \mathcal{T}^2. \tag{E.4}$$

The second moment satisfies the following differential equation obtained via the backward Fokker-Planck formalism [20],

$$2\mathcal{T}(x_0) = U'(x_0)\partial_{x_0}[\langle t_{\mathrm{FP}}^2 \rangle(x_0)] - k_B T \partial_{x_0}^2[\langle t_{\mathrm{FP}}^2 \rangle(x_0)], \tag{E.5}$$

where, $\langle t_{\mathrm{FP}}^2 \rangle(x_0)$ denotes the second moment of the FPT for the particle starting its motion at x_0.

For the linear and harmonic potentials, Eq. (E.5) can be solved directly for $\langle t_{\mathrm{FP}}^2 \rangle(x_0)$, subject to appropriate boundary conditions (specified below). However, for the piecewise-linear and piecewise-harmonic potentials defined in Eqs. (5.10) and (5.17), respectively, the derivatives $U'(x_0)$ are discontinuous at the kink position $x_0 = a$. Consequently, Eq. (E.5) must be solved separately in two regions: region I, $x_0 \in [0, a]$, and region II, $x_0 \in [a, 1]$. The complete solution thus requires two connecting conditions at $x_0 = a$, in addition to the boundary conditions. The procedure outlined in Appendix E.1 implies that the second moment $\langle t_{\mathrm{FP}}^2 \rangle(x_0)$ and its first derivative is continuous at $x_0 = a$, despite a finite discontinuity in $U'(x_0)$ at $x_0 = a$. (This conclusion requires the continuity of $\mathcal{T}(x_0)$, which has been explicitly established in Appendix E.1.) This provides the necessary connecting conditions for determining the solutions.

E.2.1 Reduction of the FPT variance in linear potential

Here, we first determine the variance of the FPT corresponding to the linear potential in Eq. (5.8). For this potential Eq. (E.5) takes the form

$$2\mathcal{T}_0^{\mathrm{L}}(x_0) = \Delta U \partial_{x_0}[\langle t_{\mathrm{FP}}^2\rangle_0^{\mathrm{L}}(x_0)] - k_B T \partial_{x_0}^2[\langle t_{\mathrm{FP}}^2\rangle_0^{\mathrm{L}}(x_0)] \tag{E.6}$$

where $\langle t_{\mathrm{FP}}^2\rangle_0^{\mathrm{L}}(x_0)$ denotes the second moment of the FPT for a particle starting at position x_0 and moving under the linear potential (no intermediate barrier) defined in Eq. (5.8). Eq. (E.6) is solved subject to the reflecting and absorbing boundary conditions:

$$\partial_{x_0}\langle t_{\mathrm{FP}}^2\rangle_0^{\mathrm{L}}(x_0 = 0) = 0, \qquad \langle t_{\mathrm{FP}}^2\rangle_0^{\mathrm{L}}(x_0 = 1) = 0. \tag{E.7}$$

Once $\langle t_{\mathrm{FP}}^2\rangle_0^{\mathrm{L}}(x_0)$ is obtained, the variance of the FPT follows from the relation

$$\mathrm{Var}(t_{\mathrm{FP}})_0^{\mathrm{L}}(x_0) = \langle t_{\mathrm{FP}}^2\rangle_0^{\mathrm{L}}(x_0) - (\mathcal{T}_0^{\mathrm{L}})^2(x_0), \tag{E.8}$$

which, upon evaluation at $x_0 = 0$, yields the following expression for the variance of the FPT for a particle starting at $x_0 = 0$:

$$\begin{aligned}\mathrm{Var}(t_{\mathrm{FP}})_0^{\mathrm{L}}(x_0 = 0) &\equiv \mathrm{Var}(t_{\mathrm{FP}})_0^{\mathrm{L}} \\ &= \left[\frac{4(k_BT)^2}{\Delta U^4} - \frac{4k_BT}{\Delta U^3}\right] e^{\Delta U/k_BT} \\ &+ \frac{(k_BT)^2}{\Delta U^4} e^{2\Delta U/k_BT} - \frac{5(k_BT)^2}{\Delta U^4} - \frac{2k_BT}{\Delta U^3}\end{aligned} \tag{E.9}$$

Next consider the piecewise linear potential U_1^{L} in Eq. (5.10) (one intermediate barrier). The corresponding quantities in this case are denoted by $\mathrm{Var}(t_{\mathrm{FP}})_1^{\mathrm{L}}(x_0)$ for the variance of the first-passage time and by $\langle t_{\mathrm{FP}}^2\rangle_1^{\mathrm{L}}(x_0)$ for its second moment.

These quantities are related through

$$\mathrm{Var}(t_{\mathrm{FP}})_1^{\mathrm{L}}(x_0) = \langle t_{\mathrm{FP}}^2\rangle_1^{\mathrm{L}}(x_0) - (\mathcal{T}_1^{\mathrm{L}})^2(x_0). \tag{E.10}$$

For this potential in Eq. (5.10), Eq. (E.5) must be expressed separately in the two regions of the domain. The resulting equations take the form

$$2\mathcal{T}_{1,I}^{\mathrm{L}}(x_0) = \Delta U k_1 \partial_{x_0}[\langle t_{\mathrm{FP}}^2\rangle_{1,I}^{\mathrm{L}}(x_0)] - k_B T \partial_{x_0}^2[\langle t_{\mathrm{FP}}^2\rangle_{1,I}^{\mathrm{L}}(x_0)], \tag{E.11}$$

for $x_0 \in [0, a]$ and,

$$2\mathcal{T}_{1,II}^{\mathrm{L}}(x_0) = \Delta U k_2 \partial_{x_0}[\langle t_{\mathrm{FP}}^2\rangle_{1,II}^{\mathrm{L}}(x_0)] - k_B T \partial_{x_0}^2[\langle t_{\mathrm{FP}}^2\rangle_{1,II}^{\mathrm{L}}(x_0)], \tag{E.12}$$

for $x_0 \in [a, 1]$. Here, subscript I (respectively II) denotes the quantities in region I (respectively II).

Since the second moment and its first derivative is continuous at $x_0 = a$, we have the following connecting conditions:

$$\langle t_{\mathrm{FP}}^2\rangle_{1,I}^{\mathrm{L}}(x_0 = a) = \langle t_{\mathrm{FP}}^2\rangle_{1,II}^{\mathrm{L}}(x_0 = a) \tag{E.13}$$

and

$$\partial_{x_0}\langle t_{\mathrm{FP}}^2\rangle_{1,I}^{\mathrm{L}}(x_0 = a) = \partial_{x_0}\langle t_{\mathrm{FP}}^2\rangle_{1,II}^{\mathrm{L}}(x_0 = a). \tag{E.14}$$

The reflecting boundary at $x_0 = 0$ implies that

$$\partial_{x_0}\langle t_{\mathrm{FP}}^2\rangle_{1,I}^{\mathrm{L}}(x_0 = 0) = 0 \tag{E.15}$$

and the absorbing boundary leads to

$$\langle t_{\mathrm{FP}}^2\rangle_{1,II}^{\mathrm{L}}(x_0 = 1) = 0. \tag{E.16}$$

We obtained analytical expressions for $\langle t_{\rm FP}^2\rangle_{1,I}^{\rm L}(x_0)$ and $\langle t_{\rm FP}^2\rangle_{1,II}^{\rm L}(x_0)$ (not shown here) by solving Eqs. (E.11) and (E.12), subject to the connecting and the boundary conditions specified in Eqs. (E.13), (E.14), (E.15), and (E.16). The second moment of the first-passage time for a particle starting at $x_0 = 0$ is then given by $\langle t_{\rm FP}^2\rangle_{1,I}^{\rm L}(x_0 = 0)$. This quantity determines the corresponding variance of the first-passage time through Eq. (E.10), evaluated at $x_0 = 0$, which we denote as $\mathrm{Var}(t_{\rm FP})_1^{\rm L}$ for brevity. The variance $\mathrm{Var}(t_{\rm FP})_1^{\rm L}$ depends on the system parameters k_1, k_2, ΔU, and a. However, according to the fixed barrier height condition given in Eq. (5.11), k_2 can be expressed as function of k_1 and a. Hence $\mathrm{Var}(t_{\rm FP})_1^{\rm L}$ is now a function of k_1, ΔU and a, which turns out to be

$$\begin{aligned}
\mathrm{Var}(t_{\rm FP})_1^{\rm L} = {} & \frac{(k_BT)^2 e^{\frac{2\Delta U}{k_BT}}}{k_1^2k_2^2\Delta U^4} + \frac{4k_BT(k_BT-\Delta U\theta)}{k_1^2k_2^2\Delta U^4}e^{\frac{\Delta U}{k_BT}} \\
& + \frac{2(k_BT)^2\alpha}{k_1^2k_2^3\Delta U^4}e^{\frac{(2-ak_1)\Delta U}{k_BT}} - \frac{2(k_BT)^2\alpha}{k_1^3k_2^2\Delta U^4}e^{\frac{(1+ak_1)\Delta U}{k_BT}} \\
& + \frac{(k_BT)^2\alpha^2}{k_1^2k_2^4\Delta U^4}e^{\frac{2(1-ak_1)\Delta U}{k_BT}} + \frac{(k_BT)^2\alpha^2}{k_1^4k_2^2\Delta U^4}e^{\frac{2ak_1\Delta U}{k_BT}} \\
& + \left(\frac{4ak_BT\alpha}{k_1^3k_2\Delta U^3} - \frac{2(k_BT)^2\beta}{k_1^4k_2^3\Delta U^4}\right)e^{\frac{ak_1\Delta U}{k_BT}} \\
& + \left(\frac{4ak_BT\alpha}{k_1k_2^3\Delta U^3} - \frac{4k_BT\alpha}{k_1k_2^3\Delta U^3} - \frac{2(k_BT)^2\gamma}{k_1^3k_2^4\Delta U^4}\right) \\
& \times e^{\frac{(1-ak_1)\Delta U}{k_BT}} + \frac{(k_BT)^2\delta}{k_1^4k_2^4\Delta U^4} + \frac{2k_BT\phi}{k_1^3k_2^3\Delta U^3}
\end{aligned} \tag{E.17}$$

where, $k_2 = (1-k_1a)/(1-a)$, $\alpha = (k_1-k_2)$, $\beta = (k_1^3+k_1^2k_2-2k_2^3)$, $\gamma = (k_2^3-2k_1^3+k_1k_2^2)$, $\delta = (-5k_1^4+2k_1^3k_2+k_1^2k_2^2+2k_1k_2^3-5k_2^4)$, $\theta = (k_1-ak_1+ak_2)$ and $\phi = [(-1+a)k_1^3-ak_2^3]$.

For the purpose of analysis, we fix $k_BT = 1$, $\Delta U = 3$ and $a = 0.3$. This implies that $\mathrm{Var}(t_{\rm FP})_0^{\rm L}$ is fully determined from Eq. (E.9). However, variance $\mathrm{Var}(t_{\rm FP})_1^{\rm L}$ remains a function of k_1. For the sake of comparison, we plot the variation of the ratio $\mathrm{Var}(t_{\rm FP})_1^{\rm L}/\mathrm{Var}(t_{\rm FP})_0^{\rm L}$, which we call scaled variance, with k_1 in FIG. E.1(a). The plot shows that for a range of k_1 values, the scaled variance is less than unity,

indicating that the introduction of an intermediate barrier within the original linear potential results in a reduction of the variance compared to that of the original process.

E.2.2 Reduction of the FPT variance in harmonic potential

Like the case of linear and modified linear potential with one intermediate barrier, we now analyze the variance of the harmonic, (Eq.(5.15)), and modified harmonic potential with one intermediate barrier in Eq. (5.17). Following the similar procedure as in the precious subsection, we determine the scaled variance, $\mathrm{Var}(t_{\mathrm{FP}})_1^{\mathrm{H}}/\mathrm{Var}(t_{\mathrm{FP}})_0^{\mathrm{H}}$, by numerically solving the corresponding differential equations. Fixing the parameters at same values as in the case of linear and piecewise-linear potential, we plot the scaled variance as a function of k_1 in FIG. E.1(b). Like the previous case, the curve shows that for a range of k_1 values, scaled variance $\mathrm{Var}(t_{\mathrm{FP}})_1^{\mathrm{H}}/\mathrm{Var}(t_{\mathrm{FP}})_0^{\mathrm{H}}$ is less than unity. This indicates that introducing an intermediate barrier into a harmonic potential is indeed useful in reducing the FPT variance.

E.3 Simulation specification

To generate the numerical data presented in Fig. 5.2 , we simulated 10^5 independent trajectories of a Brownian particle. Each trajectory was initialized at $x = 0$ and evolved until the particle was absorbed at the boundary $x = 1$. The time evolution of the particle in each microscopic time scale dt can be written in terms of a discretized form of Langevin equation in (5.1) using Euler–Maruyama approximation such as

$$x(t + \Delta t) = x(t) - U'(x(t))\,\Delta t + \sqrt{2D\Delta t}\,\mathcal{N}(0, 1), \tag{E.18}$$

where $\mathcal{N}(0,1)$ denotes a Gaussian random variable with zero mean and unit variance. For the data corresponding to Fig. 5.2(b), $dt = 10^{-5}$ was used, while for Fig. 5.2(d), $dt = 10^{-7}$ was employed to ensure numerical accuracy. In both cases, the barrier height was fixed at $\Delta U = 3$, and the position of the kink was set to $a = 0.3$.

Appendix F

Diffusivity and mobility for different models

In this section we present the derivation of diffusivity and mobility for the SSEP, the SIP, the ZRP and the strong particles model. The derivations for the SSEP, SIP and ZRP closely follow the work of Derrida et al. [153] while the derivation for the strong particles model is done by closely following the work of Gabrielli and Krapivsky [83].

F.1 The symmetric simple exclusion process (SSEP)

The one dimensional symmetric simple exclusion process is defined on a lattice of L sites, where each site $i = 1, \ldots, L$ can be occupied by at most one particle, with occupation variable $\eta_i \in \{0, 1\}$. In the bulk, particles perform symmetric nearest neighbour hopping, attempting to jump from site i to $i \pm 1$ with rate 1, and the attempt is successful only if the target site is empty, enforcing the exclusion constraint (see Fig. 2.1(a)). The system is coupled to reservoirs at the left and right boundaries with densities ρ_l^{SSEP} and ρ_r^{SSEP} respectively. At site $i = 1$, particles are injected with rate α when the site is empty and removed with rate γ when it is

occupied, while at the site $i = L$, particles are injected with rate δ and removed with rate β under the same conditions.

The boundary rates determine the densities of the reservoirs [153, 156]. To see this, consider an auxiliary single site coupled only to the left reservoir, with particle injection rate α when the site is empty and removal rate γ when it is occupied. If p denotes the stationary occupation probability of this site, then stationarity gives $\alpha(1-p) = \gamma p$ so that $p = \alpha/(\alpha+\gamma)$. This stationary occupation probability defines the density of the left reservoir

$$\rho_l^{\mathrm{SSEP}} = \frac{\alpha}{\alpha+\gamma}. \tag{F.1}$$

Similarly, for the right reservoir one obtains

$$\rho_r^{\mathrm{SSEP}} = \frac{\delta}{\beta+\delta}. \tag{F.2}$$

F.1.1 Computation of diffusivity $D(\rho)$ for SSEP

We now proceed to derive the expression for the diffusivity $D(\rho)$ for the symmetric simple exclusion process. To this end, following Ref. [153], we introduce the integrated current $Y_i(t)$, defined as the net number of particles that have jumped from site i to site $i+1$ up to time t. At the boundaries, we define $Y_0(t)$ as the integrated current from the left reservoir to site 1, and $Y_L(t)$ as the integrated current from site L to the right reservoir. This leads to

$$Y_0(t+dt) = \begin{cases} Y_0(t)+1; & \text{prob. } \alpha(1-\eta_1)dt \\ Y_0(t)-1; & \text{prob. } \gamma\,\eta_1 dt \\ Y_0(t) & \text{otherwise.} \end{cases} \tag{F.3}$$

This implies that the conditional average is given by

$$\begin{aligned}\langle Y_0(t+dt)|Y_0(t),\eta_1(t)\rangle =&\alpha(1-\eta_1)[Y_0(t)+1]dt+\gamma\,\eta_1[Y_0(t)-1]dt\\&+[1-\alpha(1-\eta_1)dt-\gamma\,\eta_1 dt]Y_0(t)\end{aligned} \tag{F.4}$$

The unconditional average is given by

$$\langle Y_0(t+dt)\rangle = [\alpha(1-\langle\eta_1\rangle)-\gamma\,\langle\eta_1\rangle]dt+\langle Y_0(t)\rangle \tag{F.5}$$

In the limit of $dt\to 0$, the above equation leads to the following evolution equation for $\langle Y_0(t)\rangle$,

$$\frac{d}{dt}\langle Y_0(t)\rangle = \alpha(1-\langle\eta_1\rangle)-\gamma\langle\eta_1\rangle. \tag{F.6}$$

Similarly, for the right boundary, we have the following relation,

$$Y_L(t+dt)=\begin{cases}Y_L(t)+1; & \text{prob. } \beta\,\eta_L dt\\ Y_L(t)-1; & \text{prob. } \delta(1-\eta_L)dt\\ Y_L(t) & \text{otherwise.}\end{cases} \tag{F.7}$$

This gives the following evolution equation for unconditional average $\langle Y_L(t)\rangle$:

$$\frac{d}{dt}\langle Y_L(t)\rangle = \beta\langle\eta_L\rangle-\delta(1-\langle\eta_L\rangle). \tag{F.8}$$

Similarly, in the bulk, one gets the following evolution equation for the unconditional average $\langle Y_i(t)\rangle$:

$$\frac{d}{dt}\langle Y_i(t)\rangle = \langle\eta_i\rangle-\langle\eta_{i+1}\rangle \tag{F.9}$$

For future purposes, it is important to note that in steady state $\frac{d\langle Y_i\rangle}{dt}$ doesn't depend on the the index i. This can be understood by observing the following relation

between integrated currents and occupation variables:

$$Y_i(t) - Y_{i-1}(t) = \eta_i(0) - \eta_i(t) \tag{F.10}$$

Taking the average and then the time derivative results in the following relation:

$$\frac{d}{dt}\langle Y_i(t) - Y_{i-1}(t)\rangle = -\frac{d}{dt}\langle \eta_i(t)\rangle. \tag{F.11}$$

In the steady state, the right hand side of the above equation is zero. It then follows that that in the steady state, $\frac{d\langle Y_i(t)\rangle}{dt}$ is independent of i, for all $i \in \{0, 1, ..., L\}$.

Now, defining $a_1 = 1/(\alpha + \gamma)$, $b_1 = 1/(\beta + \delta)$ and using the relations F.1, F.2, F.6, F.8 and F.9, we obtain the following relation

$$a_1\frac{d}{dt}\langle Y_0(t)\rangle + b_1\frac{d}{dt}\langle Y_L(t)\rangle + \sum_{i=1}^{L-1}\frac{d}{dt}\langle Y_i(t)\rangle = \rho_l^{\text{SSEP}} - \rho_r^{\text{SSEP}}. \tag{F.12}$$

Using the steady state independence of $\frac{d\langle Y_i(t)\rangle}{dt}$ on i, we get

$$\frac{d}{dt}\langle Y_0(t)\rangle = \frac{\rho_l^{\text{SSEP}} - \rho_r^{\text{SSEP}}}{a_1 + b_1 + L - 1}, \tag{F.13}$$

which at large L limit leads to

$$\frac{d}{dt}\langle Y_0(t)\rangle = \frac{\rho_l^{\text{SSEP}} - \rho_r^{\text{SSEP}}}{L}. \tag{F.14}$$

From the above equation, it is clear that for SSEP, the diffusivity $D = 1$.

F.1.2 Computation of mobility $\chi(\rho)$ for SSEP

To compute the mobility, we use the Einstein's relation between diffusivity $D(\rho)$ and mobility $\chi(\rho)$ [8], which is as follows:

$$\chi(\rho) = \frac{D(\rho)}{f''(\rho)}, \tag{F.15}$$

where $f(\rho)$ is the equilibrium free energy density of the system per unit length, and k_BT is assumed to be unity. $\rho = N/L$ is the average density of the system, where N is the number of particles and L is the length of the system. Since we know $D(\rho) = 1$ from the last section, we need to determine $f(\rho)$ to determine the mobility $\chi(\rho)$ from Eq. (F.15). This is what we do below.

For the SSEP with a fixed number N of particles on L sites, all configurations with N particles are equally likely in equilibrium [140, 156, 157]. Since the total number of such configurations is $\frac{L!}{N!(L-N)!}$, the canonical partition function is

$$Z_{N,L} = \frac{L!}{N!(L-N)!} e^{-E_0}. \tag{F.16}$$

where all configurations with N particles are equally probable and have same energy E_0. Here again it is assumed that $k_BT = 1$. Using the Stirling's approximation $\ln K! \approx K \ln K - K$ one gets the following expression for the free energy density

$$f(\rho) = -\frac{1}{L} \ln(Z_{N,L}) \approx [\rho \ln \rho + (1-\rho) \ln(1-\rho)] + \frac{E_0}{L}, \tag{F.17}$$

where, $\rho = N/L$. This implies that the second derivatiove of the free energy density is given by

$$f''(\rho) = \frac{1}{\rho(1-\rho)} \tag{F.18}$$

Using Eqs. F.18 and F.15 and $D = 1$ for SSEP, we find that $\chi(\rho) = \rho(1-\rho)$.

F.2 The simple inclusion process (SIP)

In SIP, a particle at site i jumps to site $i+1$ with rate $\eta_i(1+\eta_{i+1})$ and to site $i-1$ with rate $\eta_i(1+\eta_{i-1})$ (see Fig 2.1(b)). We couple the system to reservoirs at the left and right boundaries with densities ρ_l^{SIP} and ρ_r^{SIP} respectively. The coupling with the reservoir is as follows. A particle from left reservoir can come to the site 1 with rate $\alpha(1+\eta_1)$ and the rate of hopping from the site 1 to the left reservoir is $\gamma\eta_1$. Similarly, A particle from right reservoir can come to the site L with rate $\delta(1+\eta_L)$ and the rate of hopping from the site L to the right reservoir is $\beta\eta_L$.

The boundary rates determine the densities of the reservoirs [156]. To see this, consider an auxiliary single site coupled only to the left reservoir, with particle injection rate $\alpha(1+\eta)$ and removal rate $\gamma\eta$. The stationary distribution of this process satisfies detailed balance $\alpha(1+n)\,p_n = \gamma(n+1)\,p_{n+1}$ (p_n denotes the stationary probability of finding n particles on this site) which yields

$$p_n = \left(\frac{\alpha}{\gamma}\right)^n p_0. \tag{F.19}$$

This gives the following value of mean for $\alpha < \gamma$

$$\langle\eta\rangle = \frac{\alpha}{\gamma-\alpha}. \tag{F.20}$$

This mean occupation is identified with the density of the left reservoir, yielding

$$\rho_l^{\text{SIP}} = \frac{\alpha}{\gamma-\alpha}. \tag{F.21}$$

Similarly, for the right reservoir one obtains (for $\delta < \beta$)

$$\rho_r^{\text{SIP}} = \frac{\delta}{\beta-\delta}. \tag{F.22}$$

F.2.1 Computation of diffusivity $D(\rho)$ for SIP

We now derive the diffusivity $D(\rho)$ for the symmetric inclusion process (SIP), following the same strategy as in Ref. [153]. We again introduce the integrated current $Y_i(t)$ as the net number of particles that have jumped from site i to site $i+1$ up to time t. At the boundaries, $Y_0(t)$ denotes the integrated current from the left reservoir to site 1, and $Y_L(t)$ denotes the integrated current from site L to the right reservoir.

At the left boundary, the dynamics is given by

$$Y_0(t+dt) = \begin{cases} Y_0(t)+1; & \text{prob. } \alpha(1+\eta_1)dt \\ Y_0(t)-1; & \text{prob. } \gamma\,\eta_1 dt \\ Y_0(t) & \text{otherwise.} \end{cases} \tag{F.23}$$

This leads to the following evolution equation for the unconditional average $\langle Y_0(t)\rangle$

$$\frac{d}{dt}\langle Y_0(t)\rangle = \alpha(1+\langle\eta_1\rangle) - \gamma\langle\eta_1\rangle. \tag{F.24}$$

Similarly, at the right boundary,

$$Y_L(t+dt) = \begin{cases} Y_L(t)+1; & \text{prob. } \beta\,\eta_L dt \\ Y_L(t)-1; & \text{prob. } \delta(1+\eta_L)dt \\ Y_L(t) & \text{otherwise,} \end{cases} \tag{F.25}$$

which gives

$$\frac{d}{dt}\langle Y_L(t)\rangle = \beta\langle\eta_L\rangle - \delta(1+\langle\eta_L\rangle). \tag{F.26}$$

Similarly, in the bulk one obtains

$$\frac{d}{dt}\langle Y_i(t)\rangle = \langle \eta_i\rangle - \langle \eta_{i+1}\rangle. \tag{F.27}$$

As in the SSEP case, $\frac{d}{dt}\langle Y_i(t)\rangle$ is independent of i. See Eqs. (F.10) and Eqs. (F.11), which remain valid for the SIP as well.

Now, we define $a_2 = 1/(\gamma - \alpha)$ and $b_2 = 1/(\beta - \delta)$, and using the relations between boundary rates and reservoir densities [Eqs. (F.21), (F.22)], together with Eqs. (F.24), (F.26), and (F.27), we obtain

$$a_2\frac{d}{dt}\langle Y_0(t)\rangle + b_2\frac{d}{dt}\langle Y_L(t)\rangle + \sum_{i=1}^{L-1}\frac{d}{dt}\langle Y_i(t)\rangle = \rho_l^{\text{SIP}} - \rho_r^{\text{SIP}}. \tag{F.28}$$

Using the steady state independence of $\frac{d}{dt}\langle Y_i(t)\rangle$ on i, this gives

$$\frac{d}{dt}\langle Y_0(t)\rangle = \frac{\rho_l^{\text{SIP}} - \rho_r^{\text{SIP}}}{a_2 + b_2 + L - 1}. \tag{F.29}$$

In the large L limit, this reduces to

$$\frac{d}{dt}\langle Y_0(t)\rangle = \frac{\rho_l^{\text{SIP}} - \rho_r^{\text{SIP}}}{L}. \tag{F.30}$$

Thus, we conclude that for SIP also, the diffusivity is $D(\rho) = 1$.

F.2.2 Computation of mobility $\chi(\rho)$ for SIP

For the SIP, the equilibrium canonical partition function (k_BT assumed to be 1) is

$$Z_{N,L} = \frac{(N + L - 1)!}{N!(L-1)!}e^{-E_0}, \tag{F.31}$$

where all configurations with N particles are equally probable [156] and have the same energy E_0. Using Stirling's approximation for large L and N, we obtain the following expression for the equilibrium free energy density:

$$f(\rho) = -\frac{1}{L}\ln Z_{N,L} \approx \rho\ln\rho - (1+\rho)\ln(1+\rho) + \frac{E_0}{L}, \tag{F.32}$$

where $\rho = N/L$. Using the Einstein relation, Eq. (F.15), together with the diffusivity $D(\rho) = 1$ for SIP, we obtain the mobility

$$\chi(\rho) = \rho(1+\rho). \tag{F.33}$$

F.3 The zero range process (ZRP)

The one dimensional zero range process is defined on a lattice of L sites, where each site $i = 1, \ldots, L$ can host an arbitrary number of particles, with occupation variable η_i. In the bulk, particles perform symmetric nearest neighbour hopping: a particle at site i jumps to site $i \pm 1$ with rate $r(\eta_i)$, with $r(0) = 0$ (see Fig. 2.1(d)). The system is coupled to reservoirs at the left and right boundaries with densities ρ_l^{ZRP} and ρ_r^{ZRP} respectively. At site $i = 1$, particles are injected from the left reservoir with rate α and removed to the reservoir with rate $\gamma\, r(\eta_1)$, while at site $i = L$, particles are injected with rate δ and removed with rate $\beta\, r(\eta_L)$.

F.3.1 Relation between diffusivity and mobility in ZRP

Occupancy probability for the ZRP exhibits a product measure [48]. To see that, consider the detailed balance condition for a particle jumping between two neigh-

boring sites i and j with occupancies η_i and η_j respectively:

$$r(\eta_i)\, P_i(\eta_i) P_j(\eta_j) = r(\eta_j + 1)\, P_i(\eta_i - 1) P_j(\eta_j + 1). \tag{F.34}$$

This relation can be rewritten as

$$r(\eta_i) \frac{P_i(\eta_i)}{P_i(\eta_i - 1)} = r(\eta_j + 1) \frac{P_j(\eta_j + 1)}{P_j(\eta_j)}\,. \tag{F.35}$$

Since the left-hand side depends only on η_i and the right-hand side only on η_j, both sides must be equal to a constant, which we denote by λ. This constant is the fugacity and parametrizes the stationary state. We therefore obtain the following recursion relation at equilibrium for any site i

$$\frac{P_i(\eta_i)}{P_i(\eta_i - 1)} = \frac{\lambda}{r(\eta_i)}, \tag{F.36}$$

Iterating this relation yields the following relation for every site i

$$P_i(\eta_i) = P_i(0)\, \frac{\lambda^{\eta_i}}{r(\eta_i)!}, \tag{F.37}$$

where $r(\eta_i)! \equiv r(\eta_i) r(\eta_i - 1) \cdots r(1)$ with $r(0)! = 1$. Normalization fixes $P(0) = 1/Z_\lambda$, where

$$(Z_\lambda)_i = \sum_{\eta_i \geq 0} \frac{\lambda^{\eta_i}}{r(\eta_i)!}. \tag{F.38}$$

For the zero range process, the stationary state is thus a product measure with single site occupation distribution $P_i(\eta_i) = \frac{1}{(Z_\lambda)_i} \frac{\lambda^\eta}{r(\eta_i)!}$. The density is related to the fugacity by

$$\rho_i = \langle \eta_i \rangle = \lambda \partial_\lambda \log(Z_\lambda)_i. \tag{F.39}$$

A key identity is that the average hopping rate (at any site i) at equilibrium equals

the fugacity,

$$\langle r(\eta_i)\rangle = \lambda. \tag{F.40}$$

Eq. (F.40) suggest that at equilibrium, average hopping rate is same for every site i, and is equal to the equilibrium fugacity λ.

In what follows, we will calculate the non-equilibrium steady state current J, identify the reservoirs' mean density and infer from Fick's law $J = -D(\rho)\partial_x\rho$ at the macroscopic limit. Then, χ accounts for the current variance at equilibrium. We will follow a similar approach to [153] in order to infer D, χ functions of the ZRP.

To do that, consider $Y_i(t)$ the integrated current between site i and $i+1$. At the long time limit, $J = \frac{d}{dt}\langle Y_i\rangle = \frac{1}{L+1}\sum_{i=0}^{L}\langle Y_i\rangle$. Namely, we assume there is no condensation of particles at any given site. Using the ZRP dynamics, we find the following relation in the bulk:

$$Y_i(t+dt) = \begin{cases} Y_i(t), & \text{probability } 1 - r(\eta_i)\,dt - r(\eta_{i+1})\,dt, \\ Y_i(t)+1, & \text{probability } r(\eta_i)\,dt, \\ Y_i(t)-1, & \text{probability } r(\eta_{i+1})\,dt, \end{cases} \tag{F.41}$$

which leads to the following equation for the evolution of the unconditional average $\langle Y_i(t)\rangle$,

$$\frac{d}{dt}\langle Y_i(t)\rangle = \langle r(\eta_i)\rangle - \langle r(\eta_{i+1})\rangle = \lambda_i - \lambda_{i+1}. \tag{F.42}$$

The identification $\langle r(\eta_i)\rangle = \lambda_i$ follows from the structure of the stationary state. In zero-range process, the non-equilibrium steady state retains a factorized (product) form, but is characterized by a site-dependent fugacity profile λ_i. The single-site distribution at site i is given by $P_i(\eta_i) \propto \lambda_i^{\eta_i}/r(\eta_i)!$, which directly implies $\langle r(\eta_i)\rangle = \lambda_i$. Consequently, the local current is expressed as the difference of neighboring fugacities, as shown in Eq. (F.42) [158].

At the left boundary, we have the following relation :

$$Y_0(t+dt) = \begin{cases} Y_0(t), & \text{probability } 1-\alpha dt - \gamma\, r(\eta_1)dt \\ Y_0(t)+1, & \text{probability } \alpha\, dt \\ Y_0(t)-1, & \text{probability } \gamma\, r(\eta_1)dt, \end{cases} \tag{F.43}$$

which leads to the following evolution equation,

$$\frac{d}{dt}\langle Y_0(t)\rangle = \alpha - \gamma\,\langle r(\eta_1)\rangle = \alpha - \gamma\,\lambda_1. \tag{F.44}$$

At the the right reservoir, one obtains:

$$Y_L(t+dt) = \begin{cases} Y_L(t), & \text{probability } 1-\delta dt - \beta\, r(\eta_L)dt \\ Y_L(t)+1, & \text{probability } \beta\, r(\eta_L)\, dt \\ Y_L(t)-1, & \text{probability } \delta\, dt, \end{cases} \tag{F.45}$$

which leads to

$$\frac{d}{dt}\langle Y_L\rangle = \beta\,\langle r(\eta_L)\rangle - \delta = \beta\lambda_L - \delta \tag{F.46}$$

In the long time limit,

$$\begin{aligned} J &= \frac{d}{dt}\langle Y_0\rangle = \frac{d}{dt}\langle Y_1\rangle = \cdots = \frac{d}{dt}\langle Y_{L-1}\rangle = \frac{d}{dt}\langle Y_L\rangle \\ &= \alpha - \gamma\lambda_1 = \lambda_1 - \lambda_2 = \cdots = \lambda_{L-1} - \lambda_L = \beta\lambda_L - \delta \end{aligned} \tag{F.47}$$

The above equation after some algebra leads to the following expression of steady-state current J:

$$J = \frac{\frac{\alpha}{\gamma} - \frac{\delta}{\beta}}{L - 1 + \frac{1}{\beta} + \frac{1}{\gamma}}. \tag{F.48}$$

We note that an isolated site 1 must be in equilibrium with reservoir, implying $J = \alpha - \gamma\lambda_1 = 0$. This implies that the fugacity of the reservoir is $\lambda_{_l} = \alpha/\gamma$.

Similarly, the fugacity of the right reservoir is $\lambda_r = \delta/\beta$. Hence, Eq. (F.48) becomes

$$J = \frac{\lambda_l - \lambda_r}{L - 1 + \frac{1}{\beta} + \frac{1}{\gamma}}. \tag{F.49}$$

We note that in the large L limit the above relation becomes

$$J = -\frac{\Delta\lambda}{L} = -\partial_x \lambda = -D(\rho)\partial_x \rho \tag{F.50}$$

where $\Delta\lambda \equiv \lambda_r - \lambda_l$. This implies that

$$D(\rho) = \frac{d}{d\rho}\lambda. \tag{F.51}$$

To compute the mobility $\chi(\rho)$, we need to consider the system in equilibrium where the fugacities of the reservoirs are equal, viz. $\lambda_l = \lambda_r = \lambda_i = \lambda$.

The equilibrium condition also implies that

$$\frac{d}{dt}\langle Y \rangle = 0 \tag{F.52}$$

where, we have removed the site index from Y as the above relation is true for integrated current across every bond. This implies that at every site, $\Delta\langle Y\rangle \equiv \langle Y(t+dt)\rangle - \langle Y(t)\rangle = 0$. Also from Eq. (F.41) one easily obtains that $\langle(\Delta Y_i)^2\rangle = 2\lambda dt$. Therefore, the cumulant $\Delta\langle Y_i^2\rangle_c = 2\lambda dt$. This implies that in the limit $dt \to 0$

$$\frac{d}{dt}\langle Y_i^2\rangle_c = 2\lambda \tag{F.53}$$

The Einstein's relation implies that the mobility is defined by $2\chi/L = \frac{d}{dt}\langle Y_i^2\rangle_c/L$. This implies that

$$\chi = \lambda \tag{F.54}$$

Hence, we have from Eq. (F.51)

$$D(\rho) = \frac{d}{d\rho}\chi(\rho). \tag{F.55}$$

F.4 The strong particles model

In this section, we reproduce the derivation of diffusivity $D(\rho)$ and the mobility $\chi(\rho)$ for the strong particles model, closely following the steps of Ref. [83] including the notation adopted therein. The detailed dynamics of the model has been introduced in Chapter 2. Briefly, the model incorporates an exclusion constraint similar to that of the SSEP, in the sense that each site can be occupied by at most one particle. However, in contrast to the SSEP, every attempted move is always successful. More precisely, consider a particle at site i attempting to hop to site $i+1$. If the target site is empty, the particle simply moves to site $i+1$. If, however, site $i+1$ is already occupied, the particle at site i moves to site $i+1$ while simultaneously pushing the particle at site $i+1$ to site $i+2$. This pushing mechanism propagates recursively; if site $i+2$ is also occupied, the particle at $i+2$ is pushed to $i+3$, and so on, until the first vacant site is reached.

Consequently, the dynamics can be viewed as the collective motion of a block of particles (see Fig. 2.1(c)). Let $r(k)$ denote the rate at which a block of k particles is displaced by one lattice site, either to the right or to the left. Furthermore, following Ref. [83], we define d_i^+ as the number of consecutive occupied sites starting from site i and extending to the right until the first empty site is encountered. Similarly, d_i^- denotes the number of consecutive occupied sites starting from site i and extending to the left, up to the first vacant site. If the i-th site is vacant, $d_i^+ = 0 = d_i^-$

We now define the instantaneous current across the bond $(i, i+1)$ for a given configuration η, denoted by $j_\eta(i, i+1)$. The dynamics of the strong particles model

implies that this current can be expressed as

$$\begin{aligned} j_\eta(i,i+1) &= [\text{rate of flow from } i \to i+1] - [\text{rate of flow from } i+1 \to i] \\ &= \sum_{k=1}^{d_i^-} r(d_{i+1}^+ + k) - \sum_{k=1}^{d_{i+1}^+} r(d_i^- + k) \\ &= R(d_i^-) - R(d_{i+1}^+) \end{aligned} \tag{F.56}$$

where,

$$R(n) = \sum_{k=1}^{n} r(k). \tag{F.57}$$

We now prove below that in any block of particles denoted by C, the sum of currents across the relevant bonds for the block C is zero. To see this we consider a configuration η where a block of particles extends from site i to $i+m$. The relevant currents for this block of particles are $j_\eta(i-1,i)$, $j_\eta(i,i+1)\cdots$, $j_\eta(i+m,i+m+1)$. From Eq. (F.56), the sum of these bond currents are

$$\begin{aligned} \text{Sum of relevant bond currents in } C =& [R(d_{i-1}^-) + R(d_i^-) + \cdots + R(d_{i+m}^-)] \\ & - [R(d_i^+) + R(d_{i+1}^+) + \cdots + R(d_{i+m+1}^+)] \end{aligned} \tag{F.58}$$

We note that the two sums on the right-hand side of Eq. (F.58) contain the same terms in reverse order. Indeed, for a block extending from i to $i+m$, we have $d_{i-1}^- = 0 = d_{i+m+1}^+$, $d_i^- = 1 = d_{i+m}^+$, $d_{i+1}^- = 2 = d_{i+m-1}^+$, and so on, up to $d_{i+m}^- = m+1 = d_i^+$. Therefore, the two sums are identical, and the right-hand side vanishes identically, i.e.,

$$\text{Sum of relevant bond currents in any } C = 0. \tag{F.59}$$

Since Eq. (F.59) holds for any block of particles, the instantaneous current field has zero circulation within a block. As a consequence, the current can be represented in the following form

$$j_\eta(i,i+1) = h_\eta(i) - h_\eta(i+1), \tag{F.60}$$

where the function h is such that $h_\eta(i) = 0$ whenever the i-th site is vacant.

The next step is to find the form of the function $h_\eta(i)$ for occupied site i. To do that we first rearrange Eq. (F.60) to get $h_\eta(k+1) = h_\eta(k) - j_\eta(k, k+1)$. We next note that the index of the first vacant site to the left of the i-th site is given by $i - d_i^-$, which implies that

$$h_\eta(i - d_i^-) = 0 \tag{F.61}$$

Now, note that from the leftmost relevant bond $(i - d_i^-, i - d_i^- + 1)$, we get the following relation using Eqs. (F.60) and (F.61)

$$h_\eta(i - d_i^- + 1) = -j_\eta(i - d_i^-, i - d_i^- + 1) \tag{F.62}$$

Similarly, using Eqs. (F.60), (F.61) and (F.62), we get

$$h_\eta(i - d_i^- + 2) = -j_\eta(i - d_i^-, i - d_i^- + 1) - j_\eta(i - d_i^- + 1, i - d_i^- + 2) \tag{F.63}$$

Iteratively carrying out the above procedures , we get

$$h_\eta(i) = -\sum_{k=0}^{d_i^- - 1} j_\eta(i - d_i^- + k, i - d_i^- + k + 1) \tag{F.64}$$

To make the above relation simpler we define $p \equiv d_i^- - k$, which reduces the above equation into the following simpler form:

$$h_\eta(i) = -\sum_{p=1}^{d_i^-} j_\eta(i - p, i - p + 1). \tag{F.65}$$

Using Eq. (F.56) into Eq. (F.65), we get for occupied site i

$$\begin{aligned} h_\eta(i) &= -\sum_{p=1}^{d_i^-} R(d_{i-p}^-) + \sum_{p=1}^{d_i^-} R(d_{i-p+1}^+) \\ &= -\sum_{p=1}^{d_i^-} R(d_i^- - p) + \sum_{p=1}^{d_i^-} R(d_i^+ + p - 1) \\ &= -\sum_{k=0}^{d_i^- - 1} R(k) + \sum_{k=d_i^+}^{d_i^+ + d_i^- - 1} R(k) \\ &= -H(d_i^-) + H(d_i^+ + d_i^-) - H(d_i^+) \end{aligned} \tag{F.66}$$

where, the function H is such that

$$H(n) = \sum_{k=1}^{n-1} R(k) \quad \text{for } n \geq 2; \quad H(0) = 0 = H(1) \tag{F.67}$$

F.4.1 Computation of diffusivity $D(\rho)$ for strong particles

We now derive the expression of diffusivity $D(\rho)$ for strong particles model. Following Ref. [83], we view the one-dimensional lattice with periodic boundary conditions as embedded into the continuous circle $[0, 1]$, by associating the point $i/L \in [0, 1]$. Thus, the discrete lattice is represented as a set of evenly spaced points on the circle. Let W be a smooth periodic function on this circle.

We clearly have the following relation for the test function W:

$$\begin{aligned}\sum_i j_\eta(i,i+1)W_i &= \sum_i [h_\eta(i) - h_\eta(i+1)]W(i/L) \\ &= \sum_i h_\eta(i)W(i/L) - \sum_i h_\eta(i+1)W(i/L) \\ &= \sum_i h_\eta(i)W(i/L) - \sum_k h_\eta(k)W((k-1)/L) \\ &= \sum_i h_\eta(i)[W(i/L) - W((i-1)/L)] \\ &\approx \sum_i h_\eta(i)\frac{1}{L}\partial_x W(x)\Big|_{x=i/L}\end{aligned} \tag{F.68}$$

where the last line in the above equation follows on Taylor's expansion and assuming large L.

The strong particles model admits the Bernoulli grand-canonical product measure ν_ρ at density ρ, given by [83]

$$\nu_\rho(\eta) = \prod_i \rho^{\eta_i}(1-\rho)^{1-\eta_i}, \tag{F.69}$$

under which the occupation variables $\{\eta_i\}$ are independent and satisfy $\langle \eta_i \rangle_{\nu_\rho} = \rho$ for all sites i. Under the assumption of local equilibrium, the microscopic quantity $h_\eta(i)$ can be replaced by its average with respect to the local Bernoulli measure $\nu_{\rho(x)}$. Denoting this average by

$$G(\rho) \equiv \langle h_\eta(i) \rangle_{\nu_\rho}, \tag{F.70}$$

the discrete sum

$$\frac{1}{L}\sum_i h_\eta(i)\,\partial_x W(x)\Big|_{x=i/L} \tag{F.71}$$

can then be viewed as a Riemann sum, and in the limit $L \to \infty$ it converges to

$$\int_0^1 G(\rho(x))\,\partial_x W(x)\,dx. \tag{F.72}$$

Integrating by parts and using periodicity, we get

$$\int_0^1 G(\rho(x))\,\partial_x W(x)\,dx = -\int_0^1 [\partial_x G(\rho(x))] W(x)\,dx = -\int_0^1 [\partial_\rho G(\rho)]\,\partial_x \rho(x)\,W(x)\,dx. \tag{F.73}$$

Since the above identity holds for arbitrary test functions $W(x)$, we identify the macroscopic current as

$$J(x) = -[\partial_\rho G(\rho)]\,\partial_x \rho(x). \tag{F.74}$$

Comparing this with Fick's law,

$$J(x) = -D(\rho)\partial_x \rho(x), \tag{F.75}$$

we obtain

$$D(\rho) = \frac{d}{d\rho} G(\rho). \tag{F.76}$$

In what follows, we derive the expression of $G(\rho)$. $D(\rho)$ can then be obtained using Eq. (F.76).

Using Eqs. (F.70) and (F.66) and realising the fact that for a given density ρ the translational invariance of the probability measure ν_ρ implies that $\langle h_\eta(i)\rangle_{\nu_\rho} = \langle h_\eta(0)\rangle_{\nu_\rho}$, we have the following expression for $G(\rho)$

$$G(\rho) = \langle H(d_0^- + d_0^+)\rangle_{\nu_\rho} - \langle H(d_0^-)\rangle_{\nu_\rho} - \langle H(d_0^+)\rangle_{\nu_\rho} \tag{F.77}$$

Let us now compute the term $\langle H(d_0^+)\rangle_{\nu_\rho}$.

$$\begin{aligned}\langle H(d_0^+)\rangle_{\nu_\rho} &= \sum_{k=2}^{\infty} H(k) P_{\nu_\rho}(d_0^+ = k) = \sum_{k=2}^{\infty} H(k)\rho^k(1-\rho) \\ &= (1-\rho)\sum_{k=2}^{\infty}\left[\sum_{n=1}^{k-1} R(n)\right]\rho^k \\ &= (1-\rho)\sum_{n=1}^{\infty} R(n)\left[\sum_{k=n+1}^{\infty}\rho^k\right] \\ &= \sum_{n=1}^{\infty} R(n)\rho^{n+1}.\end{aligned} \tag{F.78}$$

Similarly,

$$\langle H(d_0^-)\rangle_{\nu_\rho} = \langle H(d_0^+)\rangle_{\nu_\rho}, \tag{F.79}$$

and

$$\langle H(d_0^- + d_0^+)\rangle_{\nu_\rho} = (1-\rho)\sum_{n=1}^{\infty} n\rho^n R(n) + \rho\sum_{n=1}^{\infty}\rho^n R(n). \tag{F.80}$$

Combining Eqs. (F.78), (F.79) and (F.80), $G(\rho)$ is obtained from Eq. (F.77) as

$$G(\rho) = (1-\rho)\sum_{n=1}^{\infty} n\rho^n R(n) - \rho\sum_{n=1}^{\infty}\rho^n R(n) \tag{F.81}$$

A convenient way to proceed from the above expression is to introduce the generating function

$$S(\rho) = \sum_{n=1}^{\infty}\rho^n r(n). \tag{F.82}$$

Using the relation $R(n) = \sum_{k=1}^{n} r(k)$, we first rewrite

$$\sum_{n=1}^{\infty}\rho^n R(n) = \sum_{n=1}^{\infty}\rho^n\sum_{k=1}^{n} r(k) = \sum_{k=1}^{\infty} r(k)\sum_{n=k}^{\infty}\rho^n = \frac{1}{1-\rho}\sum_{k=1}^{\infty}\rho^k r(k) = \frac{S(\rho)}{1-\rho}. \tag{F.83}$$

Differentiating this relation with respect to ρ, we obtain

$$\sum_{n=1}^{\infty} n\rho^{n-1} R(n) = \frac{d}{d\rho}\left(\frac{S(\rho)}{1-\rho}\right), \tag{F.84}$$

and hence

$$\sum_{n=1}^{\infty} n\rho^n R(n) = \rho \frac{d}{d\rho}\left(\frac{S(\rho)}{1-\rho}\right). \tag{F.85}$$

Substituting these results into the expression for $G(\rho)$ in Eq. (F.81), one finds that

$$G(\rho) = \rho \frac{dS}{d\rho}. \tag{F.86}$$

Therefore, using $D(\rho) = \frac{dG}{d\rho}$, the diffusivity is given by

$$D(\rho) = \frac{d}{d\rho}\left[\rho \frac{dS}{d\rho}\right] = \sum_{n=1}^{\infty} n^2 \rho^{n-1} r(n), \tag{F.87}$$

which is precisely the expression obtained in Ref. [83].

F.4.2 Computation of mobility $\chi(\rho)$ for strong particles

In this section, we use Einstein's relation in Eq. (F.15) and expression of diffusivity in Eq. (F.87) to get the expression for $\chi(\rho)$.

Using the equilibrium product measure [Eq. (F.69)], all configurations with density $\rho = N/L$ have equal weight, and the total number of such configurations is $\frac{L!}{L!(L-N)!}$ which is same as SSEP(See Sec. F.1.2). Hence, the derivative of equilibrium free energy is given by Eq. (F.18) and therefore from Eq. (F.15)

$$\chi = \rho(1-\rho)D(\rho), \tag{F.88}$$

where $D(\rho)$ is given by Eq. (F.87).